MONASH UNIVERSITY
THESIS ACCEPTED IN SATISFACTION OF THE
REQUIREMENTS FOR THE DEGREE OF
DOCTOR OF PHILOSOPHY
ON.................. 28 July 2004.................

....[redacted]......................

Sec. Research Graduate School Committee

Supervisor's signature:	[redacted]	Date: 9 Dec 2003
(please print name)	Anthony W.C. Kun	

Errata

p 7 point 1: "${}^{(4)}\Gamma^{\mu}{}_{\nu\gamma}$" for "${}^{(3)}\Gamma^{\mu}{}_{\nu\gamma}$"

p 7 point 2: "$\perp_{ij}$" for "$\perp_{\mu\nu}$", "D_i" for "D_α"

p 7 eqn (1.4): " $D_i W^j{}_k = \partial_i W^j{}_k - {}^{(3)}\Gamma^m_{ik} W^j{}_m + {}^{(3)}\Gamma^j_{im} W^m{}_k$ " for " $D_\alpha W^\mu{}_\nu = \partial_\alpha W^\mu{}_\nu - {}^{(3)}\Gamma^\tau_{\alpha\nu} W^\mu{}_\tau + {}^{(3)}\Gamma^\mu_{\alpha\tau} W^\tau{}_\nu$ "

p 16 para 2: "[Misner et.al., 1973]" for "[Bernstein, 1993]"

p 18 equ (2.29): "$tr(K)$" for "K"

p 23 para 3, sentence 3: "have shown certain promise, in terms of stability, but work in this area is ongoing and the full advantages are yet to be understood completely" for "have not shown themselves to have significant numerical stability advantages over the standard equations."

p 30 para 2, sentence 2: "For our analysis we consider the case where the charge and current densities arise from a system of point particles and the fields" for "The evolution of these fields in a vacuum"

p 50 eqn (3.82): "$tr(K)$" for "K"

p 56 eqn (3.100): Add ")" to end of equation

p 58 para 2 (definition of $g_{\mu\nu}$): "β_1" for "β^1"; "β_2" for "β^2"; "β_3" for "β^3"

p 64 para 1, last sentence: "and not necessarily interested in chasing" for "not necessarily chasing"

p 65, para 1, last sentence: remove "and for this reason is not often used for 3-D, large-scale simulations in general relativity"

p 68, para 2, first sentence: "shift" for "lapse"

p 70, eqn (5.7): " $\frac{1}{nx}\sqrt{\Sigma_{i=0}^{i=nx}(W_i)^2}$" for " $\sqrt{\Sigma_{i=0}^{i=nx}(W_i)^2}$"

p 81 para 1, second sentence: "than" for "then"

p 86 para 1, first sentence: "gauge condition" for "constraint equation"

p 96 para 2 first sentence: "The line-element that describes a static black hole may be given by" for "Historically, the first line-element to describe a black hole is given in"

p 98, para 1 last sentence: "isometry surface" for "event horizon"

p 99, para 4, first sentence: "non-Dirichlet" for "free evolution"

p 116 figure 6.8, both plots: "t" for "eta"

p 120 para 1: replace sentence 2 with "Although harmonic slicing is singularity avoiding, the inner point of the grid ($\eta = 0$) comes arbitrarily close to the singularity ($r = 0$), making this slicing poor choice for numerical simulations, unless adaptive mesh refinement techniques are employed."

Addendum

p 7, add at the end of point 2: "This particular definition of stability is appropriate in this work as we are not concerned with spacetimes where the solution itself behaves exponentially. Furthermore, as we are interested in long-term evolutions, having exponentially growing errors would render a simulation of little use, even if the solution is 'stable' in the rigorous mathematical sense."

p 8, para 1, comment: The 3+1 formalism was originally published (using a restrictive gauge) by Choquet-Bruhat, in "Théorème d'existence pour certains systèms d'equations aux dériveés particlles nonlinéaires" in *Acta Mathematica*, **88**, 141-225, 1952.

p 21, add after eqn (2.42): "where $T = tr(T) = T^{\mu}{}_{\mu}$"

p 23, Remove sentence 2, para 2 and add at end of para 2: "It is true that the constraint equations are compatible with the evolution equations in the ADM formalism, as the Bianchi identities enforce that if the constraints are satisfied on the initial hypersurface, they will be satisfied on future hypersurfaces also. However, this analytical result does not necessarily ensure stable numerical solutions, especially considering that the ADM equations do not conform to the standard classification of partial differential equations, hyperbolic, parabolic or elliptic."

p 50, para 1, comment: "This decomposition of K_{ij} was introduced by York, in "Conformally invariant orthogonal decomposition of symmetric tensors on Remannian manifolds and the initial value problem of general relativity" in *Journal of Mathematical Physics*, **14**(4), 456-464, 1973

p 60, add after equation (4.15): "Note the decomposition given in equation (4.11) differs from the more standard form given by York, 1979, namely $A_{ij} = \Psi^{-10}\tilde{A}_{ij}$. Whilst our choice simplifies the form of the evolution equations, it also leads to a more complicated form of the momentum constraint. We are justified in this as the momentum constraint is not used to specify initial conditions in this work. However, for more general systems this complication will need to be taken into account."

p 64, para 1, comment: "Black hole excision techniques were introduced over a decade ago. For an example of the development of this technique, see Thornburg, J. "Coordinates and boundary conditions for the general relativistic initial data problem", *Classical Quantum Gravity*, **4**, 1119, 1987

p 69 add to the end of para 2: "It is true that this static boundary condition will introduce errors into the derivative values on the boundary, resulting in small reflections. It was found that these errors remained less than the errors applied to the grid for the life of the simulation. Therefore it was not deemed necessary to utilise more careful boundary conditions, in this particular case."

p125 add at the end of para 1: "One note of concern, however, for the GEM equations is the fact $tr(K)$ does not remain monotonic across the grid. This behaviour was found to persist when different time-stepping, boundary conditions and spatial derivatives were tested. This could indicate some deeper pathology of the GEM equations. This behaviour is also found to be a factor in the following chapter, where we consider non-zero shift vector spacetimes."

Gravitoelectromagnetism and the Question of Stability in General Relativity

a thesis submitted for the degree of

Doctor of Philosophy

by

Elizabeth Stark

B.Sc. (Hons)

January 18, 2004

Centre for Stellar & Planetary Astrophysics

School of Mathematical Sciences

Monash University

Australia

Contents

'When you are courting a nice girl an hour seems like a second. When you sit on a red-hot cinder a second seems like an hour. That's relativity.' - Albert Einstein

'People have stars, but they aren't the same. For travellers, the stars are guides. For other people, they're nothing but tiny lights. And for still others, for scholars, they are problems. For my businessman, they were gold. But all those stars are silent stars. You, though, will have stars like nobody else ... You'll have stars that can laugh.'
- Antoine De Saint-Exupéry, from *The Little Prince*

'Marge, I agree with you - in theory. In theory, Communism works. In theory.' - Homer J. Simpson

Abstract

In recent years the advent of gravitational wave detectors and ever-growing computer power have made the field of numerical general relativity increasingly relevant and more accessible. At the same time the need for stable and accurate numerical models of strong-field gravitational phenomena has raised many questions. The difficulties of separating physical and coordinate results, and the problem of formulating the Einstein equations in a way that produces numerically stable, results have resulted in a wide body of research.

This thesis concerns itself mainly with the question of numerical stability. We modify the standard numerical formulation of the Einstein equations [Arnowitt et al., 1962] in an attempt to produce a formalism that is better suited to numerical modelling. We use the fact that the radiative part of spacetime, represented by the Weyl tensor, may be expressed using the gravito-electric and gravito-magnetic field tensors. These tensors represent a purely gravitational field, but are mathematically analogous to the electric and magnetic fields of classical electromagnetism.

We decompose the Bianchi identities into 3+1 form which results in a system of

evolution and constraint equations for the gravito-electric and gravito-magnetic field (the gravitoelectromagnetic equations) that are analogous to the Maxwell equations in electrodynamic theory. This system of equations is then used to augment the standard equations. This removes the 3-Ricci tensor as an evolution variable, thereby making the system first order in both space and time. This property is found to result in improved convergence properties in spacetime where gauge shocks develop.

In order to test the modified formalism, we construct a one-dimensional test code. Our aim is to compare the modified and standard formulations in a range of spacetimes. As we are trying to gauge the effect of modifying the continuum equations, we use a range of standard testbed spacetimes and standard numerical techniques.

We compare and contrast the two formulations under a range of gauge conditions in both Minkowski and Schwarzschild spacetime. We find that the modified equations produce accurate, convergent and stable simulations in most of the spacetimes considered. The results here suggest that further investigation into the use of the gravitoelectromagnetism in numerical general relativity is justified.

Statement

This thesis contains no material which has been accepted for the award of any other degree or diploma in any University or other institution. To the best of my knowledge, this thesis contains no material previously published or written by another person except where due reference is made in the text.

[redacted]

Elizabeth Stark

Foreword

The modified numerical formalism published in this work was first presented at the GR16 conference, along with preliminary numerical results, based on a Schwarzschild spacetime. While the theory presented here is the same as that presented previously, the numerical results are not. This is due to the fact that further testing of the algorithm post GR16 revealed results that were less encouraging than initially thought. The initial numerical results in a maximally sliced spacetime appeared stable. However, further convergence testing revealed a coding error that lead to increased diffusion in the time-stepping algorithm. This lead to a 'smearing-out' of the coordinate shocks that usually form in this case.

The results presented herein have had this rectified, and all the test cases are designed to be as transparent and as free of additional numerical effects as is possible.

Acknowledgements

First and foremost, thank you, Stu, for everything.

Thanks and acknowledgement must go to my supervisor, Tony Lun, for the help and advice he has offered me throughout my candidature. Thanks also to all at C.S.P.A., and to all the MONash General RELativistS. Particular thanks must be given to Leo Brewin, for help and advice, to John Lattanzio for much support and encouragement, and to 'the Old Dude' for an ever friendly ear. Especial gratitude is due to Ray Burston, for never kicking me out of the office, for much fun, much beer and some of the strangest conversations I have ever taken part in.

Thanks to all the Starks, big and small, for much love, for always believing in me more than I did and for teaching me to question and argue with the best of them. To Claire and Steph, thanks for being there even you are so far away. Thanks also to the Muirs for your acceptance and support and for giving me a Melbourne family.

This thesis is sponsored by the finer things in life: kelpie dogs, Australian music, noisy red motorbikes and single malt whiskey.

Chapter 1

Introduction

1.1 The Need for Numerical Relativity

General relativity is an inherently four dimensional theory that uses geometry to describe the interactions of massive bodies and the four dimensional spacetime they are contained in. While there is no doubt that this fundamental coupling of space and time provides an elegant and powerful theory, it is not automatically conducive to describing the dynamics of evolving gravitational systems. To fully describe a four dimensional spacetime manifold we need to solve the ten coupled Einstein equations, which relate the metric on the 4-manifold, $g_{\mu\nu}$, the curvature of space (represented by the Ricci tensor, $R_{\mu\nu}$, and its trace, R) and the mass-energy tensor, $T_{\mu\nu}$. That is, we must solve

$$R_{\mu\nu} - \frac{1}{2}g_{\mu\nu}R = 8\pi T_{\mu\nu} \tag{1.1}$$

for the entire past and future of the spacetime. For physically complicated, dynamical systems, such as the collision of two or more compact objects, we are unable to provide this kind of analytical solution. Instead we need to recast the Einstein equations into an initial value (Cauchy) problem.

As the Einstein field equations are inherently four-dimensional, non-linear and self-coupled, the task of producing a Cauchy formulation is difficult. There is the additional problem that solutions to the field equations are unique only up to a diffeomorphism [Hawking and Ellis, 1973] so that solving the field equations actually results in an equivalence class of solutions. Thus, reformulating the Einstein equations into an initial value problem requires the imposition of gauge conditions to remove the extra degrees of freedom in the system (see chapter 2 for a full derivation of the initial value problem in general relativity).

The work presented herein is primarily concerned with the development and evaluation of a modified formulation of the numerical Einstein equations . The advent of gravitational wave detectors has highlighted the need for accurate and stable numerical models of dynamics in the strong field regime of general relativity, for example, the merger of binary black holes and collapse of supermassive stars. The rapid development of supercomputing and parallel programming techniques has meant that the numerical general relativity community finally has at its disposal hardware and numerical techniques capable of handling these kind of problems.

Unfortunately the major stumbling block has proved to be the mathematical structure of the equations themselves. When reformulated as an initial value problem, the

Einstein field equations are non-linear and do not conform to standard categories of hyperbolic, elliptic or parabolic partial differential equations, all of which have well understood properties and for which we have standard finite difference techniques. As stated above, there is the added problem that we must specify a gauge (in analogy with classical electromagnetism) in order to uniquely specify a system. This leads to the added complication of gauge dynamics, that is, the appearance of effects that rise from a certain choice of coordinate system, rather than from the physics of the spacetime.

The Einstein equations were first presented as an initial value problem by Arnowitt et al. [1962]. The work most commonly followed today is, however, that of York [1979] and it is on this form of the initial value problem (referred to throughout as Standard ADM, or just ADM) that we base our benchmark code. We present and test a modification of the Standard ADM equations, based on the idea of augmenting the standard equations with the Bianchi identities, which we recast as an initial value problem. The Bianchi identities are expressed in terms of the gravito-electric, $E_{\mu\nu}$, and gravito-magnetic, $B_{\mu\nu}$, conformal tensors and we refer to the test scheme as the ADM+gravitoelectromagnetic, or GEM, system.

1.2 Aims and Outline

We aim to develop a modified 3+1 formalism and to gauge its performance relative to standard theory in a range of testbed calculations and to use the results to gain some insights into the question of stability in numerical general relativity. In order to obtain meaningful results, we must be very clear about the behaviour of the spacetimes we model in order to distinguish between 'real' physics, gauge physics and behaviour caused by the form of the equations used. The aim of the game here is not to discover new physics, but to evaluate the worth of a new formalism in a range of familiar settings.

For this reason we limit the test cases considered to ones that may be modelled using one spatial dimension plus time (a 1+1 formulation). For the most part, these are spherically symmetric spacetimes. This allows us to investigate a simpler and more transparent form of the equations investigated. It also means that we have, at best, exact solutions and, at worst, a thorough understanding of the qualitative behaviour of the spacetimes under consideration. This means we can gauge error growth and convergence with confidence. We also limit ourselves to numerical techniques that are as simple as possible. That is, we implement standard boundary conditions and integration algorithms. Again, the aim in this work is to gain insight into the feasibility of the equations, not to develop new numerical techniques.

The structure of the work is as follows :

In chapter 2 we introduce the standard 3+1 formalism, referred to as the ADM system throughout the work. This provides us with a foundation from which we can construct a benchmark code, based on the standard numerical Einstein equations, that we can test our modified equations against. We also discuss some of the problems inherent in the standard approach and survey the more common approaches to dealing with them.

Chapter 3 we introduce the conformal Weyl tensor and the Bianchi identities, as expressed using the Weyl tensor. We also discuss the derivation of the Maxwell equations in special relativity as an analogy for the following work. Following Maartens and Bassett [1998] and Friedrich [1996] we construct, from the Bianchi identities, a system of constraint and evolution equations for the Weyl tensor, that have similar properties to Maxwell's equations of electromagnetism. We conclude the chapter by augmenting the standard 3+1 equations with the Bianchi identities to produce the system of equations (the GEM system) that will be the basis for the numerical work we undertake.

In Chapter 4 we reduce the general GEM equations to their simplified (1+1) form and outline the numerical techniques that were used in the development of the algorithm. We apply the algorithm and both sets of equations to evolve initial data representing perturbations of Minkowski spacetime in chapter 5. In this way we investigate the performance of the algorithm in evolving initial data with both high and low frequency perturbations. These tests are based around the standard numerical relativity testbed calculations suggested in Alcubierre et al. [2003a].

Chapter 6 investigates well-established slicings of a Schwarzschild spacetime, following the tests carried out in Bernstein [1993]. Again we evaluate the performance of the modified algorithm in handling a range of gauge phenomena, in comparison with the benchmark code. Following this, in chapter 7, we consider a slicing of the Schwarzschild spacetime, with a line element related to that discussed in Alcubierre [1997]) with non-zero shift vector.

Finally, we summarise our findings in chapter 8, outlining the major points of difference between the standard and modified equations in (1+1)-dimensions. We also suggest a range of possible extensions of the work presented here.

1.3 Notations and Conventions

Throughout this work we shall use a range of notations and conventions when presenting mathematical results. Note, in particular, the following:

- It is assumed that Greek indices run over the range $(0, \ldots, 3)$ and Roman indices run over $(1, \ldots, 3)$.
- All metrics have signature (- + + +).
- We shall use standard Einstein summation notation where vectors and tensors are denoted using indices and summation occurs over recurring indices, i.e.:

$$v^{\alpha}T_{\mu\alpha} = v^0 T_{\mu 0} + v^1 T_{\mu 1} + v^2 T_{\mu 2} + v^3 T_{\mu 3} \tag{1.2}$$

- Symmetry is denoted by round brackets around the indices affected, $A_{(\mu\nu)} = \frac{1}{2}(A_{\mu\nu} + A_{\nu\mu})$, and antisymmetry by square brackets, $A_{[\mu\nu]} = \frac{1}{2}(A_{\mu\nu} - A_{\nu\mu})$.
- The superscript $^{(4)}$ is used to denote quantities defined on the four-dimensional manifold (with respect to the 4-metric, $g_{\mu\nu}$) and the superscript $^{(3)}$ is used to denote quantities defined on a spatial hypersurface (with respect to the metric

on the hypersurface, $\perp_{\mu\nu}$). For example the 4-connection is ${}^{(3)}\Gamma^{\mu}{}_{\nu\gamma}$ and the 3-connection is ${}^{(3)}\Gamma^{i}{}_{jk}$

- Covariant differentiation with respect to the 4-metric, $g_{\mu\nu}$, is denoted by ∇_{α} and with respect to the 3-metric, $\perp_{\mu\nu}$, is denoted by D_{α}, i.e.

$$\nabla_{\alpha} W^{\mu}{}_{\nu} = \partial_{\alpha} W^{\mu}{}_{\nu} - {}^{(4)}\Gamma^{\tau}{}_{\alpha\nu} W^{\mu}{}_{\tau} + {}^{(4)}\Gamma^{\mu}{}_{\alpha\tau} W^{\tau}{}_{\nu} \tag{1.3}$$

$$D_{\alpha} W^{\mu}{}_{\nu} = \partial_{\alpha} W^{\mu}{}_{\nu} - {}^{(3)}\Gamma^{\tau}{}_{\alpha\nu} W^{\mu}{}_{\tau} + {}^{(3)}\Gamma^{\mu}{}_{\alpha\tau} W^{\tau}{}_{\nu} \tag{1.4}$$

The semi-colon notation, $W_{\mu;\nu}$ is used to denote covariant differentiation with respect to the 4-metric only. Partial differentiation is referred to by both ∂_{μ} and comma notation, $W_{\mu,\nu}$.

- As this thesis deals with the question of numerical stability it is imperative that we spell out exactly what we mean when we refer to stability. In this work we shall use the definition of stability outlined in Alcubierre et al. [2003a]. That is, a numerical simulation is unstable if the errors (whether measured through comparison with the exact solutions, or by tracking the violation of specific constraint equations that must be satisfied at all times) exhibit exponential growth. The exceptions are when exponential error growth occurs on a timescale much larger than the dynamical timescale of the system under consideration and, naturally, when the exponential growth is a consequence of the analytical problem itself.

Chapter 2

The 3+1 Formalism in General Relativity

2.1 Introduction & Motivation

The 3+1 formalism in general relativity, first introduced by Arnowitt et al. [1962] provides a mechanism for decomposing 4-dimensional quantities into their 3-space and 1-time components. Thus, we may formulate our solution as an initial value (or Cauchy) problem. We specify our metric, its first time derivative, and any hydrodynamical information on an initial, fully spatial hypersurface. This data is then propagated forward in a suitable gauge. It can be shown [Arnowitt et al., 1962] that the long term solution of this initial value problem is equivalent to solving the Einstein equations in full 4-dimensional general relativity.

The 3+1 formulation most commonly used in numerical relativity (Standard ADM) was presented by York [1979] and is actually a modification of the original formalism [Arnowitt et al., 1962]. Although Standard ADM has been studied and used for decades, it is worth reviewing, as we will be using the ideas in the development of our adjusted formalism and will be using Standard ADM to construct a benchmark code for comparison with the approach discussed in this thesis. Unless noted otherwise, we will follow the work of York [1979] and the later review given in Bernstein [1993].

2.2 Constructing the 3+1 Space-time

In order to recast the Einstein equations into an initial value problem, we must first foliate our four dimensional manifold $(\mathcal{M}, g_{\mu\nu})$ with a series of Cauchy surfaces. A Cauchy surface $(\Sigma_t, \perp_{ij})$ is defined as a closed, achronal set, for which the complete domain of dependence is the manifold, $\mathcal{M}$. The complete domain of dependence of Σ_t is the complete set of (past and future) events that may be determined through knowledge of events on Σ_t. The surface Σ_t is achronal if distinct points $p, q \in \Sigma_t$ can not be connected by a future (or past) directed timelike curve, i.e. event p does not lie in the chronological past or future of q, and vice versa. [Wald, 1984].

Consider a family of spacelike hypersurfaces $(\Sigma, \perp_{ij})$ embedded in a four-dimensional manifold $(\mathcal{M}, g_{\mu\nu})$. We define a scalar function, called the *Cauchy time function*, t, such that every level surface of t, Σ_t, is a Cauchy surface. This series of hypersurfaces provide a *foliation* of $\mathcal{M}$, that is, they are non-intersecting and space-time-filling. The Cauchy time foliation allows us to define a coordinate time curve, so that the coordinates on $\mathcal{M}$ are (t, x^1, x^2, x^3).

We define a future pointing vector, $t^\mu = (1,0,0,0)$, tangent to the coordinate time curve. The motion of observers in the direction of the vector, t^μ, can then be resolved into components tangential and normal to the hypersurface, as illustrated in figure 2.1. First, we define a unit time-like one-form, n_μ, orthogonal to the hypersurface. This implies

$$n_{[\mu}\nabla_\nu n_{\gamma]} = 0 \tag{2.1}$$

and

$$n_\sigma n^\sigma = -1 \tag{2.2}$$

From equation (2.1) it follows that there exists a positive definite scalar function, α, such that

$$n_\mu = -\alpha\nabla_\mu t = (-\alpha, 0, 0, 0) \tag{2.3}$$

The normal vector, n^μ, represents the 4-velocity of an Eulerian observer (i.e. one at rest with respect to the hypersurface). The quantity α is the lapse function, and we shall outline its role below.

A related quantity, and one that will become useful later, is the 4-acceleration of the Eulerian observers, $\overset{\bullet}{n}^\mu$, which is defined to be given by the covariant derivative of the 4-velocity, projected orthogonal to the hypersurfaces, i.e.

$$\overset{\bullet}{n}^\mu = n^\nu \nabla_\nu n^\mu \tag{2.4}$$

Thus, $\overset{\bullet}{n}^\mu$ is tangential to the hypersurface, i.e. $\overset{\bullet}{n}^\mu n_\mu = 0$. This follows directly from the above definition and equation (2.2). The 4-acceleration is also related to the lapse function via

$$\dot{n}_\nu = \perp^\mu{}_\nu \nabla_\mu (\ln \alpha) \equiv D_\nu (\ln \alpha) \tag{2.5}$$

where D_ν is the covariant derivative associated with the 3-metric, $\perp_{\mu\nu}$ (see section 2.2.1 for definition of the 3-metric).

Now we have defined a normal vector to our surface, we may also define a projection tensor, i.e.:

$$\perp_\mu{}^\nu = \delta_\mu{}^\nu + n_\mu n^\nu \tag{2.6}$$

which projects quantities in $\mathcal{M}$ onto Σ.

Knowledge of the projection tensor allows us to construct a general prescription for the projection of any geometric quantity on $\mathcal{M}$ onto a hypersurface. The full projection of a tensor quantity is

$$\perp T^{\mu_1 \ldots \mu_l}{}_{\nu_1 \ldots \nu_k} = \perp^{\alpha_1}{}_{\nu_1} \ldots \perp^{\alpha_k}{}_{\nu_k} \perp^{\mu_1}{}_{\beta_1} \ldots \perp^{\mu_l}{}_{\beta_l} T^{\beta_1 \ldots \beta_l}{}_{\alpha_1 \ldots \alpha_k} \tag{2.7}$$

The projected quantity will be spatial, that is

$$n_{\mu_i}(\perp T^{\mu_1 \ldots \mu_i \ldots \mu_l}{}_{\nu_1 \ldots \nu_k}) = n^{\nu_i}(\perp T^{\mu_1 \ldots \mu_l}{}_{\nu_1 \ldots \nu_i \ldots \nu_k}) = 0 \tag{2.8}$$

This allows us to decompose four-dimensional quantities into their components in a

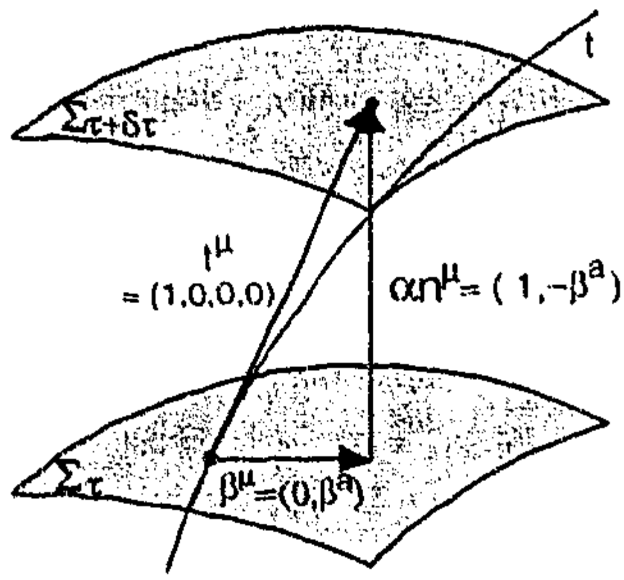

Figure 2.1: *Spacetime foliation, showing the hypersurfaces, the coordinate time and the gauge variables, α and β^μ*

timelike and spacelike direction. For example, a rank-2 tensor may be written as

$$T_{\mu\nu} = \perp T_{\mu\nu} - (\perp T_{\mu\tau} n^\tau) n_\nu - (\perp T_{\tau\nu} n^\tau) n_\mu + T_{\sigma\tau} n^\sigma n^\tau n_\mu n_\nu \tag{2.9}$$

and the extension to higher dimensional tensors is straightforward. In particular, the projection of t^μ gives us β^μ, which we shall refer to as the shift vector. The shift vector is defined as follows:

$$\beta^\mu = \perp^\mu{}_\sigma t^\sigma \tag{2.10}$$

As illustrated in figure 2.1 the coordinate time curve tangent vector may then be expressed as

$$t^\mu = \alpha n^\mu + \beta^\mu \tag{2.11}$$

Note that $t^{\mu} = (1, 0, 0, 0)$ regardless of the lapse and shift as it is, by definition, tangent to the coordinate time curve, t. The coordinate time curve, however, is dependant on the lapse and shift and may be completely specified in terms of them and the normal vector. Thus the lapse, α, and shift vector, β^i, are purely gauge variables and may be chosen arbitrarily. The choice of α determines the structure of the foliation of surfaces. The choice of β^i is arbitrary at each point, and a particular choice leads to a particular family of curves 'threading the slices of Σ' [York, 1979].

2.2.1 Hypersurface Structure

The description of the slices is governed by the knowledge of two basic quantities, the *induced metric* of the slice, $\perp_{\mu\nu}$, and the *extrinsic curvature*, $K_{\mu\nu}$. The former is simply given by the projection of the 4-metric onto the slice.

$$\perp_{\mu\nu} = g_{\mu\nu} + n_\mu n_\nu \tag{2.12}$$

c.f. equation (2.6).

The *covariant derivative on the slice*, D_μ is obtained by projecting its 4-dimensional analog, ie

$$D_\sigma T^\mu{}_\nu = \perp \nabla_\sigma T^\mu{}_\nu \tag{2.13}$$

where T^μ_ν is an arbitrary spatial mixed tensor. Once we have assumed this form we can show that D_σ does indeed satisfy the properties of a covariant derivative (as given by Wald [1984], section 3.1). In particular, D_σ satisfies

- Linearity:

$$D_\mu(xA^{a_1\cdots a_k}_{b_1\cdots b_l} + yB^{a_1\cdots a_k}_{b_1\cdots b_l}) = xD_\mu A^{a_1\cdots a_k}_{b_1\cdots b_l} + yD_\mu B^{a_1\cdots a_k}_{b_1\cdots b_l} \tag{2.14}$$

where $x, y \in \Re$ and A, B are tensors of rank (k, l).

- Leibniz Rule:

$$D_\mu[A^{a_1\cdots a_k}_{b_1\cdots b_l} B^{a_1\cdots a_k}_{b_1\cdots b_l}] = B^{a_1\cdots a_k}_{b_1\cdots b_l} D_\mu[A^{a_1\cdots a_k}_{b_1\cdots b_l}] + A^{a_1\cdots a_k}_{b_1\cdots b_l} D_\mu[B^{a_1\cdots a_k}_{b_1\cdots b_l}] \tag{2.15}$$

It is important to note that D_μ is still a 4-dimensional operator, and is designed to act on 4-dimensional *spatial* tensors. A further important property of the spatial derivative is

$$\begin{aligned} D_\mu \perp_{\alpha\beta} &= \perp^\delta_\sigma \perp^\beta_\nu \perp^\alpha_\mu \nabla_\delta(n_\alpha n_\beta) \\ &= \perp^\delta_\sigma [n_{\mu;\delta} n_\nu + n_\nu n_\mu n^\alpha n_{\alpha;\delta} - n_{\mu;\delta} n_\nu - n_\nu n_\mu n^\alpha n_{\alpha;\delta}] \equiv 0 \end{aligned} \tag{2.16}$$

as expected in comparison to the 4-dimensional case ($\nabla_\mu g_{\alpha\beta} = 0$).

Contractions of the 4-dimensional Riemann tensor, ${}^{(4)}R_{\mu\nu\alpha\beta}$, provide important information about the 4-dimensional spacetime curvature. The 3-dimensional Riemman tensor, ${}^{(3)}R_{\mu\nu\alpha\beta}$, is defined analogously to its 4-dimensional counterpart. That is, for arbitrary one-forms, v_σ and w_σ, (with w_σ spatial),

$$v_\gamma {}^{(4)}R_{\mu\nu\sigma}{}^\gamma = (\nabla_\mu\nabla_\nu - \nabla_\nu\nabla_\mu)v_\sigma \tag{2.17}$$

$$w_\gamma {}^{(3)}R_{\mu\nu\sigma}{}^\gamma = (D_\mu D_\nu - D_\nu D_\mu)w_\sigma \tag{2.18}$$

In order to translate information about the metric and curvature of the hypersurfaces into information about the 4-dimensional spacetime we need to know how the slices, Σ, are embedded in $\mathcal{M}$. That is, we need to define the extrinsic curvature (or second fundamental form) of the slices. The extrinsic curvature, $K_{\mu\nu}$, is obtained from the 3-covariant derivative of the normal vector:

$$
\begin{aligned}
K_{\mu\nu} &= D_\mu n_\nu \\
&= - \perp^\sigma_\mu \perp^\tau_\nu \nabla_\sigma n_\tau \equiv - \perp^\sigma_\mu \nabla_\sigma n_\nu
\end{aligned}
\tag{2.19}
$$

(For the third identity we have used the definition of the projection tensor (2.6) and the identity $n^\tau n_\tau \nabla_\mu n^\tau = 0$.) This also leads to the important result that

$$
\nabla_\mu n_\nu = -K_{\mu\nu} - n_\mu \dot{n}_\nu \tag{2.20}
$$

from equation (2.4). $K_{\mu\nu}$ is symmetric, i.e. $K_{\mu\nu} = K_{(\mu\nu)} = \frac{1}{2}(K_{\mu\nu} + K_{\mu\nu})$. This follows from equations (2.20) and (2.1).

We now have the tools needed to construct the constraint equations governing the components of the Riemann tensor on each slicing. In fact, we find that we are able to constrain the 4-dimensional Riemann tensor, ${}^{(4)}R_{\mu\nu\alpha\beta}$, entirely in terms of spatial components.

2.2.2 Hypersurface Curvature & Constraint Equations

In order to split the Einstein equations into their 3+1 form, we first consider the Riemann tensor. The three components of the decomposition of ${}^{(4)}R_{\mu\nu\alpha\beta}$ leads to the set of equations known as the Gauss-Codazzi-Ricci equations. These equations are

- Gauss equation:

$$\perp {}^{(4)}R_{\mu\nu\alpha\beta} = {}^{(3)}R_{\mu\nu\alpha\beta} + K_{\mu\alpha}K_{\nu\beta} - K_{\mu\beta}K_{\nu\alpha} \tag{2.21}$$

- Codazzi Equation:

$$\perp {}^{(4)}R_{\mu\nu\alpha\sigma}n^{\sigma} = D_{\nu}K_{\mu\alpha} - D_{\mu}K_{\nu\alpha} \tag{2.22}$$

- Ricci Equation:

$$\begin{aligned} \perp {}^{(4)}R_{\mu\nu\alpha\beta}n^{\mu}n^{\alpha} &= n^{\alpha}\nabla_{\alpha}K_{\nu\beta} + K_{\alpha\nu}\nabla_{\beta}n^{\alpha} \\ &+ K_{\alpha\beta}\nabla_{\nu}n^{\alpha} + K_{\nu\alpha}K^{\alpha}_{\beta} + \alpha^{-1}D_{\nu}D_{\beta}\alpha \end{aligned} \tag{2.23}$$

Equation (2.21) is obtained from the projection of all indices of ${}^{(4)}R_{\mu\nu\alpha\beta}$ onto the hypersurface, using equation (2.7). This removes all terms involving normal components, leaving only terms involving ${}^{(3)}R_{\mu\nu\alpha\beta}$ and $K_{\mu\nu}$. Equation (2.22) follows from a single projection along the normal and subsequent projection of the remaining three indices onto the hypersurface. Similarly, equation (2.23) follows from double projection along the normal. Due to the symmetries of the Ricci tensor, contraction of more than two indices with the normal will yield a zero result [Bernstein, 1993].

The total decomposition of $R_{\mu\nu\alpha\beta}$ is then found from the definition (2.9) which is then simplified using equations (2.21) - (2.23) to obtain:

$$\begin{aligned}
{}^{(4)}R_{\mu\nu\gamma\beta} = {}& {}^{(3)}R_{\mu\nu\gamma\beta} + K_{\mu\gamma}K_{\nu\beta} - K_{\mu\beta}K_{\nu\gamma} \\
& + n_\mu n_\gamma (n^\sigma \nabla_\sigma K_{\nu\beta} + K_{\nu\sigma}\nabla_\beta n^\sigma + K_{\sigma\beta}\nabla_\nu n^\sigma + K_{\nu\sigma}K^\sigma{}_\beta + \alpha^{-1}D_\nu D_\beta \alpha) \\
& - n_\nu n_\gamma (n^\sigma \nabla_\sigma K_{\mu\beta} + K_{\mu\sigma}\nabla_\beta n^\sigma + K_{\sigma\beta}\nabla_\nu n^\sigma + K_{\mu\sigma}K^\sigma{}_\beta + \alpha^{-1}D_\mu D_\beta \alpha) \\
& + n_\nu n_\beta (n^\sigma \nabla_\sigma K_{\mu\gamma} + K_{\mu\sigma}\nabla_\gamma n^\sigma + K_{\sigma\gamma}\nabla_\mu n^\sigma + K_{\mu\sigma}K^\sigma{}_\gamma + \alpha^{-1}D_\mu D_\gamma \alpha) \\
& - n_\mu n_\beta (n^\sigma \nabla_\sigma K_{\nu\gamma} + K_{\nu\sigma}\nabla_\gamma n^\sigma + K_{\sigma\gamma}\nabla_\nu n^\sigma + K_{\nu\sigma}K^\sigma{}_\gamma + \alpha^{-1}D_\nu D_\gamma \alpha) \\
& - 2(n_\mu D_{[\gamma}K_{\beta]\nu} + n_\nu D_{[\beta}K_{\gamma]\mu} + n_\gamma D_{[\mu}K_{\nu]\beta} + n_\beta D_{[\nu}K_{\mu]\gamma})
\end{aligned} \tag{2.24}$$

For a complete picture we need to consider the presence of a matter distribution with arbitrary mass-energy tensor $T_{\mu\nu}$. The mass-energy tensor may be decomposed using equation (2.9) to be expressed entirely in terms of hypersurface parameters:

$$T_{\mu\nu} = S_{\mu\nu} + 2j_{(\mu}n_{\nu)} + \rho n_\mu n_\nu \tag{2.25}$$

where

$$\begin{aligned}
S_{\mu\nu} &:= \perp T_{\mu\nu} \\
j^\mu &:= - \perp (T^{\mu\alpha}n_\alpha) \\
\rho &:= T^{\alpha\beta}n_\alpha n_\beta
\end{aligned} \tag{2.26}$$

$S_{\mu\nu} = \pi_{\mu\nu} + \perp_{\mu\nu} P$ where $\pi_{\mu\nu}$ and P are the anisotropic and isotropic pressure respectively, j^μ represents energy flux and ρ the energy density of the fluid. Note that

$\pi_{\mu\nu} = \pi_{\langle\mu\nu\rangle}$ and $tr(\pi) = \pi^{\sigma}{}_{\sigma} = 0$. The hydrodynamical quantities are obtained for a given matter distribution by specifying an equation of state and considering the twice contracted Bianchi identities, which are discussed in more detail in section 3.4.4.

We may also construct the Einstein tensor from the definition

$$^{(4)}G_{\mu\nu} = {}^{(4)}R_{\mu\nu} - \frac{1}{2}g_{\mu\nu}{}^{(4)}R \tag{2.27}$$

Using equation (2.24) we can project the Einstein equations (1.1) along the direction of the normal vector to yield the constraint equations:

$$2n^{\mu}n^{\nu(4)}G_{\mu\nu} \equiv {}^{(3)}R + tr(K)^2 - K_{\mu\nu}K^{\mu\nu} = 2\kappa\rho \tag{2.28}$$

$$-\perp^{\mu}_{\tau} n^{\nu}G^{\tau}{}_{\nu} \equiv D_{\nu}(K^{\mu\nu} - \perp^{\mu\nu} K) = \kappa j^{\mu} \tag{2.29}$$

where $^{(3)}R$ refers to the spatial Ricci scalar, $\kappa = 8\pi$ and $tr(K) = \perp^{\mu\nu} K_{\mu\nu} = g^{\mu\nu}K_{\mu\nu}$. These are the *Hamiltonian constraint* and the *momentum constraints* respectively. Equation (2.28) produces a scalar while equation (2.29) returns a spatial vector, hence the combined hypersurface components (i.e. the indices from 1-3) of the constraint equations provide four of the ten independent equations needed to specify the system.

2.3 Propagation of Hypersurface Parameters

The remaining six Einstein equations prescribe the evolution of the hypersurface and we shall outline their derivation in this section.

2.3.1 Lie Derivatives

One of the most important tools in our development of the 3+1 problem is the concept of the Lie derivative (see Hawking and Ellis [1973] for a full description of the Lie derivative's properties). We shall define it in terms of its action on various fields. For example, the Lie derivative of a scalar field, f, is analogous to a directional derivative along a given vector field X^μ.

$$£_X f = X^\sigma \nabla_\sigma f = X^\sigma f_{,\sigma} \tag{2.30}$$

For a vector field, V^μ, it is given by

$$£_X V^\mu = X^\sigma \nabla_\sigma V^\mu - V^\sigma \nabla_\sigma X^\mu \tag{2.31}$$

and finally for a tensor field, $T^\mu{}_\nu$, we have

$$£_X T^\mu{}_\nu = X^\sigma \nabla_\sigma T^\mu{}_\nu - T^\sigma{}_\nu \nabla_\sigma X^\mu + T^\mu{}_\sigma \nabla_\nu X^\sigma \tag{2.32}$$

An additional important property of the Lie derivative is its action on the projection tensor. Using the definition of the Lie derivative (2.32) and equations (2.5) and (2.12) we find

$$£_n \perp^\nu{}_\mu = 0 \tag{2.33}$$

where n^μ is the velocity of the 4-observers that was introduced in section 2.2.

The evolution equations are derived by considering the Lie derivative of $\perp_{\mu\nu}$ and $K_{\mu\nu}$

along the curve t^μ. By linearity of the Lie derivative:

$$\pounds_t = \pounds_{\alpha n+\beta} \tag{2.34}$$

$$= \alpha\pounds_n + \pounds_\beta \tag{2.35}$$

Now we are ready to construct the evolution equations for initial data (the 3-metric, $\perp_{ij}$, and extrinsic curvature, $K_{(ij)}$) specified on a hypersurface.

2.3.2 Propagation along t^μ

Consider the Lie derivative of the 3-metric in the n^μ direction. We find:

$$\pounds_n \perp_{\mu\nu} = n^\sigma\nabla_\sigma \perp_{\mu\nu} + \perp_{\sigma\nu} \nabla_\mu n^\sigma + \perp_{\sigma\mu} \nabla_\nu n^\sigma \tag{2.36}$$

$$= n^\sigma n_\mu \nabla_\sigma n_\nu + n^\sigma n_\nu \nabla_\sigma n_\mu + \perp^\sigma{}_\nu \nabla_\mu n_\sigma + \perp^\sigma{}_\mu \nabla_\nu n_\sigma \tag{2.37}$$

But from equation (2.20) and (2.5) we have

$$n^\sigma n_\mu \nabla_\sigma n_\nu \equiv n_\mu \dot{n}_\nu = -K_{\mu\nu} - \nabla_\mu n_\nu \tag{2.38}$$

so

$$\pounds_n \perp_{\mu\nu} = -K_{\mu\nu} - \nabla_\mu n_\nu + -K_{\nu\mu} - \nabla_\nu n_\mu + (\delta^\sigma_\nu + n^\sigma n_\nu)\nabla_\mu n_\sigma$$
$$+ (\delta^\sigma_\mu + n^\sigma n_\mu)\nabla_\nu n_\sigma \tag{2.39}$$

$$\tag{2.40}$$

Thus, by the symmetry of $K_{\mu\nu}$ the evolution of $\perp_{\mu\nu}$ along n^{σ} is given by

$$\pounds_n \perp_{\mu\nu} = -2K_{\mu\nu} \tag{2.41}$$

The Lie derivative of the extrinsic curvature along n^{μ} is obtained through the full projection of the Einstein equations (1.1) expressed as

$$\perp^{(4)} R_{\mu\nu} = \kappa \perp (T_{\mu\nu} - \frac{1}{2} g_{\mu\nu} T) \tag{2.42}$$

The right-hand side is expressed using purely spatial quantities through the definition of the mass-energy tensor (2.25). The left-hand side is obtained by taking the projection of the Gauss equation (2.21) along the 3-metric which yields

$$\perp^{(4)} R_{\mu\nu} + \perp^{(4)} R_{\mu\sigma\nu\tau} n^{\sigma} n^{\tau} = ^{(3)} R_{\mu\nu} + tr(K) K_{\mu\nu} - K_{\mu\sigma} K^{\sigma}{}_{\nu} \tag{2.43}$$

Using the Ricci equation (2.23) and noticing that it includes the Lie derivative of the extrinsic curvature leads to our next set of evolution equations:

$$\begin{aligned} \pounds_n K_{\mu\nu} = & ^{(3)} R_{\mu\nu} + tr(K) K_{\mu\nu} - 2 K_{\mu\sigma} K^{\sigma}{}_{\nu} - \alpha^{-1} D_{\mu} D_{\nu} \alpha \\ & - \kappa(\pi_{\mu\nu} - \frac{1}{2} \perp_{\mu\nu} P) \end{aligned} \tag{2.44}$$

In order to use this information to construct time derivatives of our evolution variables, we remember that we have defined the tangent to our coordinate time curve (section 2.2) as

$$t^{\mu} = (1,0,0,0) \equiv \partial_t \tag{2.45}$$

Thus $\pounds_t \equiv \partial_t$. Using equation (2.35) we then obtain the general evolution equations for $\perp_{\mu\nu}$ and $K_{\mu\nu}$ along the coordinate time curve:

$$(\partial_t - \pounds_\beta) \perp_{\mu\nu} = -2\alpha K_{\mu\nu} \tag{2.46}$$

and

$$\begin{aligned}(\partial_t - \pounds_\beta)K_{\mu\nu} &= \alpha({}^{(3)}R_{\mu\nu} + tr(K)K_{\mu\nu} - 2K_{\mu\sigma}K^{\sigma}{}_{\nu}) - D_\mu D_\nu \alpha \\ &\quad - \kappa\alpha(\pi_{\mu\nu} - \frac{1}{2} \perp_{\mu\nu} P)\end{aligned} \tag{2.47}$$

If we take a moment to do some counting, we notice that the spatial components (i.e. letting the index run from 1-3) of the evolution equations for the 3-metric (2.46) represent the remaining six independent and non-trivial components of the Einstein equations. Note also that these equations do not constrain the four gauge functions, i.e. the lapse function, α, and shift vector, β^i. We are free to specify these. Once we have done so, the coupled system of evolution equations, (2.46) and (2.47), the four constraint equations given by the Hamiltonian and momentum constraints, (2.28) and (2.29), along with evolution of any matter source terms provides us with the ten independent components of the Einstein equations, posed as a Cauchy problem.

2.4 The Question of Stability

To solve for a complete spacetime using the Standard ADM formalism we firstly specify our 3-metric and extrinsic curvature (according to the constraint equations) on a Cauchy surface of our choosing. We shall pretend for the purposes of this thesis that this is a straightforward task, as the initial conditions for the spacetimes we consider are easily specified. As the aim of the game in this work is to study the behaviour of the evolution the question of initial conditions is tangential. There are, however a number of interesting review papers on the topic for the interested reader, for example Cook [2000].

Before we introduce the modified formalism in the following chapter, we need to provide some justification for why any modification is considered necessary. Firstly, the equations as they are presented above are not, in general, well-posed or hyperbolic. A system of equations is well posed if we can show the existence and uniqueness of a solution, and that the solution depends continuously on the initial values. That is, if the constraints are satisfied initially they will be satisfied for subsequent hypersurfaces, if the problem is well posed*. [Brügmann, 2000]

This has lead to a large body of work aimed at the modification of the standard ADM equations to obtain a hyperbolic formulation. The major advances in this area are reviewed in Reula [1998]. To date, the hyperbolic formulations of the 3+1 equations have not shown themselves to have significant numerical stability advantages over the standard equations.

*although well-posedness in an analytical sense will not necessarily ensure the constraints remain bounded in a numerical setting

Secondly, there is the problem of 'gauge modes'. The specification of a gauge (α and β^i) is only enough to constrain the metric and extrinsic curvature up to a coordinate transformation. It remains possible to transform the metric-extrinsic curvature pair without changing the form of the lapse and shift functions. If the transformed solution satisfies the constraint equations, this gauge constraint can, depending on the speed of propagation of the mode, lead to unstable numerical results [Kelly et al., 2001].

A great deal of work has been done in trying to understand the mathematical nature of the stabilities in both linearised and full-field general relativity. For example, the work of Gen Yoneda and Hisa-aki Shinkai has dealt with the stability question through the eigenvalue analysis of propagation equations for the constraint equations (for a recent review see Shinkai and Yoneda [2002]). Their methodology requires an eigenvalue analysis of the full non-linear constraint propagation equations, but an insight into stability can be gleaned by restricting ourselves to the linear regime, namely be considering the behaviour of linear perturbations on a Minkowski background.

Here we consider the theory as presented in Alcubierre et al. [2000]. By considering a metric of the form

$$\perp_{ij}= \delta_{ij} + \epsilon_{ij} \tag{2.48}$$

where $|\epsilon_{ij}| << 1$ we can derive linearised versions of the ADM evolution, and constraint equations. If we then slice the spacetime such that observers fall along geodesics

($\alpha = 1, \beta^i = 0$) the linearised ADM system is [Alcubierre et al., 2000]

$$\partial_t \epsilon_{ij} = -2K_{ij} + h.o. \tag{2.49}$$

$$\partial_t K_{ij} = {}^{(3)}R_{ij}^{(linear)} + h.o. \tag{2.50}$$

where ${}^{(3)}R_{ij}^{(linear)} = \frac{1}{2}(-\partial_m \partial^m \epsilon_{ij} - \partial_i \partial_j tr(\epsilon) + \partial_i \partial_m \epsilon^m{}_j + \partial_m \partial_j \epsilon_i{}^m)$ is the linearised Ricci tensor and $h.o.$ represents all terms of higher than linear order. The linearised constraint equations are given by

$$H = \partial_m(\partial_n \epsilon^{mn} - \partial^m tr(\epsilon)) = 0 \tag{2.51}$$

$$M^i = \partial_i(\partial_m \epsilon^{im} - \partial^i tr(\epsilon)) = 0 \tag{2.52}$$

We assume a solution of the form of a plane wave travelling in the x-direction, i.e.

$$\perp_{ij} = \hat{\perp}_{ij} e^{i(\omega t - kx)} \tag{2.53}$$

$$K_{ij} = \hat{K}_{ij} e^{i(\omega t - kx)} \tag{2.54}$$

Substituting this into equations (2.49) and (2.50) and expressing the metric as a vector, $\hat{\perp}_{ij} = (\hat{\perp}_{xx}, \hat{\perp}_{yy}, \hat{\perp}_{zz}, \hat{\perp}_{xy}, \hat{\perp}_{xz}, \hat{\perp}_{yz})$ allows us to reduce the set of equations to an eigenproblem for $\hat{\perp}_{ij}$. The probiem admits two eigenvalues, $\lambda = 0$ and $\lambda = 1$ and six eigenvectors. Of these solutions, twc represent the physical gravitational wave (i.e. they travel with speed one and are transverse and traceless), three modes violate at least one constraint and one satisfies all the constraints, (2.51) and (2.52), and propagates with zero speed.

This last solution is the one that is most worrisome. This is not a physical solution, it is a pure gauge phenomenon and, as it exhibits zero speed, can never propagate off a numerical grid. Thus, numerical integrations using the ADM equations, in some gauges at least, will exhibit a constraint violation that grows with time, leading to an unstable evolution.

Of the great number of modifications to the standard equations that have been proposed, the most widely accepted at this point is the system presented in Baumgarte and Shapiro [1999], based on the conformal, trace-split system of Shibata and Nakumara [Shibata and Nakamura, 1995]. The crux of this modification is, firstly, the use of the conformal metric, $\tilde{\gamma}_{ij} = e^{-4\phi}\,\gamma_{ij}$, where $e^{4\phi} = (\det\gamma)^{1/3}$. The evolution of the metric function is now split into two equations, one for the conformal factor, ϕ and one for the conformal metric, $\tilde{\gamma}_{ij}$. The evolution equation for the extrinsic curvature is also split into its trace and trace-free parts, which are evolved separately.

Secondly, the conformal connection functions are raised to evolution variables through the introduction of the kinematic quantity $\tilde{\Gamma}^i \equiv \tilde{\gamma}^{jk}\tilde{\Gamma}^i{}_{jk}$. This quantity also allows the definition of the 3-Ricci tensor to be recast in elliptic form, making it more conducive to numerical computation. Furthermore, the evolution equation for $\tilde{\Gamma}^i$ incorporates the momentum constraint. It can be shown [Knapp et al., 2002] that this modification has an important effect on the constraint-satisfying gauge mode. In the BSSN formalism, this mode propagates at the speed of light, thus enabling it to propagate off the numerical grid, resulting in a more stable integration.

Chapter 3

Gravitoelectromagnetism

3.1 Motivation

In this chapter we propose a modification of the Standard ADM equations, with a view to improving their stability properties. We propose to include the Bianchi identities to the existing Standard ADM Cauchy system. This will change the existing system of equations and will add in extra equations. The extra equations are formed from the Bianchi identities and bear a strong resemblance to the Maxwell equations of classical electromagnetism.

The Bianchi identities and their 3+1 decomposition are not new but (to the best of our knowledge) their use in augmenting the Standard ADM equation and the development of a numerical code with this modified formalism, is. Firstly, we shall outline some of the previous applications of these equations (section 3.2). We shall also review the equations of classical electromagnetism in section 3.3, before we spend the remainder of the chapter in building the gravitoelectromagnetism (GEM) formalism. The general form of the 3+1+GEM equations that shall be used in this work are presented in section 3.5.

3.2 Previous Work

The work that is closest in philosophy to that undertaken here is Friedrich [1996]. Friedrich introduced the idea of using the Bianchi identities as part of a hyperbolic reduction of the Einstein field equations. The Weyl conformal tensor (section 3.4.3) in a vacuum can be shown to propagate according to hyperbolic equations regardless of gauge.

The Weyl conformal tensor and the Bianchi identities also play a large part in the work done in the field of cosmology by Ellis (see, for example Ellis [1973]). In order to carry out the decomposition we modify Ellis' approach slightly. The major differences between Ellis' approach and standard ADM may be seen by comparing figure 3.1 and figure 2.1.

Ellis considers local hypersurfaces that are co-moving with a congruence of observers who are moving through spacetime. We observe that the congruence approach does not require the spacetime to admit a global foliation of hypersurfaces. There is still a strong and obvious analogy between the two approaches, as the congruence approach

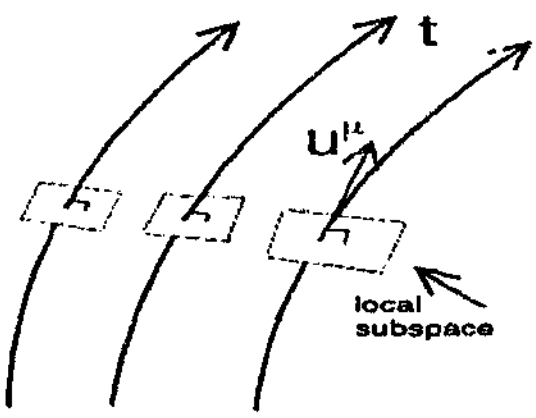

Figure 3.1: *Representation of the spacetime foliation in the congruence of observers method of Ellis. Here $u^\mu = \frac{dx^\mu}{dt}$ is the co-moving velocity of the observer. We consider projection of 4-dimensional quantities into the* **local** *subspaces of the observers.*

splits the spacetime into its three space and one time components, though only in a local sense. The congruence method equations are complicated, however, by the appearance of vorticity terms arising from the rotation of the observers. These terms do not appear in the ADM case due to the imposition of global hypersurfaces.

In this work we assume the existence of a global foliation of hypersurfaces (i.e. there will be no vorticity terms in our equations). We will, however, follow the methodology and some of the notation of Ellis.

3.3 Relativistic Electromagnetism

In order to formulate the fully covariant 3+1 form of the Einstein equations plus Bianchi identities we consider an analogy to classical electromagnetic theory. For simplification, we consider the equations in Minkowski spacetime, i.e.

$$g_{\mu\nu} = \eta_{\mu\nu} = (-1, 1, 1, 1) \tag{3.1}$$

where the normal special relativistic definitions apply.

The classical electromagnetic field is described by the two fundamental vectors: the electric (**E**) and magnetic (**B**) fields. The evolution of these fields in a vacuum are described by the set of evolution and constraint equations known as the microscopic Maxwell equations, which are [Barut, 1980]:

$$\partial_t \mathbf{B} + \nabla \times \mathbf{E} = 0 \tag{3.2}$$

$$\partial_t \mathbf{E} - \nabla \times \mathbf{B} = -\mathbf{j}^{(em)} \tag{3.3}$$

$$\nabla \cdot \mathbf{B} = 0 \tag{3.4}$$

$$\nabla \cdot \mathbf{E} = \rho^{(em)} \tag{3.5}$$

Here $\mathbf{j}^{(em)}$ is the current density and $\rho^{(em)}$ is the charge density (the (em) superscript differentiates them from the energy flux and energy density defined in the preceding chapter). $\nabla \equiv (\frac{\partial}{\partial x^1}, \frac{\partial}{\partial x^2}, \frac{\partial}{\partial x^3})$ is the standard flat-space gradient operator.

It is then common practice to define scalar and a vector potentials:

$$\mathbf{B} = \nabla \times \mathbf{A} \tag{3.6}$$

$$\nabla \phi = -\mathbf{E} - \partial_t \mathbf{A} \tag{3.7}$$

The definition of the vector potential, **A**, (equation (3.6)) follows from equation (3.4) and the definition of the scalar potential, ϕ (equation (3.7)) follows from equation (3.2). This allows us to rework the Maxwell equations into evolution equations for the gauge potentials, to obtain

$$(-\partial_t^2 + \Delta)\phi = -\rho^{(em)} - \partial_t(\nabla \cdot \mathbf{A} + \partial_t\phi) \tag{3.8}$$

$$(-\partial_t^2 + \Delta)\mathbf{A} = -\mathbf{j}^{(em)} + \nabla(\nabla \cdot \mathbf{A} + \partial_t\phi) \tag{3.9}$$

where $\Delta \equiv (\frac{\partial^2}{\partial(x^1)^2}, \frac{\partial^2}{\partial(x^2)^2}, \frac{\partial^2}{\partial(x^3)^2})$ is the flat-space Laplacian operator. The set of equations (3.6) - (3.9) are equivalent to the Maxwell equations (3.2) - (3.5).

In this chapter we will be deriving the general relativistic counterparts to equations (3.2) - (3.5). In order to draw comparisons between the two theories we shall reformulate the above equations into tensorial form. We define the field tensor $F_{\mu\nu}$ by

$$F_{\mu\nu} = \begin{bmatrix} 0 & -E_1 & -E_2 & -E_3 \\ E_1 & 0 & B_3 & -B_2 \\ E_2 & -B_3 & 0 & B_1 \\ E_3 & B_2 & -B_1 & 0 \end{bmatrix}$$

Likewise we define the 4-potential (A^μ) and the 4-current (J^μ)

$$A^\mu = (\phi, A^i) \tag{3.10}$$

$$J^\mu = (\rho, j^i) \tag{3.11}$$

The definitions of the scalar and vector potentials, (3.6) and (3.7), are equivalent to

$$F_{\mu\nu} = \partial_\mu A_\nu - \partial_\nu A_\mu \tag{3.12}$$

The Maxwell equations may then be expressed in tensorial form thus:

$$\partial_\beta F^{\mu\beta} = J^\mu \tag{3.13}$$

$$\partial_{[\alpha} F_{\beta\gamma]} = 0 \tag{3.14}$$

Note that equations (3.12)-(3.14) are invariant under the transformation

$$A^\mu \rightarrow A^\mu + \frac{\partial\chi}{\partial x^\mu} \tag{3.15}$$

where χ is an arbitrary scalar function. This gives us the freedom to specify different gauge choices, by placing conditions on the potentials, A and ϕ. Two common examples are the Coulomb gauge:

$$\nabla \cdot \mathbf{A} = 0 \tag{3.16}$$

and the Lorentz gauge:

$$\nabla \cdot \mathbf{A} + \frac{\partial^2\phi}{\partial t^2} = 0 \tag{3.17}$$

We can see from this brief look at electromagnetism that the approach to modelling a classical electromagnetism problem differs from the approach often taken in general relativity. In electromagnetic theory we see that we start by ascribing the two fields, **E** and **B**. We then see that the Maxwell equations imply the existence of the potentials, **A** and ϕ, which generate the electric and magnetic field.

This is the opposite of general relativity where, with knowledge of the 'gravitational potentials' (the metric coefficients) one can calculate the 'fields' (the curvature of spacetime). By solving the Einstein equations (in this case using the 3+1 formalism) we obtain the fields generated by the potentials (that is, we solve the evolution and constraint equations for the ten components of the spacetime metric). The Bianchi identities (which we shall see are analogous to the Maxwell equations) provide the integrability conditions for the Einstein equations but, traditionally, are not used in obtaining a solution.

The reworking of the 3+1 formalism that we provide in this chapter sees us taking an approach that is closer in philosophy to that used in classical electromagnetism (following the work done by G.F.R. Ellis in particular). That is to say, we use the Bianchi identities in analogy with the Maxwell equations to provide evolution and constraint equations for gravito-electric and gravito-magnetic field. The 3+1 Einstein equations, augmented with the Bianchi identities, allow us to solve gravitational potentials, which in turn, generate the gravitational field.

3.4 The Gravitoelectrodynamic Equations

3.4.1 A Toolkit

Before we embark on the main aims of this chapter it is worth spending a moment considering a few quantities that we will need along the way (i.e. we must build a toolkit for the derivation). Firstly, we consider the alternating pseudo-tensor, $\varepsilon_{\mu\nu\alpha\beta}$. We define this as

$$\varepsilon_{\mu\nu\sigma\tau} = \sqrt{-\det(g)}\ 4!\ \delta^0_{[\mu}\delta^1_\nu\delta^2_\sigma\delta^3_{\tau]} \tag{3.18}$$

$$\varepsilon^{\mu\nu\sigma\tau} = \frac{-1}{\sqrt{-\det(g)}}\ 4!\ \delta^{[\mu}_0\delta^\nu_1\delta^\sigma_2\delta^{\tau]}_3 \tag{3.19}$$

The 4-volume element is then

$$\begin{aligned} dV &:= \sqrt{-\det(g)}\, dx^0 dx^1 dx^2 dx^3 \\ &= \varepsilon_{\mu\nu\alpha\beta} dx^\mu dx^\nu dx^\alpha dx^\beta \end{aligned} \tag{3.20}$$

Note that this implies $\varepsilon_{0123} = +\sqrt{-\det(g)}$, which gives our pseudo-tensor the opposite sign to that defined in the work of Ellis et. al. (for example Ellis [1973] and Ellis [1971]).

We define the alternating tensor associated with the 3-volume element as

$$\varepsilon_{\mu\nu\alpha} = \varepsilon_{\tau\mu\nu\alpha} n^\tau \tag{3.21}$$

The 4-alternating tensor may be decomposed as

$$\varepsilon_{\mu\nu\alpha\beta} = \varepsilon_{\mu\nu\alpha} n_\beta + \varepsilon_{\mu\alpha\beta} n_\nu - \varepsilon_{\mu\nu\beta} n_\alpha - \varepsilon_{\nu\alpha\beta} n_\mu \tag{3.22}$$

The 3-alternating tensor may also be defined in terms of the 3-metric, via:

$$\varepsilon_{\mu\nu\alpha} = \sqrt{\det(\perp)}\, 3!\ \perp^0{}_{[\mu} \perp^1{}_\nu \perp^2{}_{\alpha]} \tag{3.23}$$

$$\varepsilon^{\mu\nu\alpha} = \frac{-1}{\sqrt{\det(\perp)}}\, 3!\ \perp^{[\mu}{}_0 \perp^\nu{}_1 \perp^{\alpha]}{}_2 \tag{3.24}$$

and it has the following important properties

1. $\varepsilon_{\mu\nu\alpha} n^\alpha = 0$ (i.e. $\varepsilon_{\mu\nu\alpha}$ is spatial)

2. $D_\alpha \varepsilon_{\mu\nu\beta} = 0$

3. $\varepsilon_{123} = +\sqrt{\det(\perp)}$

4. (a) $\varepsilon_{\mu\nu\alpha} \varepsilon^{\beta\sigma\tau} = 3!\ \perp^{[\beta}{}_\mu \perp^\sigma{}_\nu \perp^{\tau]}{}_\alpha$

   (b) $\varepsilon_{\mu\nu\tau} \varepsilon^{\alpha\beta\tau} = 2!\ \perp^{[\alpha}{}_\mu \perp^{\beta]}{}_\nu$

   (c) $\varepsilon_{\mu\sigma\tau} \varepsilon^{\alpha\sigma\tau} = 2 \perp^\alpha{}_\mu$

   (d) $\varepsilon_{\alpha\sigma\tau} \varepsilon^{\alpha\sigma\tau} = 3!$

Secondly, we consider the Weyl Conformal tensor,

$$C_{\mu\nu\alpha\beta} = {}^{(4)}R_{\mu\nu\alpha\beta} - 2g_{[\mu\alpha}{}^{(4)}R_{\nu\beta]} + \frac{1}{3} g_{\mu[\alpha} g_{\beta]\nu}{}^{(4)}R \tag{3.25}$$

$$C_{\mu\nu\alpha\beta} = {}^{(4)}R_{\mu\nu\alpha\beta} - \kappa[2 g_{[\mu\alpha} T_{\nu\beta]} - g_{[\mu\alpha} g_{\nu\beta]} T + \frac{1}{3} g_{\mu[\alpha} g_{\beta]\nu} T] \tag{3.26}$$

From this definition we see that the Weyl tensor shares the same symmetries as the Riemann tensor (see, for example Misner et al. [1973]). In particular:

$$C_{\mu\nu\alpha\beta} = C_{[\mu\nu][\alpha\beta]} \tag{3.27}$$

$$C_{\mu\nu\alpha\beta} = C_{\alpha\beta\mu\nu} \tag{3.28}$$

$$C_{\mu[\nu\alpha\beta]} = C_{[\mu\nu\alpha\beta]} = 0 \tag{3.29}$$

The Weyl tensor has the additional constraint that it is trace-free, i.e.

$$C^{\alpha\beta}{}_{\alpha\beta} = 0 \tag{3.30}$$

It represents the ten trace-free components of the Riemann tensor in a 4-dimensional spacetime.

Most importantly for this work we can express the familiar Bianchi identities (again, see Misner et al. [1973]) in terms of the Weyl tensor. We do this by utilising the definition (3.25) which gives us the uncontracted and contracted Bianchi identities respectively:

$$\varepsilon^{\sigma\mu\nu}\nabla_\sigma C_{\mu\nu\alpha\beta} = 2\varepsilon_{\sigma\mu[\alpha}\nabla^\sigma R_{\beta]}{}^{\mu} + \frac{1}{3}\varepsilon_{\sigma\alpha\beta}\nabla^\sigma R \tag{3.31}$$

$$\nabla^\sigma C_{\mu\nu\alpha\sigma} = \nabla_{[\nu}R_{\mu]\alpha} + \frac{1}{6}g_{\alpha[\nu}\nabla_{\mu]}R \tag{3.32}$$

where the Ricci tensor and its trace are the four dimensional quantities.

To aid with the 3+1 decomposition of the Bianchi identities we can, with knowledge of the Weyl tensor and $\varepsilon_{\mu\nu\alpha\beta}$, define the electric and magnetic parts of the Weyl tensor as [Ellis, 1971]

$$E_{\mu\nu} := C_{\alpha\mu\beta\nu} n^{\alpha} n^{\beta} \tag{3.33}$$

$$\begin{aligned} B_{\mu\nu} &:= \frac{1}{2} \varepsilon_{\tau\mu\sigma\alpha} C^{\sigma\alpha}{}_{\beta\nu} n^{\tau} n^{\beta} \\ &= \frac{1}{2} \varepsilon_{\mu\sigma\alpha} C^{\sigma\alpha}{}_{\beta\nu} n^{\beta} \end{aligned} \tag{3.34}$$

These are both spatial ($E_{\mu\tau} n^{\tau} = B_{\mu\tau} n^{\tau} = 0$) and trace-free ($E^{\sigma}{}_{\sigma} = B^{\sigma}{}_{\sigma} = 0$).

Just as the Riemann tensor may be decomposed in the 3+1 formalism, so may the Weyl conformal tensor. The remainder of chapter will look at this decomposition, and its implications for numerical relativity, in considerable depth.

3.4.2 The Decomposition of the Weyl Tensor

As with any 4-dimensional tensor quantity we can break the Weyl tensor up into its components perpendicular and parallel to the hypersurface (Σ), according to the rule (2.7), yielding

$$\begin{aligned} C_{\mu\nu\alpha\beta} = {} & \perp C_{\mu\nu\alpha\beta} - (\perp C_{\tau\nu\alpha\beta} n^{\tau}) n_{\mu} - (\perp C_{\mu\tau\alpha\beta} n^{\tau}) n_{\nu} - (\perp C_{\mu\nu\tau\beta} n^{\tau}) n_{\alpha} \\ & - (\perp C_{\mu\nu\alpha\tau} n^{\tau}) n_{\beta} + (\perp C_{\tau\sigma\alpha\beta} n^{\tau} n^{\sigma}) n_{\mu} n_{\nu} + (\perp C_{\tau\nu\sigma\beta} n^{\tau} n^{\sigma}) n_{\mu} n_{\alpha} \\ & + (\perp C_{\tau\nu\alpha\sigma} n^{\tau} n^{\sigma}) n_{\mu} n_{\beta} + (\perp C_{\mu\tau\sigma\beta} n^{\tau} n^{\sigma}) n_{\nu} n_{\alpha} \\ & + (\perp C_{\mu\tau\alpha\sigma} n^{\tau} n^{\sigma}) n_{\nu} n_{\beta} + (\perp C_{\mu\nu\tau\sigma} n^{\tau} n^{\sigma}) n_{\alpha} n_{\beta} \end{aligned} \tag{3.35}$$

noting that $\perp$ projects all *free* indices only and that contracting the Weyl tensor with the normal more then twice equals zero, through symmetry.

From the previous equation we can obtain three equations that are analogous to the Gauss-Codazzi-Ricci equations ((2.21) - (2.23)). First we consider the double projection along the normal, $\perp C_{\mu\tau\alpha\sigma}n^\tau n^\sigma$. By using the definition of the electric conformal tensor (3.33) and the fact that it is spatial we obtain

$$\perp C_{\mu\tau\alpha\sigma}n^\tau n^\sigma = E_{\mu\alpha} \tag{3.36}$$

Considering the single projection along the normal,

$$\perp C_{\tau\nu\alpha\beta}n^\tau = \perp^\rho_\nu \perp^{[\gamma}_\alpha \perp^{\omega]}_\beta C_{\tau\rho|\gamma\omega|}n^\tau \tag{3.37}$$

leads to

$$\perp C_{\tau\nu\alpha\beta}n^\tau = \varepsilon_{\alpha\beta\sigma}B^\sigma{}_\nu \tag{3.38}$$

The full projection onto the hypersurface ($\perp C_{\mu\nu\alpha\beta} = \perp^{[\tau}_\mu \perp^{\sigma]}_\nu \perp^{[\gamma}_\alpha \perp^{\omega]}_\beta C_{[\tau\sigma][\gamma\omega]}$) yields

$$\perp C_{\mu\nu\alpha\beta} = -\varepsilon_{\mu\nu\pi}\varepsilon_{\alpha\beta\rho}E^{\rho\pi} \tag{3.39}$$

By substituting equations (3.36) - (3.39) into the decomposition of the Weyl tensor (3.35) we obtain an expression for the Weyl tensor in terms of its electric and magnetic parts:

$$
\begin{aligned}
C_{\mu\nu\alpha\beta} = &- \varepsilon_{\mu\nu\omega}\varepsilon_{\alpha\beta\rho}E^{\rho\omega} - \varepsilon_{\alpha\beta\sigma}B^{\sigma}{}_{\nu}n_{\mu} \\
&+ \varepsilon_{\alpha\beta\sigma}B^{\sigma}{}_{\mu}n_{\nu} - \varepsilon_{\mu\nu\sigma}B^{\sigma}{}_{\beta}n_{\alpha} + \varepsilon_{\mu\nu\sigma}B^{\sigma}{}_{\alpha}n_{\beta} \\
&+ E_{\mu\alpha}n_{\nu}n_{\beta} - E_{\nu\alpha}n_{\mu}n_{\beta} + E_{\nu\beta}n_{\mu}n_{\alpha} - E_{\mu\beta}n_{\nu}n_{\alpha} \qquad (3.40)
\end{aligned}
$$

Now that we have an expression for the Weyl tensor in terms of the gravito-electric and gravito-magnetic tensors we are in a position to consider the 3+1 decomposition of the Bianchi identities.

3.4.3 The Bianchi Identities

In this section we shall obtain the 3+1 Bianchi identities in terms of the gravito-electric and gravito-magnetic tensors. For this we will start with equations (3.31) and (3.32), the Bianchi identities. To obtain the gravitational analogue of the Maxwell equations we need to construct four independent, tensorial equations. By considering the decomposition of $C_{\mu\nu\alpha\beta}$, equation (3.35), we surmise that we can obtain only three independent equations from the once contracted identity so we must utilise both the uncontracted and once contracted Bianchi identities for our task.

We will get one tensorial equation from considering each of the following projections of the Bianchi identities:

$$\perp \nabla^{\sigma} C_{\mu\nu\alpha\sigma} = \perp \kappa \left(\nabla_{[\nu} T_{\mu]\alpha} + \frac{1}{3} g_{\alpha[\nu} \nabla_{\mu]} T \right) \tag{3.41}$$

$$\perp (\nabla^{\sigma} C_{\mu\tau\alpha\sigma}) n^{\tau} = \perp \kappa \left(\nabla_{[\tau} T_{\mu]\alpha} + \frac{1}{3} g_{\alpha[\tau} \nabla_{\mu]} T \right) n^{\tau} \tag{3.42}$$

$$\perp (\nabla^{\sigma} C_{\mu\tau\omega\sigma}) n^{\tau} n^{\omega} = \perp \kappa \left(\nabla_{[\tau} T_{\mu]\omega} + \frac{1}{3} g_{\omega[\tau} \nabla_{\mu]} T \right) n^{\tau} n^{\omega} \tag{3.43}$$

and

$$\perp \varepsilon^{\sigma\mu\nu} (\nabla_{\sigma} C_{\mu\nu\alpha\tau}) n^{\tau} = \perp \kappa \left(2 \varepsilon_{\sigma\mu[\alpha} \nabla^{\sigma} T_{\tau]}{}^{\mu} - \frac{1}{3} \varepsilon_{\sigma\alpha\tau} \nabla^{\sigma} T \right) n^{\tau} \tag{3.44}$$

where we have used the Einstein equations, (1.1), to replace the Ricci tensor in equations (3.31) and (3.32) with the mass-energy tensor, $T_{\mu\nu}$.

We shall sketch the outline of the derivation by considering the left-hand and right-hand sides of the above equations separately. We first consider the left hand side (i.e. the projection of the Weyl tensor) of equation (3.41). We replace the Weyl tensor with its definition in terms of the gravito-electric and gravito-magnetic tensors, via equation (3.40), and expand the derivative using the Leibniz rule, equation (2.15).

We also make use of the identity (2.20) to replace terms of the form $\nabla_\mu n_\nu$. We obtain

$$\begin{aligned}\perp C_{\mu\nu\alpha\tau} = {} & \perp_\mu{}^\tau \perp_\nu{}^\pi \perp_\alpha{}^\beta \, [-\nabla^\sigma(\varepsilon_{\tau\pi\omega}\varepsilon_{\beta\sigma\rho}E^{\rho\omega}) - \varepsilon_{\tau\pi\omega}B^{\omega}{}_\beta tr(K) \\ & + \varepsilon_{\tau\pi\omega}\,\dot{B}^{\omega}{}_\beta + B^{\omega}{}_\beta n_\sigma \nabla^\sigma(\varepsilon_{\tau\pi\omega\rho}n^\rho)] \\ & + 2\perp_\mu{}^{(\tau}\perp_\nu{}^{\pi)}\,(E_{\alpha\tau}\,\dot{n}_\pi - \varepsilon_{\sigma\omega\alpha}B^{\omega}{}_\tau K^{\sigma}{}_\pi) \\ & + \varepsilon_{\mu\nu\omega}B^{\omega\sigma}K_{\sigma\alpha}\end{aligned} \tag{3.45}$$

where the dot denotes the projection of the covariant 4-derivative in the direction of the normal, i.e. for an arbitrary rank-2 tensor $W_{\mu\nu}$,

$$\dot{W}_{\mu\nu} = n_\sigma \nabla^\sigma W_{\mu\nu} \tag{3.46}$$

We utilise the properties of the alternating pseudo-tensor (section 3.4.1, properties 1,2 and 4) and equation (3.22), to simplify this further. It follows from the definition of the the 3-covariant derivative (equation (2.13)) that the $\nabla^\sigma E^\rho{}_\omega$ in the above equation may be replaced with $D^\sigma E^\rho{}_\omega$. Thus equation (3.45) becomes

$$\begin{aligned}\perp \nabla^\sigma C_{\mu\nu\alpha\sigma} = {} & \varepsilon_{\mu\nu}{}^{\omega}[-\varepsilon_{\alpha\sigma\rho}D^\sigma E^\rho{}_\omega + 2\varepsilon_{\sigma\gamma(\alpha}E^\sigma{}_{\omega)}\,\dot{n}^\gamma \\ & - 2B_{\alpha\omega}tr(K) + \dot{B}_{\alpha\omega} - B_{\omega\gamma}\,\dot{n}^\gamma\, n_\alpha \\ & + 2B_{\sigma\omega}K^\sigma{}_\alpha + B_{\sigma\alpha}K^\sigma{}_\omega - \perp_{\alpha\omega}\, B^{\tau\sigma}K_{\tau\sigma}]\end{aligned} \tag{3.47}$$

Note we have also used the definition of the 3-covariant derivative, D_μ, in terms of the 4-covariant derivative (2.13) in order to express the above equation in terms of spatial quantities and operators only.

Using the definition of the Lie derivative (2.32) along with equation (2.20) we can identify

$$\overset{\bullet}{B}_{\alpha\omega} = \pounds_n B_{\alpha\omega} + B_{\sigma(\alpha}K^{\sigma}{}_{\omega)} + B_{\sigma(\alpha}n_{\omega)}\overset{\bullet}{n}{}^{\sigma} \tag{3.48}$$

In order to highlight the mathematical similarities between the 3+1 Bianchi identities and the microscopic Maxwell equations we make use of two important definitions, as given by Maartens [1997]. The spatial divergence of a vector and a rank-2 tensor are taken to be

$$\mathrm{div}V = D^{\alpha}V_{\alpha} \tag{3.49}$$

$$(\mathrm{div}M)_{\mu} = D^{\alpha}M_{\mu\alpha} \tag{3.50}$$

respectively. Similarly we use the following definition of the curl of a vector and tensor:

$$\mathrm{curl}(V_{\mu}) = \varepsilon_{\mu\alpha\beta}D^{\alpha}V^{\beta} \tag{3.51}$$

$$\mathrm{curl}(M_{\mu\nu}) = \varepsilon_{\alpha\beta(\mu}D^{\alpha}M_{\nu)}{}^{\beta} \tag{3.52}$$

The curl and divergence are related via [Maartens and Bassett, 1998]

$$\mathrm{curl}(M_{\mu\nu}) = \varepsilon_{\mu\sigma\rho}D^{\sigma}M^{\rho}{}_{\nu} - \frac{1}{2}\varepsilon_{\mu\nu\rho}(\mathrm{div}M)^{\rho} \tag{3.53}$$

These relations allow us to reduce equation (3.47) to

$$\begin{aligned}\perp \nabla^{\sigma} C_{\mu\nu\alpha\sigma} = & \varepsilon_{\mu\nu}{}^{\omega}[\pounds_n B_{\alpha\omega} - \mathrm{curl}(E_{\alpha\omega}) + 2\varepsilon_{\sigma\gamma(\alpha} E^{\sigma}{}_{\omega)} \overset{\bullet}{n}{}^{\gamma} \\ & - \frac{1}{2}\varepsilon_{\alpha\omega\rho} D_{\sigma} E^{\sigma\rho} - 2B_{\alpha\omega} tr(K) + 3B_{\sigma\omega} K^{\sigma}{}_{\alpha} \\ & + 2B_{\sigma\alpha} K^{\sigma}{}_{\omega} - \perp_{\alpha\omega} B_{\sigma\rho} K^{\sigma\rho}]\end{aligned} \tag{3.54}$$

Using the same techniques, we can express the left-hand side of equation (3.42) as

$$\begin{aligned}\perp (\nabla^{\sigma} C_{\mu\tau\alpha\sigma}) n^{\tau} = & -[\pounds_n E_{\alpha\mu} + \mathrm{curl}(B_{\alpha\mu}) + \frac{1}{2}\varepsilon_{\alpha\mu\omega} D_{\sigma} B^{\sigma\omega} \\ & - 2\varepsilon_{\sigma\omega(\alpha} B^{\sigma}_{\mu)} \overset{\bullet}{n}{}^{\omega} + 3E_{\sigma\mu} K^{\sigma}{}_{\alpha} + 2E_{\sigma\alpha} K^{\omega}{}_{\mu} \\ & - \perp_{\alpha\mu} E_{\sigma\omega} K^{\sigma\omega} - 2E_{\alpha\mu} tr(K)]\end{aligned} \tag{3.55}$$

The left-hand side of equation (3.43) is expanded using the Leibniz rule for derivatives, i.e.

$$\perp (\nabla^{\sigma} C_{\mu\nu\alpha\sigma}) n^{\mu} n^{\alpha} = \perp [\nabla^{\sigma}(C_{\mu\nu\alpha\sigma} n^{\mu} n^{\alpha}) - C_{\mu\nu\alpha\sigma} \nabla^{\sigma}(n^{\mu} n^{\alpha})] \tag{3.56}$$

We then take the above equation and expand out each term, again using the Leibniz rule. We utilise the definition of the gravito-electric tensor (3.33) the decomposition of $C_{\mu\nu\alpha\beta}$, equation (3.40), and equation (2.20), which relates the 4-derivative of the normal vector and the extrinsic curvature. This leads to the following expression

$$\perp (\nabla^{\sigma} C_{\mu\nu\alpha\sigma}) n^{\mu} n^{\alpha} = D^{\sigma} E_{\sigma\nu} + \varepsilon_{\mu\nu\omega} B^{\omega}{}_{\sigma} K^{\sigma\mu} \tag{3.57}$$

We expand equation (3.44) in the same way, taking note of the definition of the gravito-magnetic tensor, equation (3.34), to obtain

$$\perp \varepsilon^{\sigma\mu\nu}(\nabla_\sigma C_{\mu\nu\alpha\tau})n^\tau = -2D_\sigma B^\sigma{}_\alpha - 2\varepsilon_{\alpha\tau\gamma}E^{\gamma\omega}K_\omega{}^\tau \tag{3.58}$$

For each of the right-hand sides of the contracted Bianchi identities, (3.41) - (3.43), we substitute the 3+1 decomposition of $T_{\mu\nu}$ (equation (2.25)) and use the properties of $\varepsilon_{\mu\nu\alpha}$ to obtain

$$\perp \kappa\left(\nabla_{[\nu}T_{\mu]\alpha} + \frac{1}{3}g_{\alpha[\nu}\nabla_{\mu]}T\right) = \frac{\kappa}{2}\varepsilon_{\mu\nu}{}^\omega\left[\varepsilon_{\tau\rho\omega}(D^\rho\pi^\tau{}_\alpha - j^\tau K^\rho{}_\alpha) - \frac{1}{3}\varepsilon_{\tau\alpha\omega}D^\tau\rho\right] \tag{3.59}$$

$$\begin{aligned}\perp \kappa\left(\nabla_{[\tau}T_{\mu]\alpha} + \frac{1}{3}g_{\alpha[\tau}\nabla_{\mu]}T\right)n^\tau = \frac{\kappa}{2}[&\dot{\pi}_{\mu\alpha} - \pi_{\mu\sigma}\dot{n}^\sigma n_\alpha - \pi_{\tau\alpha}\dot{n}^\tau n_\mu \\ &+ 2j_{(\mu}\dot{n}_{\alpha)} - K_{\alpha\mu}\rho - \pi_{\sigma\alpha}K^\sigma{}_\mu - K_{\alpha\mu}P \\ &+ \frac{1}{3}\perp_{\alpha\mu}\dot{\rho} + D_\mu j_\alpha]\end{aligned} \tag{3.60}$$

$$\begin{aligned}\perp \kappa\left(\nabla_{[\tau}T_{\mu]\omega} + \frac{1}{3}g_{\omega[\tau}\nabla_{\mu]}T\right)n^\tau n^\omega = \frac{\kappa}{2}[&\frac{2}{3}D_\nu\rho - 2j_\sigma K^\sigma_\nu + \dot{j}_\nu - j_\sigma\dot{n}^\sigma n_\nu + \rho\,\dot{n}_\nu \\ &+ \pi_{\nu\sigma}\dot{n}^\sigma + \dot{n}_\nu P + D_\nu P]\end{aligned} \tag{3.61}$$

Similarly, the right-hand side of the uncontracted Bianchi identity yields

$$\perp \kappa\left(2\varepsilon_{\sigma\mu[\alpha}\nabla^\sigma T_{\tau]}{}^\mu - \frac{1}{3}\varepsilon_{\sigma\alpha\tau}\nabla^\sigma T\right)n^\tau = \kappa\varepsilon_{\sigma\omega\alpha}[\pi^\omega{}_\tau K^{\sigma\tau} - D^\sigma j^\omega] \tag{3.62}$$

We can use the definition of the curl of a tensor (3.51) to modify equation (3.59). We can also simplify equation (3.60) and equation (3.61) by considering the relationship between the Lie derivative and the $^\bullet$ operator. By definition of the Lie derivative and equation (2.20) we have

$$\overset{\bullet}{\rho} = \pounds_n \rho \tag{3.63}$$

$$\overset{\bullet}{j}_\mu = \pounds_n j_\mu - j_\sigma \nabla_\mu n^\sigma = \pounds_n j_\mu + j_\sigma (K_\mu{}^\sigma + n_\mu \overset{\bullet}{n}{}^\sigma) \tag{3.64}$$

$$\overset{\bullet}{\pi}_{\mu\nu} = \pounds_n \pi_{\mu\nu} - 2\pi_{\sigma(\mu} \nabla_{\nu)} n^\sigma = \pounds_n \pi_{\mu\nu} + 2\pi_{\sigma(\mu} K_{\nu)}{}^\sigma + 2\pi_{\sigma(\mu} n_{\nu)} \overset{\bullet}{n}{}^\sigma \tag{3.65}$$

The right hand sides of the uncontracted Bianchi identities may then be expressed as

$$\begin{aligned} \perp \kappa\left(\nabla_{[\nu} T_{\mu]\alpha} + \frac{1}{3} g_{\alpha[\nu} \nabla_{\mu]} T\right) &= -\frac{\kappa}{2} \varepsilon_{\mu\nu}{}^\omega [\mathrm{curl}(\pi_{\omega\alpha}) + \frac{1}{2} \varepsilon_{\omega\alpha\rho} D_\sigma \pi^{\sigma\rho} \\ &\quad + \varepsilon_{\tau\rho\omega} j^\tau K^\rho{}_\alpha + \frac{1}{3} \varepsilon_{\sigma\alpha\omega} D^\sigma \rho] \end{aligned} \tag{3.66}$$

$$\begin{aligned} \perp \kappa\left(\nabla_{[\tau} T_{\mu]\alpha} + \frac{1}{3} g_{\alpha[\tau} \nabla_{\mu]} T\right) n^\tau &= \frac{\kappa}{2} [\pounds_n \pi_{\mu\alpha} + \pi_{\sigma\mu} K^\sigma{}_\alpha + 2 j_{(\mu} \overset{\bullet}{n}_{\alpha)} - K_{\alpha\mu}(P + \rho) \\ &\quad + D_\mu j_\alpha + \frac{1}{3} \perp_{\alpha\mu} \pounds_n \rho] \end{aligned} \tag{3.67}$$

$$\begin{aligned} \perp \kappa\left(\nabla_{[\tau} T_{\mu]\omega} + \frac{1}{3} g_{\omega[\tau} \nabla_{\mu]} T\right) n^\tau n^\omega &= \frac{\kappa}{2} [\pounds_n j_\nu + \frac{2}{3} D_\nu \rho - j_\sigma K_\nu^\sigma + \rho \overset{\bullet}{n}_\nu \\ &\quad + \pi_{\cdot\sigma} \overset{\bullet}{n}{}^\sigma + \overset{\bullet}{n}_\nu P + D_\nu P] \end{aligned} \tag{3.68}$$

Equation (3.62) remains unchanged.

3.4.4 Conservation Equations

Before we combine our left-hand (equations 3.54) - (3.58)) and right-hand (equations (3.66) - (3.62)) sides, we choose to simplify the right-hand sides somewhat. You will note that equations (3.67) and (3.68) contain propagation terms (e.g. $\pounds_n j_\mu$). We can simplify the propagation terms involving the hydrodynamical quantities by considering the twice contracted Bianchi identities,

$$\nabla_\alpha T^\alpha{}_\nu = 0 \tag{3.69}$$

which give rise to the conservation equations.

We derive the continuity equation from projecting equation (3.69) in the direction of the normal vector, i.e. $n^\sigma \nabla_\alpha T^\alpha{}_\sigma = 0$ to obtain the following [York, 1979]

$$\pounds_n \rho = -D_\sigma j^\sigma + \pi^{\sigma\omega} K_{\sigma\omega} + (P+\rho)tr(K) - 2j_\sigma \overset{\bullet}{n}{}^\sigma \tag{3.70}$$

The generalised Euler equations are found from the projection of the twice-contracted Bianchi identities tangential to the hypersurface, $\perp^\beta{}_\sigma \; \nabla_\nu T^\nu{}_\beta = 0$. We obtain [York, 1979]

$$\pounds_n j_\mu = -D_\sigma \pi^\sigma{}_\mu - D_\mu P + j_\mu tr(K) - \pi_{\sigma\mu} \overset{\bullet}{n}{}^\sigma - (P+\rho)\overset{\bullet}{n}_\mu \tag{3.71}$$

Thus we see that we can obtain evolution equations for two of our hydrodynamical quantities, the energy density and energy flux, directly from the twice contracted Bianchi identities. In order to specify our isotropic and anisotropic pressures we need extra information for a given matter configuration, for example an equation of state. As we will be dealing only with vacuum spacetimes in this work, we will not go down the path of obtaining explicit equations for the pressure terms. In general, the question of finding an appropriate equation of state for relativistic fluids, such as in the interior of neutron stars, is non-trivial and deserves a thesis worth of explanation in itself. It was, however, worthwhile to consider the generalised continuity and Euler equations as we wish to present a prescription for 3+1+Bianchi identities that is applicable in general spacetimes.

3.4.5 The Gravitoelectromagnetic Equations

We substitute the continuity equation, (3.70), and Euler equation, (3.71), into equations (3.67) and (3.68). We are then in a position to combine equations (3.54)-(3.58) with equations (3.66)-(3.62) to obtain

$$D^{\sigma}(E_{\sigma\mu} + \frac{\kappa}{2}\pi_{\sigma\mu}) = \frac{\kappa}{3}D_{\mu}\rho - \varepsilon_{\sigma\mu\omega}(B^{\omega\tau} + \frac{\kappa}{2}\varepsilon^{\tau\omega\gamma}j_{\gamma})K^{\sigma}{}_{\tau} \tag{3.72}$$

$$D^{\sigma}(B_{\sigma\mu} + \frac{\kappa}{2}\varepsilon_{\sigma\mu\gamma}j^{\gamma}) = \varepsilon_{\sigma\mu\gamma}(E^{\gamma}{}_{\tau} + \frac{\kappa}{2}\pi^{\gamma}{}_{\tau})K^{\tau\sigma} \tag{3.73}$$

These constraint equations are used to simplify the remaining two equations, which become

$$\begin{aligned} &\pounds_n E_{\mu\nu} + \text{curl}(B_{\mu\nu}) - 2\varepsilon_{\sigma\omega(\mu}B^{\sigma}{}_{\nu)}\overset{\bullet}{n}{}^{\omega} + 5E_{\sigma(\mu}K_{\nu)}{}^{\sigma} - \perp_{\mu\nu} E_{\sigma\gamma}K^{\sigma\gamma} - 2E_{\mu\nu}tr(K) \\ &\quad = \frac{\kappa}{2}[\pi_{\sigma(\mu}K_{\nu)}{}^{\sigma} - \pounds_n\pi_{\mu\nu} - D_{(\mu}j_{\nu)} - 2j_{(\mu}\overset{\bullet}{n}_{\nu)} + (\rho + P)(K_{\mu\nu} - \frac{1}{3}\perp_{\mu\nu} tr(K)) \\ &\quad + \frac{1}{3}\perp_{\mu\nu}(D_{\sigma}j^{\sigma} - \pi_{\sigma\tau}K^{\sigma\tau} + 2j^{\sigma}\overset{\bullet}{n}_{\sigma})] \end{aligned} \tag{3.74}$$

$$\begin{aligned} &\pounds_n B_{\mu\nu} - \text{curl}(E_{\mu\nu} - \frac{\kappa}{2}\pi_{\mu\nu}) + 2\varepsilon_{\sigma\gamma(\mu}E^{\sigma}{}_{\nu)}\overset{\bullet}{n}{}^{\gamma} + 5B_{\sigma(\mu}K^{\sigma}_{\nu)} + \frac{\kappa}{2}\varepsilon_{\sigma\gamma(\mu}j^{\sigma}K^{\gamma}{}_{\nu)} \\ &\quad - 2B_{\mu\nu}tr(K) - \perp_{\mu\nu} B_{\sigma\gamma}K^{\sigma\gamma} = 0 \end{aligned} \tag{3.75}$$

It can be shown [Friedrich, 1996] that the equations above, when considered in vacuum, represent a symmetric hyperbolic system provided $\alpha > 0$ and $\perp_{\mu\nu}$ is positive definite. Friedrich proposed the addition of the gravito-'Maxwell' equation system, (3.72)-(3.75), to a hyperbolic formulation of the ADM equations, to form a complete hyperbolic evolution system. We have, instead, chosen to augment the Standard ADM equations with the gravito-'Maxwell' equations, in order to keep the resulting system relatively simple and to aid us in drawing comparisons with Standard ADM.

In understanding the above equations, we make use of the similarities between the above equations and the classical Maxwell equations, (3.2)-(3.4). Note in particular, that if we choose a perfect fluid equation of state, where $\pi_{\mu\nu} = j_\mu = 0$, the equations (3.72)-(3.75) reduce to the form

$$D^\sigma E_{\sigma\mu} + [\text{field coupling terms}] = \frac{\kappa}{3} D_\mu \rho \tag{3.76}$$

$$D^\sigma B_{\sigma\mu} + [\text{field coupling terms}] = 0 \tag{3.77}$$

$$\pounds_n E_{\mu\nu} + \text{curl}(B_{\mu\nu}) + [\text{field coupling terms}] = (P + \rho)(K_{\mu\nu} - \frac{1}{3} \perp_{\mu\nu} tr(K)) \tag{3.78}$$

$$\pounds_n B_{\mu\nu} + \text{curl}(E_{\mu\nu}) + [\text{field coupling terms}] = 0 \tag{3.79}$$

Firstly, note the additional field coupling terms that appear in the gravito-'Maxwell' equations, in comparison with the electromagnetic Maxwell equations. These arise for two reasons, namely the the tensor coupling of the gravito-electric and gravito-magnetic fields to the extrinsic curvature ($K_{\mu\nu}$ and $tr(K)$) and to the gauge functions ($\overset{\bullet}{n}^{\omega}$ terms).*

*Remember that $\overset{\bullet}{n}^{\omega} = D^\omega \ln(\alpha)$ by equation (2.5).

By simplifying to a perfect fluid, we are able to draw an analogy between source terms in classical electromagnetism and general relativity. By comparing equations (3.76) and (3.5) we can identify the gradient of the energy density, $D_\mu \rho$, as a gravito-electric charge density, in comparison with $\rho^{(em)}$ in electromagnetism. We see also that the general relativistic source term $(P+\rho)(K_{\mu\nu} - \frac{1}{3} \perp_{\mu\nu} tr(K))$ is analogous with the concept of charge density, $\mathbf{j}^{(em)}$ in the classical Maxwell equations. See Maartens and Bassett [1998] for a detailed discussion of these analogies in 1+3 formalism of Ellis.

3.4.6 Gravito-electromagnetic Potentials

The next step is to define gravito-potential terms, in analogy with the electromagnetism case. In classical electromagnetism the potentials are constructed from the Maxwell equations. In our case, however, we can define these more easily through the Codazzi and Ricci equations (2.22) and (2.23).

Firstly we substitute the definition of the Weyl tensor (3.26) into the Codazzi equation (2.22). We then use the 3+1 form of $T_{\mu\nu}$ (2.25) and equation (3.38) to obtain

$$B_{\mu\nu} = \varepsilon_{\sigma\tau\mu} D^{\sigma} K_{\nu}{}^{\tau} - \frac{\kappa}{2} \varepsilon_{\sigma\mu\nu} j^{\sigma} \tag{3.80}$$

Note that $B_{\mu\nu}$ is, by definition, trace-free. This implies that we should split the right hand side into its trace and trace-free parts in order to get a more 'natural' expression.

To facilitate this we express the extrinsic curvature as

$$K_{\mu\nu} = A_{\mu\nu} + \frac{1}{3} \perp_{\mu\nu} tr(K) \tag{3.81}$$

where $tr(K) = K^{\sigma}{}_{\sigma}$ and $tr(A) = 0$. The momentum constraint (2.29)) in this notation is

$$D_{\sigma}(A^{\sigma\mu} - \frac{2}{3} \perp^{\sigma\mu} K) = \kappa j^{\mu} \tag{3.82}$$

To simplify equation (3.80) we utilise equation (3.53), which relates the div and curl operators, and the trace-split version of the momentum constraint (3.82) to obtain the identity

$$\varepsilon_{\sigma\tau\mu} D^{\sigma} A_{\nu}{}^{\tau} = \mathrm{curl}(A_{\mu\nu}) + \frac{2}{3}\varepsilon_{\mu\nu\sigma} D^{\sigma} tr(K) + \frac{\kappa}{2}\varepsilon_{\mu\nu\sigma} j^{\sigma} \tag{3.83}$$

This identity and equation (3.81) reduce equation (3.80)

$$B_{\mu\nu} = \mathrm{curl} A_{\mu\nu} \tag{3.84}$$

which defines our tensor potential $A_{\mu\nu}$ (compare to the definition of the vector potential in electromagnetism, given by equation (3.6)).

We now use the Ricci equation (2.23) along with the Weyl tensor in terms of the 4-Riemann tensor and the mass-energy tensor (3.26), the 3+1 decomposition of $T_{\mu\nu}$

(2.25), and equation (3.39) to show that

$$
\begin{aligned}
&E_{\mu\nu} - \frac{1}{3}\perp_{\mu\nu}(A_{\sigma\tau} + \frac{1}{3}\perp_{\sigma\tau} tr(K))(A^{\sigma\tau} + \frac{1}{3}\perp^{\sigma\tau} tr(K)) \\
&+ \frac{1}{3}\perp_{\mu\nu} tr(\dot{K}) - \frac{1}{2}{}^{(3)}Q_{\mu\nu} + \frac{1}{2}A_{\mu\nu} tr(K) + \frac{1}{2}(\perp\dot{A}_{\mu\nu}) \\
&= \pounds_n tr(K) + (A_{\mu}{}^{\sigma} + \frac{1}{3}\perp_{\mu}{}^{\sigma} tr(K))(A_{\sigma\nu} + \frac{1}{3}\perp_{\sigma\nu} tr(K)) \\
&+ \frac{1}{2\alpha}(D_\mu D_\nu \alpha - \frac{1}{3}\perp_{\mu\nu} D_\sigma D^\sigma \alpha)
\end{aligned}
\tag{3.85}
$$

Using the definition of the Lie derivative, we can derive the following helpful identities

$$
\perp\dot{A}_{\mu\nu} = \pounds_n A_{\mu\nu} + 2A_{\mu\beta}A_{\nu}{}^{\beta} + \frac{2}{3}A_{\mu\nu}K \tag{3.86}
$$

$$
\pounds_n K_{\mu\nu} = \pounds_n A_{\mu\nu} - \frac{2}{3}A_{\mu\nu}K + \frac{1}{3}\perp_{\mu\nu}\dot{K} - \frac{1}{3}\perp_{\mu\nu} K^2 \tag{3.87}
$$

Equation (3.85) then reduces to

$$
\begin{aligned}
E_{\mu\nu} &= \frac{1}{2}[\pounds_n A_{\mu\nu} - \frac{1}{3}\perp_{\mu\nu}(\perp^{\alpha\beta}\pounds_n A_{\alpha\beta})] \\
&+ [D_\mu(D_\nu\alpha) - \frac{1}{3}\perp_{\mu\nu} D^\sigma(D_\sigma\alpha)] + {}^{(3)}Q_{\mu\nu} + \frac{1}{3}A_{\mu\nu}K
\end{aligned}
\tag{3.88}
$$

Note that $\pounds_n A_{\mu\nu} - \frac{1}{3}\perp_{\mu\nu}(\perp^{\alpha\beta}\pounds_n A_{\alpha\beta})$ is the trace-free part of $\pounds_n A_{\mu\nu}$. If we compare equation (3.85) with equation (3.7) we can identify the quantity $D_\mu\alpha$ as a vector potential, in analogy with the scalar potential, ϕ, in classical electromagnetism.

Furthermore, we can draw an analogy between gauge choices in general relativity and electromagnetism. The gravitational analog of the Coulomb gauge (3.16) in electromagnetism is $D^\sigma A_{\sigma\mu} = 0$. From the momentum constraint (3.81) we see that this is equivalent to the general relativistic gauge choice $tr(K)$ = constant. A widely used example of this family of gauge choices is maximal slicing, where

$$tr(K) = 0 \tag{3.89}$$

One of the most important points of the last few sections is that we can identify potentials with those in flat-space electromagnetism, just as we can identify the Weyl tensor with the electromagnetic tensor F_{ab}. In summary the key comparisons between quantities in electromagnetism and general relativity are

Electromagnetism	General Relativity
Field Tensors	
F_{ab}	$C_{\mu\nu\alpha\beta}$
Fields	
$E_a = F_{ab}n^b$	$E_{\alpha\beta} = C_{\alpha\tau\beta\rho}n^\tau n^\rho$
$B_a = \frac{1}{2}\varepsilon_{abc}F^{bc}$	$B_{\alpha\beta} = \frac{1}{2}\varepsilon_{\alpha\rho\sigma}C^{\rho\sigma}{}_{\beta\gamma}n^\gamma$
Potentials	
A_a	$A_{\mu\nu}$
ϕ	$D_\mu\alpha$
Source Terms	
$\mathbf{j}^{(em)}$	$(P+\rho)A_{\mu\nu}$
$\rho^{(em)}$	$D_\mu\rho$

3.5 The Modified 3+1 Equations

In chapter 2 we reviewed the 3+1 formalism for solving the Einstein equations. The preceding parts of this chapter have outlined the Bianchi identities in terms of the gravito-electric and gravito-magnetic tensors. We have seen how this allows us to make a direct analogy between general relativity and electromagnetism. We are now in a position to construct the numerical formalism.

The main modification to standard 3+1 formalism is made to the evolution equations for the extrinsic curvature, $K_{\mu\nu}$. Because the gravito-electric and gravito-magnetic tensors are by definition trace-free, we split up our standard evolution equations into trace and trace-free parts. By breaking up the evolution of the extrinsic curvature (2.44) we obtain

$$\begin{aligned} \pounds_n A_{\mu\nu} - \frac{1}{3} \perp_{\mu\nu} (\perp^{\sigma\tau} \pounds_n A_{\sigma\tau}) = {}^{(3)}Q_{\mu\nu} - 2(A_{\mu\sigma} A_\nu{}^\sigma - \frac{1}{3} \perp_{\mu\nu} A_{\sigma\tau} A^{\sigma\tau}) + \frac{1}{3} A_{\mu\nu} tr(K) \\ - \frac{1}{\alpha}(D_\mu D_\nu \alpha - \frac{1}{3} \perp_{\mu\nu} D^\sigma D_\sigma \alpha) - \kappa \pi_{\mu\nu} \end{aligned} \quad (3.90)$$

$$\pounds_n tr(K) = \frac{1}{3}(tr(K))^2 + A_{\sigma\tau} A^{\sigma\tau} - \frac{1}{\alpha} D_\sigma D^\sigma \alpha + \frac{\kappa}{2}(\rho + 3P) \quad (3.91)$$

where ${}^{(3)}Q_{\mu\nu} = {}^{(3)}R_{\mu\nu} - \frac{1}{3} \perp_{\mu\nu} {}^{(3)}R$ is the trace-free part of the 3-Ricci tensor.

We have also employed the Hamiltonian constraint (2.28) in the equation for the evolution of $tr(K)$, thereby removing the need to use the Ricci scalar explicitly in this equation. In fact, we can remove the Ricci tensor entirely from both the above equations, by utilising the definition of the gravito-electric tensor in terms of the tensor potential (3.88) to remove ${}^{(3)}Q_{\mu\nu}$ from equation (3.90). We are then left with

$$\begin{aligned} \pounds_n A_{\mu\nu} - \frac{1}{3} \perp_{\mu\nu} (\perp^{\sigma\tau} \pounds_n A_{\sigma\tau}) =& E_{\mu\nu} - (A_{\mu\sigma} A_\nu{}^\sigma - \frac{1}{3} \perp_{\mu\nu} A^{\sigma\tau} A_{\sigma\tau}) \\ & - \frac{1}{\alpha}(D_\mu D_\nu \alpha - \frac{1}{3} \perp_{\mu\nu} D^\sigma D_\sigma \alpha) - \frac{\kappa}{2}\pi_{\mu\nu} \end{aligned} \quad (3.92)$$

Additionally, if we substitute the Lie derivative of $A_{\mu\nu}$, from equation (3.90), into equation (3.92) we gain the following constraint equation relating the gravito-electric field, $E_{\mu\nu}$ and the trace-free part of the 3-Ricci tensor, ${}^{(3)}Q_{\mu\nu}$:

$$E_{\mu\nu} + \frac{\kappa}{2}\pi_{\mu\nu} = {}^{(3)}Q_{\mu\nu} - (A_{\mu\alpha} A_\nu{}^\alpha - \frac{1}{3} \perp_{\mu\nu} A_{\alpha\beta} A^{\alpha\beta}) + \frac{1}{3} A_{\mu\nu} tr(K) \quad (3.93)$$

Note that the gravito-electric tensor appears in the evolution equation for $A_{\mu\nu}$ (3.92). Thus we need to provide an evolution equation for $E_{\mu\nu}$ from our gravito-'Maxwell' equations (equation (3.74) to be precise). For this equation we need to know the gravito-magnetic tensor on each hypersurface. We have two choices here: we may either utilise the constraint equation (3.73) or the evolution equation (3.75)†. We choose to evolve $B_{\mu\nu}$. This avoids curl(curl($A_{\mu\nu}$)) terms, ensuring our system of equations is first order in both time and space.

The final form of the ADM + Gravitoelectromagnetism system is outlined below. The system involves the evolution of $\perp_{ij}$, A_{ij}, $tr(k)$, E_{ij} and B_{ij} subject to the constraint equations and the gauge variables α and β^μ.

†though we shall see in the next chapter that this choice is not so important for this work.

- Evolution Equations

$$(\partial_t - \pounds_\beta) \perp_{ij} = -2\alpha\{A_{ij} + \frac{1}{3} \perp_{ij} tr(K)\} \tag{3.94}$$

$$\begin{aligned}(\partial_t - \pounds_\beta)A_{ij} =& \alpha\{E_{ij} - \frac{1}{3} \perp_{ij} A_{ab}A^{ab} - A_{ia}A^a{}_j - \frac{\kappa}{2}\pi_{ij}\} \\ & - D_iD_j\alpha + \frac{1}{3} \perp_{ij} D_aD^a\alpha\end{aligned} \tag{3.95}$$

$$(\partial_t - \pounds_\beta)tr(K) = \alpha\{\frac{1}{3}tr(K)^2 + A_{ab}A^{ab} + \frac{\kappa}{2}(\rho + 3P)\} - D_aD^a\alpha \tag{3.96}$$

$$\begin{aligned}(\partial_t - \pounds_\beta)E_{ij} =& \alpha[-curlB_{ij} - 5E_{m(i}A_{j)}{}^m + \frac{1}{3}E_{ij}tr(K) \\ & + \perp_{ij} E_{mn}A^{mn} + \frac{\kappa}{2}(\pi_{m(i}A_{j)}{}^m + \frac{1}{3}\pi_{ij}tr(K) - \frac{1}{3} \perp_{ij} \pi_{mn}A^{mn} - \pounds_n\pi_{ij} \\ & - D_{(i}j_{j)} + \frac{1}{3} \perp_{ij} D_mj^m + (P + \rho)A_{ij})] \\ & + 2\varepsilon_{nm(i}B_{j)}{}^mD^n\alpha - \kappa(j_{(i}D_{j)}\alpha - \frac{1}{3} \perp_{ij} j^mD_m\alpha)\end{aligned} \tag{3.97}$$

$$\begin{aligned}(\partial_t - \pounds_\beta)B_{ij} =& \alpha[\mathrm{curl}(E_{ij} + \frac{\kappa}{2}\pi_{ij}) - 5B_{m(i}A_{j)}{}^m + \frac{1}{3}B_{ij}tr(K) \\ & + \perp_{ij} B_{mn}A^{mn} - \frac{\kappa}{2}\varepsilon_{mn(i}A_{j)}{}^mj^n] - 2\varepsilon_{mn(i}E_{j)}{}^mD^n\alpha\end{aligned} \tag{3.98}$$

plus the conservation equations (3.70) and (3.71) and a given equation of state.

- Constraints

$$2\kappa\rho = {}^{(3)}R + \frac{2}{3}tr(K)^2 - A_{mn}A^{mn} \tag{3.99}$$

$$\kappa j_i = D_m(A^m{}_i - \frac{2}{3} \perp^m{}_i tr(K) \tag{3.100}$$

$$B_{ij} = curl(A_{ij}) \tag{3.101}$$

$$E_{ij} + \frac{\kappa}{2}\pi_{ij} = {}^{(3)}Q_{ij} - (A_{ia}A_j{}^a - \frac{1}{3} \perp_{ij} A_{ab}A^{ab}) + \frac{1}{3}A_{ij}tr(K) \tag{3.102}$$

We have seen in this chapter that it is possible to augment the Standard ADM equations with the Bianchi identities, written in terms of the gravito-electro and gravito-magnetic conformal tensors. We will refer to this system of equations as the gravito-electromagnetic or GEM formalism. For the rest of this thesis we will be concerned with the numerical behaviour of the GEM formalism, particularly in comparison to the Standard ADM. Before this we shall take advantage of the symmetry of the numerical spacetimes under consideration in this work and reduce the GEM and ADM equations to the form used in the numerical simulations presented later.

Chapter 4

One-Dimensional Test Code Construction

In order to properly evaluate the usefulness of GEM for numerical relativity applications we shall spend the remainder of this work in the construction and application of an algorithm designed to compare the performance of our modified evolution equations with the Standard ADM equations as presented in chapter 2.

It is important when undertaking this kind of comparison, to make the workings of the test code as transparent as possible, assuring the reader that the performance we present is "real" and to allow better understanding of where different aspects of the performance are coming from. Thus, in this chapter we shall discuss the specific form of the equations that we use in this work and the development of the testing algorithm. On the former point, we will be restricting ourselves to one-dimensional, vacuum spacetimes for the rest of this work. Although a great deal of current research is focused on the solution of general three-dimensional spacetimes, the study of one dimensional test cases will still provide us with insight into the stability properties of a given numerical formalism.

4.1 The One-Dimensional Equations

Because we limit the range of spacetimes considered in this work we can simplify our equations somewhat. For clarity we shall lay out the GEM equations (and Standard ADM equations for comparison) as they are to be used in this work. We shall do this in general and note that any changes specific to a given test will be outlined in the appropriate section. We assume general coordinates (t, x^i) and the standard 3+1 line element:

$$ds^2 = -(\alpha^2 - \beta_m\beta^m)dt^2 + 2\beta_i dx^i dt + \perp_{ij} dx^i dx^j \tag{4.1}$$

or, alternatively, we can express the 4-metric components via

$$g_{\mu\nu} = \begin{bmatrix} -(\alpha^2 - \beta_m\beta^m) & \beta_1 & \beta_2 & \beta_3 \\ \beta^1 & & & \\ \beta^2 & & [\perp_{ij}] & \\ \beta^3 & & & \end{bmatrix}$$

As we are dealing with one-dimensional spacetimes, the 3-metric is diagonal for all the cases we consider here. Similarly, the only non-zero component of the shift vector will be β^1. Furthermore, in all cases we have $\perp_{22} \equiv \perp_{33}$, so our metric has only two independent components, which we shall denote as $\perp_1$ and $\perp_2$*. Thus our 3-metric takes the form

$$\perp_{ij} = \mathrm{diag}(\perp_1, \perp_2, \perp_2) \tag{4.2}$$

This also means that we are only left with the following non-zero connection functions. †

$$^{(3)}\Gamma^1{}_{11} = \frac{1}{2}\left(\frac{1}{\perp_1}\frac{\partial \perp_1}{\partial x^1}\right) \tag{4.3}$$

$$^{(3)}\Gamma^1{}_{22} = {}^{(3)}\Gamma^1{}_{33} = -\frac{1}{2}\left(\frac{1}{\perp_1}\frac{\partial \perp_2}{\partial x^1}\right) \tag{4.4}$$

$$^{(3)}\Gamma^2{}_{12} = {}^{(3)}\Gamma^3{}_{13} = -\frac{1}{2}\left(\frac{1}{\perp_2}\frac{\partial \perp_2}{\partial x^1}\right) \tag{4.5}$$

and Ricci tensor components:

$$^{(3)}R_{11} = -\frac{1}{2}\,\frac{-\left(\frac{\partial \perp_2}{\partial x^1}\right)^2 \perp_1 + 2\left(\frac{\partial^2 \perp_2}{(\partial x^1)^2}\right)\perp_2\perp_1 - \left(\frac{\partial \perp_1}{\partial x^1}\right)\left(\frac{\partial \perp_2}{\partial x^1}\right)\perp_2}{(\perp_2)^2\perp_1} \tag{4.6}$$

$$^{(3)}R_{22} = -\frac{1}{4}\,\frac{-\left(\frac{\partial \perp_1}{\partial x^1}\right)\frac{\partial \perp_2}{\partial x^1} + 2\left(\frac{\partial^2 \perp_2}{(\partial x^1)^2}\right)\perp_1 - 2\,(\perp_1)^2}{(\perp_1)^2} \tag{4.7}$$

$$^{(3)}R = -\frac{1}{2}\,\frac{-2\left(\frac{\partial \perp_{11}}{\partial x^1}\right)\left(\frac{\partial \perp_{22}}{\partial x^1}\right)\perp_{22} - \left(\frac{\partial \perp_{22}}{\partial x^1}\right)^2\perp_{11} - 2\perp_{22}(\perp_{11})^2 + 4\left(\frac{\partial^2 \perp_{22}}{(\partial x^1)^2}\right)\perp_{22}\perp_{11}}{(\perp_{22})^2(\perp_{11})^2} \tag{4.8}$$

As one of our spacetimes is best modelled using a conformal factor we will set up our

*Note that in the case of spherical symmetry, we have $\perp_{ij} = diag(\perp_{11}, \perp_{22}, \perp_{22}\sin\theta)$. By setting up our finite difference nodes along the line $\theta = \frac{\pi}{2}$ we obtain $\perp_{22} = \perp_{33}$.

†Again, in the case of spherical symmetry, we calculate the connections and then let $\theta = \frac{\pi}{2}$ to simplify.

general equations to allow for this. That is

$$\perp_{ij} = \Psi^4 \tilde{\perp}_{ij} = \Psi^4 diag(\tilde{\perp}_{11}, \tilde{\perp}_{22}, \tilde{\perp}_{33})$$
$$= \Psi^4 diag(\tilde{\perp}_1, \tilde{\perp}_2, \tilde{\perp}_2) \tag{4.9}$$

where Ψ is a function of x^1 only (see Chapter 6). The symmetry of the spacetimes considered allows us to define the complete one-dimensional evolution variables for each scheme as:

<u>GEM</u>

$$\mathcal{U}^{(\mathrm{gem})} = (\tilde{\perp}_1, \tilde{\perp}_2, \tilde{A}_1, \tilde{A}_2, tr(K), E_1, E_2, \alpha, \beta^1)$$

<u>Standard ADM</u>

$$\mathcal{U}^{(\mathrm{adm})} = (\tilde{\perp}_1, \tilde{\perp}_2, \tilde{K}_1, \tilde{K}_2, {}^{(3)}R_1, {}^{(3)}R_2, \alpha, \beta^1)$$

where each of the variables is a function of (t, x^1) only, and where‡

$$K_{ij} = \Psi^4 diag(\tilde{K}_1, \tilde{K}_2, \tilde{K}_2) \tag{4.10}$$

$$A_{ij} = \Psi^4(\tilde{K}_{ij} - \frac{1}{3}\tilde{\perp}_{ij} tr(K)) = \Psi^4 diag(\tilde{A}_1, \tilde{A}_2, \tilde{A}_2) \tag{4.11}$$

$$E_{ij} = diag(E_1, E_2, E_2) \tag{4.12}$$

$${}^{(3)}R_{ij} = diag({}^{(3)}R_1, {}^{(3)}R_2, {}^{(3)}R_2) \tag{4.13}$$

$${}^{(3)}Q_{ij} = {}^{(3)}R_{ij} - \frac{1}{3}\Psi^4 \tilde{\perp}_{ij} {}^{(3)}R = diag({}^{(3)}Q_1, {}^{(3)}Q_2, {}^{(3)}Q_2) \tag{4.14}$$

$$\beta^i = \beta^1 \tag{4.15}$$

Note that the electric conformal tensor, E_{ij}, is unchanged under conformal transfor-

‡Note that for the remainder of this work, E_1 and E_2 denote components of the gravito-electric tensor, *not* the electric field.

mations of the 3-metric.

One obvious thing to note here is that B_{ij} is not included in the one-dimensional evolution scheme. This is because B_{ij} is identically equal to zero for all the cases considered here. To prove this we consider the definition of the gravito-magnetic tensor

$$\begin{aligned} B_{ij} &= curl A_{ij} = \varepsilon_{ab(i} D^a A_{j)}{}^b \\ &= \frac{1}{2}[\perp_{im} \varepsilon^{abm} D_a A_{jb} + \perp_{jn} \varepsilon^{abn} D_a A_{ib}] \\ &= \frac{1}{2}\varepsilon^{abm}[\perp_{im} (\partial_a A_{jb} - {}^{(3)}\Gamma^n{}_{ja} A_{nb}) + \perp_{jm} (\partial_a A_{ib} - {}^{(3)}\Gamma^n{}_{ia} A_{nb})] \end{aligned} \tag{4.16}$$

By using the fact that metric and extrinsic curvature are functions of t and x^1 only and by substituting the form of the evolution variables given by (4.9) and (4.10)-(4.14) into the above definition (4.16), we can show that each component of B_{ij} is identically equal to zero. This result holds in spherical symmetry or any spacetime where we can reduce the metric to the form $\perp_{22}=\perp_{33}$. Early code tests evolved the gravito-magnetic tensor to check this constraint and it was found to be satisfied to machine precision. There is no reason, therefore, to include it in one-dimensional tests. It would be interesting, however, to investigate its influence in higher dimensional spacetimes. That is, however, beyond the scope of this work.

The evolution equations as they will be applied in this work are, therefore, given by:

GEM Evolution Equations

$$\partial_t \tilde{\mathrm{I}}_1 = \beta^1 \partial_1 \tilde{\mathrm{I}}_1 - 2\alpha\left(\tilde{A}_1 + \frac{1}{3}\tilde{\mathrm{I}}_1 tr(K)\right) + 4\beta^1 \tilde{\mathrm{I}}_1 \frac{\partial_1 \Psi}{\Psi} + 2\tilde{\mathrm{I}}_1 \partial_1 \beta^1 \tag{4.17}$$

$$\partial_t \tilde{\mathrm{I}}_2 = \beta^1 \partial_1 \tilde{\mathrm{I}}_2 - 2\alpha\left(\tilde{A}_2 + \frac{1}{3}\tilde{\mathrm{I}}_2 tr(K)\right) + 4\beta^1 \tilde{\mathrm{I}}_2 \frac{\partial_1 \Psi}{\Psi} \tag{4.18}$$

$$\begin{aligned}\partial_t \tilde{A}_1 = \beta^1 \partial_1 \tilde{A}_1 &+ \alpha\left(\Psi^{-4} E_1 - \frac{2}{3}\frac{\tilde{\mathrm{I}}_1 (A_2)^2}{(\tilde{\mathrm{I}}_2)^2} - \frac{4}{3}\frac{(\tilde{A}_1)^2}{\tilde{\mathrm{I}}_1}\right) \\ &- \Psi^{-4} D_1 D_1 \alpha + \frac{1}{3}\tilde{\mathrm{I}}_1 D_a D^a \alpha + 4\beta^1 \tilde{A}_1 \frac{\partial_1 \Psi}{\Psi} + 2\tilde{A}_1 \partial_1 \beta^1\end{aligned} \tag{4.19}$$

$$\begin{aligned}\partial_t \tilde{A}_2 = \beta^1 \partial_1 \tilde{A}_2 &+ \alpha\left(\Psi^{-4} E_2 - \frac{1}{3}\frac{\tilde{\mathrm{I}}_2 (A_1)^2}{(\tilde{\mathrm{I}}_1)^2} - \frac{5}{3}\frac{(\tilde{A}_2)^2}{\tilde{\mathrm{I}}_2}\right) \\ &- \Psi^{-4} D_2 D_2 \alpha + \frac{1}{3}\tilde{\mathrm{I}}_2 D_a D^a \alpha + 4\beta^1 \tilde{A}_2 \frac{\partial_1 \Psi}{\Psi}\end{aligned} \tag{4.20}$$

$$\partial_t tr(K) = \beta^1 \partial_1 tr(K) + \alpha\left(-\frac{1}{3}tr(K)^2 + \frac{(\tilde{A}_1)^2}{(\tilde{\mathrm{I}}_1)^2} + \frac{2(\tilde{A}_2)^2}{(\tilde{\mathrm{I}}_2)^2}\right) - D_a D^a \alpha \tag{4.21}$$

$$\partial_t E_1 = \beta^1 \partial_1 E_1 + \alpha\left(\frac{1}{3}E_1 tr(K) + \frac{2\tilde{\mathrm{I}}_1 E_2 \tilde{A}_2}{(\tilde{\mathrm{I}}_2)^2} - \frac{4E_1 \tilde{A}_1}{\tilde{\mathrm{I}}_1}\right) + 2E_1 \partial_1 \beta^1 \tag{4.22}$$

$$\partial_t E_2 = \beta^1 \partial_1 E_2 + \alpha\left(\frac{1}{3}E_2 tr(K) + \frac{\tilde{\mathrm{I}}_2 E_1 \tilde{A}_1}{(\tilde{\mathrm{I}}_1)^2} - \frac{3E_2 \tilde{A}_2}{\tilde{\mathrm{I}}_2}\right) \tag{4.23}$$

where

$$D_1 D_1 \alpha = (\partial_1)^2 \alpha - \frac{1}{2}\left(\frac{1}{\tilde{I}_1}(\partial_1 \tilde{I}_1) + \frac{4}{\Psi}\partial_1 \Psi\right)\partial_1 \alpha \tag{4.24}$$

$$D_2 D_2 \alpha = \frac{1}{2}\left(\frac{1}{\tilde{I}_1}\partial_1 \tilde{I}_2 + \frac{4\tilde{I}_2}{\tilde{I}_1 \Psi}\partial_1 \Psi\right)\partial_1 \alpha \tag{4.25}$$

$$D_a D^a \alpha = \frac{1}{\Psi^4}\left(\frac{D_1 D_1 \alpha}{\tilde{I}_1} + \frac{2 D_2 D_2 \alpha}{\tilde{I}_2}\right) \tag{4.26}$$

For comparison, we include the Standard ADM equations as they will be implemented in our benchmark code:

Standard ADM Evolution Equations

$$\partial_t \tilde{I}_1 = \beta^1 \partial_1 \tilde{I}_1 - 2\alpha \tilde{K}_1 + 4\beta^1 \tilde{I}_1 \frac{\partial_1 \Psi}{\Psi} + 2\tilde{I}_1 \partial_1 \beta^1 \tag{4.27}$$

$$\partial_t \tilde{I}_2 = \beta^1 \partial_1 \tilde{I}_2 - 2\alpha \tilde{K}_2 + 4\beta^1 \tilde{I}_2 \frac{\partial_1 \Psi}{\Psi} \tag{4.28}$$

$$\begin{aligned}\partial_t \tilde{K}_1 = {} & \beta^1 \partial_1 \tilde{K}_1 + \alpha\left(\Psi^{-4}({}^{(3)}R_1) - \frac{(\tilde{K}_1)^2}{(\tilde{I}_1)} + \frac{2\tilde{K}_2 \tilde{K}_1}{\tilde{I}_2}\right) \\ & - \Psi^{-4} D_1 D_1 \alpha + 4\beta^1 \tilde{K}_1 \frac{\partial_1 \Psi}{\Psi} + 2\tilde{K}_1 \partial_1 \beta^1\end{aligned} \tag{4.29}$$

$$\begin{aligned}\partial_t \tilde{K}_2 = {} & \beta^1 \partial_1 \tilde{K}_2 + \alpha\left(\Psi^{-4}({}^{(3)}R_2) + \frac{\tilde{K}_2 \tilde{K}_1}{\tilde{I}_1}\right) \\ & - \Psi^{-4} D_2 D_2 \alpha + 4\beta^1 \tilde{K}_2 \frac{\partial_1 \Psi}{\Psi}\end{aligned} \tag{4.30}$$

where the derivatives of the lapse function are as in (4.24) - (4.26).

4.2 Coding Choices

As well as outlining the form of the equations used, we must comment on the general choices of numerical techniques used to integrate the above equations. We do not consider the wide range of cutting edge numerical techniques under development, such as fixed and adaptive mesh refinement and black hole excision techniques (for example see Alcubierre and Brügmann [2001]). As we are trying to ascertain some of the properties of the above equations, and not necessarily chasing long-term evolutions, we use simple and transparent numerical techniques where possible.

The initial conditions are constructed on a one-dimensional, Eulerian grid. For the GEM system, $\mathcal{U}^{(gem)}$, we evolve all the variables, except the gauge variables, α and β^1, according to equations (4.17)-(4.23) using a numerical integrator. For the Standard ADM system, $\mathcal{U}^{(adm)}$, we evolve all the variables except the gauge variables, α and β^1, and the 3-Ricci tensor components, R_1 and R_2, according to equations (4.27)-(4.30). The 3-Ricci tensor is found by equations (4.6)-(4.8) at each iteration of the time-stepping algorithm. The methods used to calculate the gauge variables will be outlined separately for each simulation.

To guard against confusing the numerical effects with physical results we have carried out each of the simulations with two different forms of time integrator. We use an iterated Crank-Nicholson (CrN(2)) algorithm, with two iterations [Teukolsky, 2000]. This method is second-order accurate in time. It is considered to be a standard integrator within numerical relativity. There has been some concern that it can exhibit dissipation [Bona et al., 2003]. There was no evidence of this when we checked the

Crank-Nicholson results against our second choice of integrator, a fourth-order in time Runge-Kutta algorithm (RK4) [Press et al., 1996]. The Runge-Kutta integrator is a widely regarded as a robust integrator for both ordinary and partial differential equations, though it is relatively inefficient and for this reason is not often used for 3-D, large-scale simulations in general relativity.

For the most part we use centred, second order derivatives for the spatial derivatives, i.e., for some variable $u(x^1)$ defined at node i by the discrete value u_i

$$\frac{\partial u}{\partial x^1} = \frac{u_{i+1} - u_{i-1}}{2\Delta x^1} + O(\Delta x^1)^2 \tag{4.31}$$

$$\frac{\partial^2 u}{(\partial x^1)^2} = \frac{u_{i+1} - 2u_i + u_{i-1}}{(\Delta x^1)^2} + O(\Delta x^1)^2 \tag{4.32}$$

The only exception is outlined in chapter 7 where the inclusion of a shift vector leads to advection-type terms in the equations that are dealt with using upwind derivatives.

We are now in a position to study the behaviour of the GEM system of equations when applied to a series of simple testbed spacetime simulations.

Chapter 5

Slicings of Minkowski Spacetime

5.1 Finding 'Simple' Test Cases in G.R.

It is only fairly recently (within the last ten years) that the focus of research in numerical relativity has shifted to the question of stability. Therefore, it is only recently that code tests in numerical relativity have been designed to highlight stability features (along with standard accuracy and convergence testing).

In this chapter we consider various slicings of the simplest spacetime, Minkowski spacetime. The Minkowski line-element is given in cartesian coordinates ($[t, x, y, z]$) as

$$ds^2 = -dt^2 + dx^2 + dy^2 + dz^2 \tag{5.1}$$

and in spherical polars ($[t, r, \theta, \phi]$) as

$$ds^2 = -dt^2 + dr^2 + r^2 d\theta^2 + r^2 \sin^2(\theta) d\phi^2 \tag{5.2}$$

As these metrics represent simple four-dimensional flat spacetime, we may be led to the assumption that the numerical evolution of Minkowski space would be trivial. However, this is not necessarily the case. In fact, for nontrivial slicings and coordinate choices the Minkowski spacetime can exhibit coordinate singularities [Bernstein, 1993]. We shall investigate this idea here, with a view to evaluating the GEM algorithm's response to non-trivial coordinate and gauge dynamics.

5.2 Minkowski + Noise Numerical Tests

One of the simplest comparisons between the GEM and Standard ADM algorithms is constructed by supplying initial data from a Minkowski spacetime, plus small amplitude . andom noise, simulating small deviations from exact initial conditions. This tests the growth of unstable modes in both systems and are set up according to Alcubierre et al. [2003a], although we use spherically symmetric coordinates and a one-dimensional, not three-dimensional simulation. The test is designed to highlight the kind of gauge mode instabilities outlined in section 2.4.

We have the freedom to choose our gauge, through the freely specifiable lapse and shift functions. We choose zero shift vector and define the lapse using the harmonic slicing condition, as outlined below. Harmonic slicing is one of the Bona-Masso family of slicing conditions [Bona et al., 1995], given by the general formula:

$$\partial_t\alpha = -\alpha^2 f(\alpha)tr(K) \tag{5.3}$$

where $f(\alpha)$ is an arbitrary function. Harmonic slicing corresponds to the case $f(\alpha) = 1$, whereas the "1+ln" slicing is occurs when $f(\alpha) = 1/\alpha$ (see section 6.5).

By considering the evolution of the 3-metric (2.46) we can see that, with zero lapse,

$$\partial_t(det(\perp)^{1/2}) = -(det(\perp))^{1/2}(\alpha tr(K)) \tag{5.4}$$

Using this we can integrate (5.3) to obtain

$$\alpha = N(t,x^i)\sqrt{\det(\perp)} \tag{5.5}$$

where $N(t,x^i)$ is an arbitrary function of (t,x^i), usually chosen to be time-independent for simplicity of use and understanding. To implement (5.5) we shall make the common simplifying choice $N(t,x^i) = 1$.

These slicing conditions have been a source of interest in numerical relativity over a number of years. They have been widely used in the development of hyperbolic numerical relativity formalisms. Their attraction lies in the fact that the specification of the gauge according to equation (5.3) allows the reduction of the Einstein equations to a hyperbolic system [Reula, 1998].

Our motivation is slightly different. Using harmonic slicing allows our coordinate system to "respond" to changes in the spacetime, as opposed to a non-dynamic choice such as geodesic or maximal slicing (see chapter 6). By choosing a dynamic lapse we allow numerical noise to be propagated through space and possibly, depending on boundary conditions, off the grid. This has the potential to avoid the kind of coordinate 'focusing' singularities discussed in Bernstein [1993]. Although the Bona-Masso slicing conditions are better suited to the problems discussed in this chapter, they are not impervious to coordinate shock formation. For example see Alcubierre [1997] for a study of the behaviour of hyperbolic formalisms when coupled to these slicing conditions.

To set the initial conditions, the line element given in (5.2) was modified by adding small amplitude random noise (ϵ_{ij}) to $\perp_1$ and $\perp_2$. The random noise was calculated using a standard subroutine "ran2" given by Press et al. [1996]. The spherically symmetric grid was centred on r=10. This meant that the co-ordinate singularity at r=0 is avoided. Unfortunately it also meant that we were unable to use periodic boundary conditions, which are the most practical way of avoiding errors due to boundary noise. Instead we used a simple, static boundary value choice, where one ghost-point was initialised on either side of the grid on the initial slice, and this value was kept constant throughout the simulation. It was found that this "rough-and ready" boundary condition did not cause unacceptable errors and the boundary did not affect the dynamics on the inner grid unduly.

The grid and time stepping choices used were : $r \in (9.5, 10.5)$, $dr = 1/(50\rho)$ (no. of grid points = 50ρ), and $dt = 0.01\rho$, where $\rho = 1, 2, 4, 8$ is a scaling parameter. The purpose of this is allow us to increase grid resolution (to test convergence of errors) while keeping the ratio dt/dx constant ($dt/dx = 0.5$ in this case). This means that any errors that respond to the resolution are errors arising from gauge modes, not Courant instabilities.

The amplitude of the noise was chosen to vary within the range

$$\epsilon_{ij} \in [-10^{-10}/\rho^2, +10^{-10}/\rho^2] \tag{5.6}$$

to keep the perturbation within the linear regime, at least at first. The evolution variables were initialised as follows:

- $\Psi = 1$, i.e. not a conformal metric
- $\perp_1 = 1 + \epsilon_1$, $\perp_2 = r^2 + \epsilon_2$
- $K_1 = K_2 = A_1 = A_2 = tr(K) = 0$, i.e. a time-symmetric initial slice.
- Ricci Tensor terms calculated from the 3-metric using (4.6) to (4.8)
- $E_1 = {}^{(3)}Q_1$, $E_2 = {}^{(3)}Q_2$, using the constraint equation (3.93)
- $\alpha = 1$, $\beta = 0$

To compare the two schemes and track the growth of errors, we consider a few key variables. Consider a function W, defined at the discrete nodes $i = 0 \to nx$ by the values W_i. The L_2 norm of W is

$$L_2 W = \sqrt{\Sigma_{i=0}^{i=nx}(W_i)^2} \tag{5.7}$$

The L_∞ norm is just the maximum value of W_i on the grid. We track the L_2 and L_∞ of the Hamiltonian (H) and momentum (M^1) constraints as well as key kinematic quantities, such as $tr(K)$ and α. To track the growth of these errors, we output the constraint information at each light crossing time, which is simply the time it takes information travelling along a null geodesic to travel the length of the grid. Thus, for a given metric we have

$$\Delta t^2 = (g_{rr}\Delta r^2 + g_{\theta\theta}\Delta\theta^2 + g_{\phi\phi}\Delta\phi^2)/g_{tt} \tag{5.8}$$

and $\Delta\theta = \Delta\phi = 0$ for radially travelling information in our 1-dimensional spacetime and $\Delta r = 1$ is the length of the grid

Figures 5.1 and 5.2 show us the evolution of the L_2 norm of the Hamiltonian and momentum constraints respectively. Here we have used the second order iterative Crank-Nicholson time-stepping routine (CrN(2)). The GEM case clearly shows a growth of the initial errors in the constraints. The Standard ADM case shows a decay of the errors. This is not what is seen in similar three-dimensional simulations (for example Alcubierre et al. [2003a]) which clearly demonstrate that the Standard ADM equations exhibit exponential growth of these errors.

We also see that the deviation of our perturbed spacetime from Minkowski (figure 5.3) is essentially constant for Standard ADM and grows with time for GEM. Also note that the violation of the constraints and the magnitude of the errors in the evolution variables increases with increasing resolution in both cases, as is expected for pure gauge phenomena.

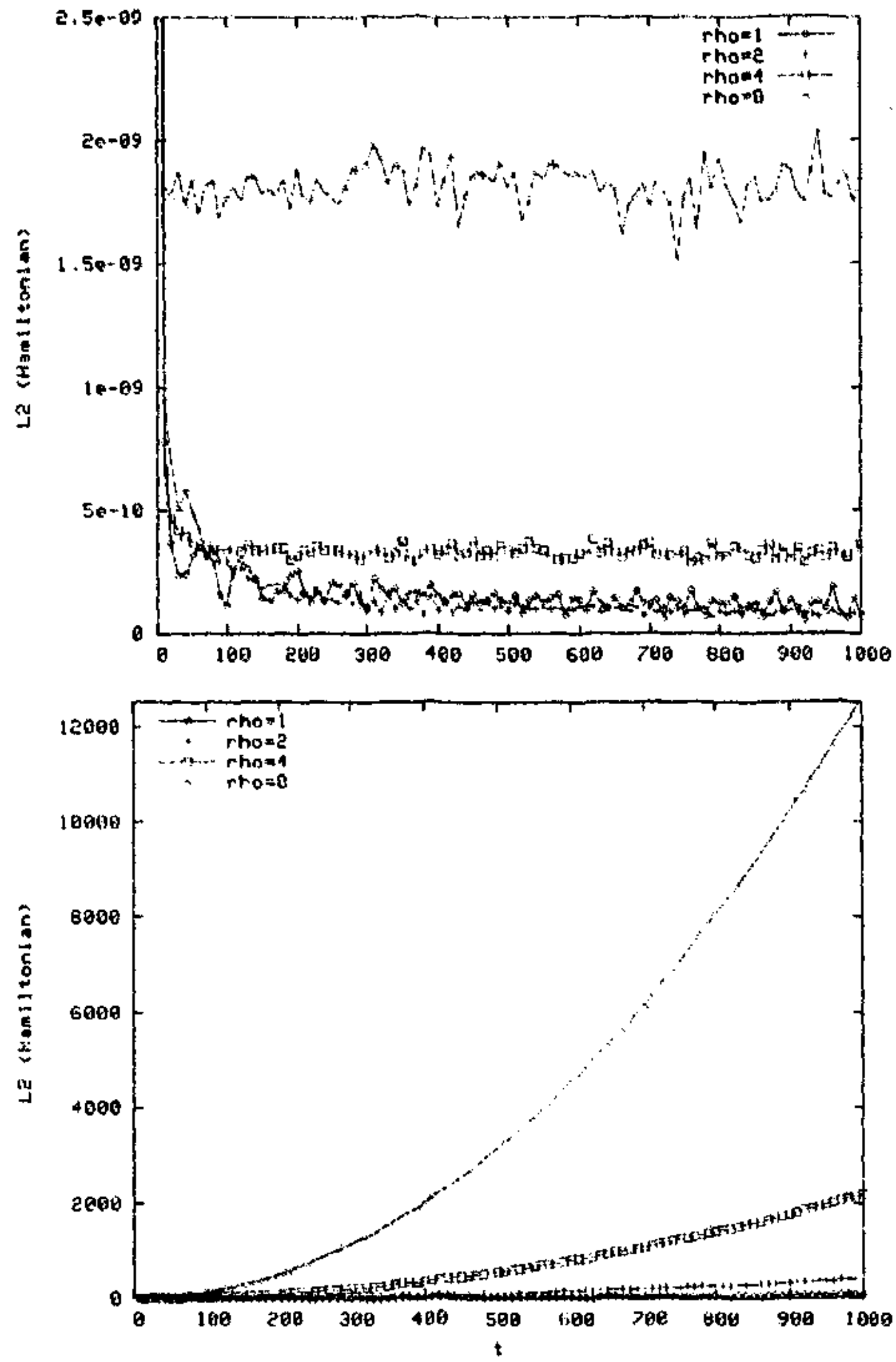

Figure 5.1: *The L_2 norm of the Hamiltonian constraint for the Standard ADM (top) and GEM (bottom) formalisms as a function of crossing time, t, for the Minkowski+noise spacetime using CrN(2) integration.*

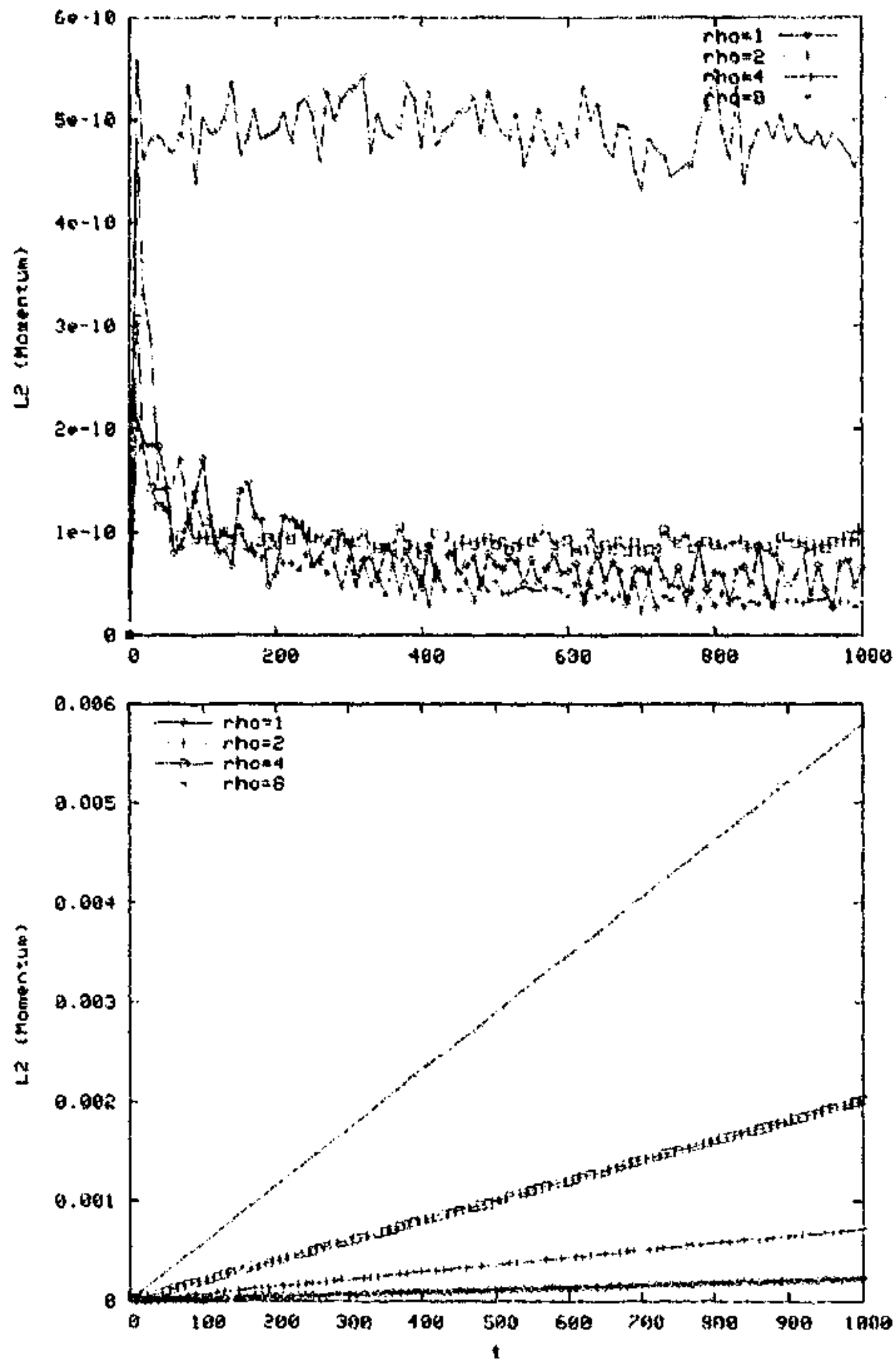

Figure 5.2: *The L_2 norm of the Momentum constraint for the Standard ADM (top) and GEM (bottom) formalisms as a function of crossing time, t, for the Minkowski+noise spacetime using CrN(2) integration.*

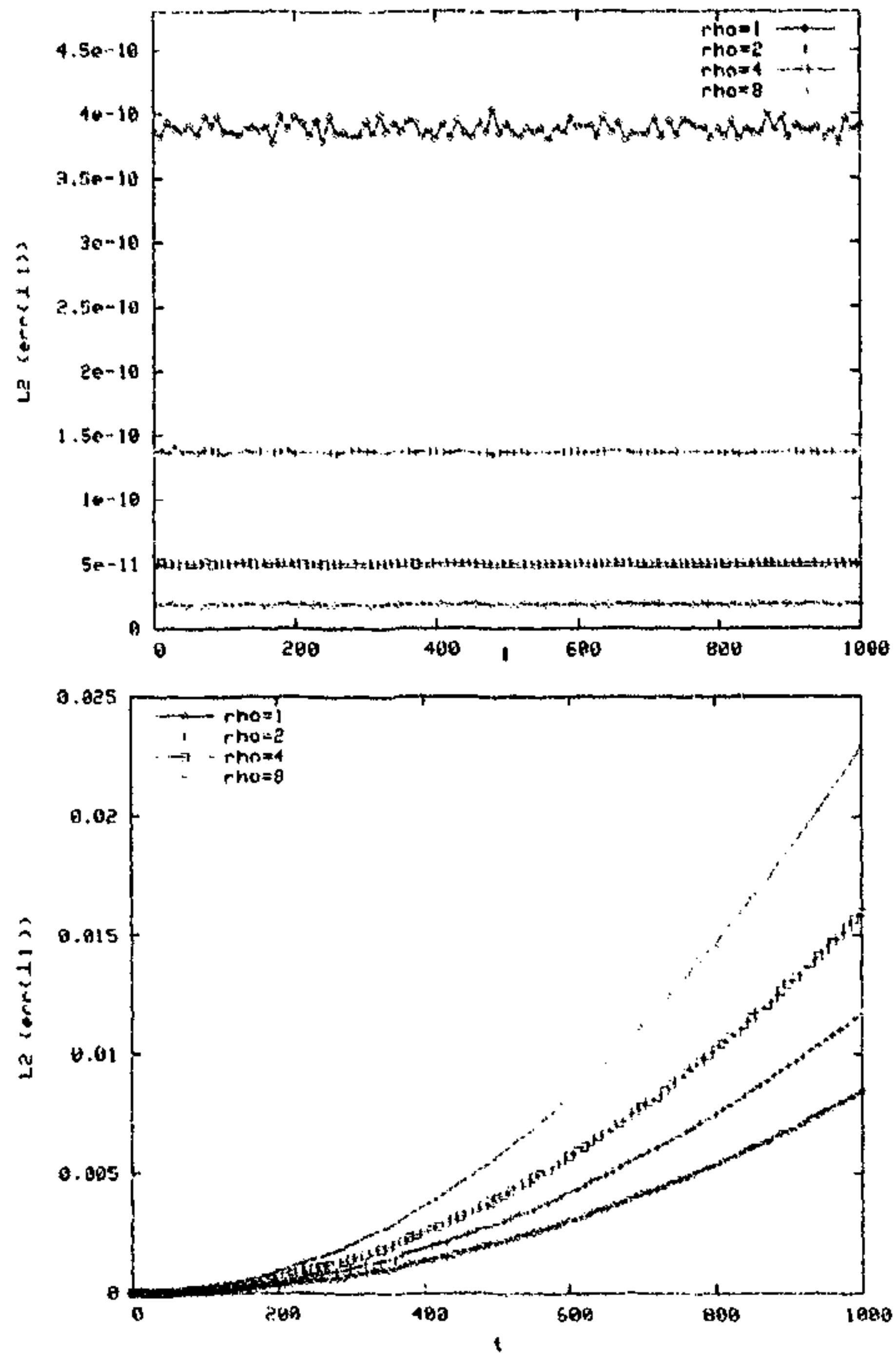

Figure 5.3: *The L_2 norm of the deviation of $\perp_1$ from Minkowski spacetime for the Standard ADM (top) and GEM (bottom) formalisms as a function of crossing time, t, for the Minkowski+noise spacetime using CrN(2) integration.*

Initially, the growth of the constraints using the GEM method are discouraging. Up until 1000 crossing times, however, the errors do not grow exponentially. We find that the momentum constraint grows linearly, whilst the error with respect to Minkowski spacetime and the Hamiltonian constraint both exhibit quadratic growth.

If we consider the growth of the errors throughout the first half of the first crossing time, we can glean some insight into why this happens, in this particular case. Figure 5.4 shows the evolution of the extrinsic curvature on the central portion of our grid ($\rho = 1$) for both methods, from the initial conditions through the first half crossing time.

From this we see that while the noise in the ADM case is propagated and "spread out" over time, the noise on each grid point grows on each step for GEM, and does not propagate through the grid. This is purely due to the fact that the only spatial derivatives left in our GEM equations (4.17 - 4.23) are derivatives of the gauge variable, α. Due to the fact that our lapse function remains constant ($\alpha = 1$) across the grid for all time, our set of evolution equations reduce to ordinary differential equations and consequently, each grid point is "cut off" from its neighbour, stopping information transmission across the grid.

The Standard ADM results recorded here could be attributed to a number of factors. Firstly, the simplified form of the one-dimensional equations effectively remove a number of the degrees of freedom that are present in the three-dimensional simulations (for example, we are implicitly demanding that all off-diagonal terms are identically equal to zero). More interestingly, it could tell us something about the

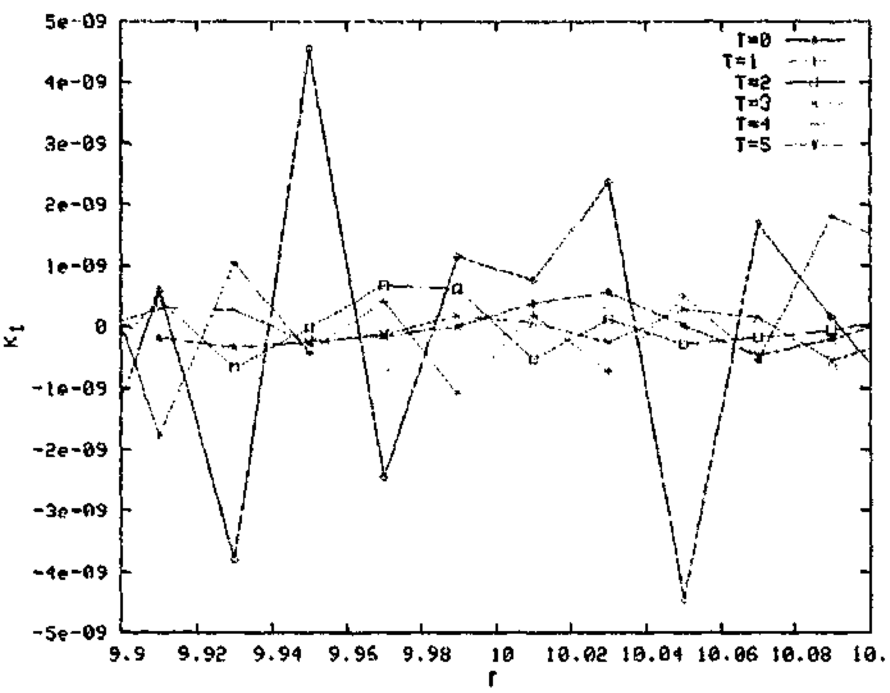

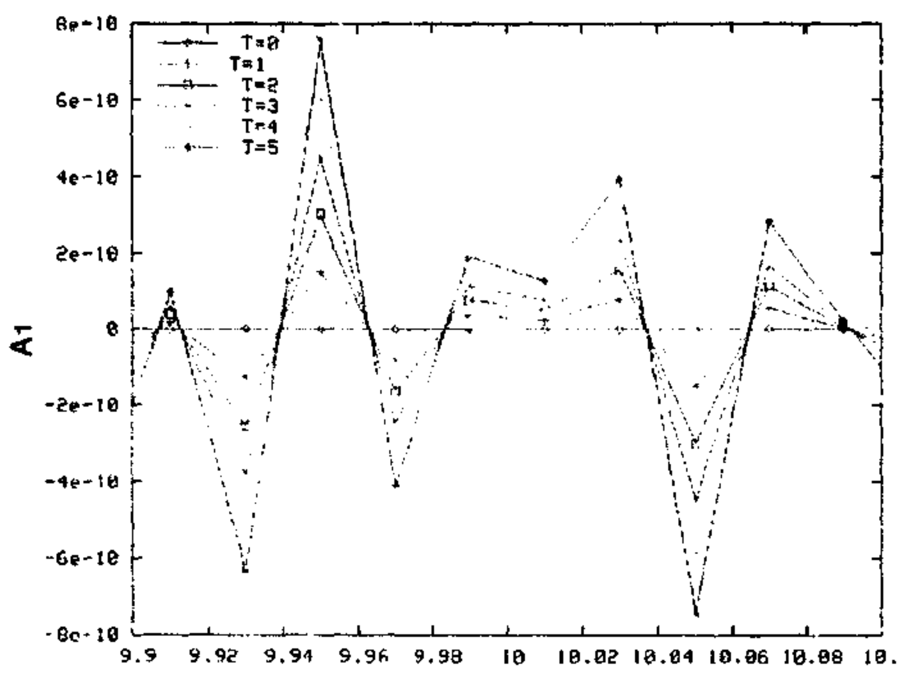

Figure 5.4: *The radial component of the extrinsic curvature (A_1 in GEM, K_1 in ADM) for the Standard ADM (top) and GEM (bottom) formalisms for the Minkowski+noise spacetime using CrN(2) integration.*

stability criteria for the ADM equations.

It is logical to assume that the ratio dt/dx, is related in some way (perhaps not trivially) to the Courant-Friedrichs-Lewy (CFL) condition [Courant et al., 1967] for our equations. If we vary dt/dx we see markedly different responses, particularly in the Standard ADM case. To test the relationship of dt/dx to stability we re-ran the $\rho = 2$ code, keeping the same spatial resolution (and hence the same initial noise to background ratio) but varying the temporal resolution. The results are summarised in table 5.1.

We see that both formalisms exhibit exponentially growing errors within one hundred light crossing times when $dt/dx \gtrsim 1$ ($dt/dx \gtrsim 1.5$ when a fourth-order Runge-Kutta integrator is used). The form of the growth is markedly different, however, when the two formalisms are compared, as in figures 5.5 and 5.6. For GEM we see that, until the instability reaches the 'runaway' stage (that leads to the code crashing within a few time-steps) the growth is polynomial in time. The Hamiltonian constraint exhibits quadratic growth, while the momentum constraint grows linearly.

The ADM case, however, shows clear exponential growth from early times (note the log scale on the y-axis). We also see that this unstable mode has definite periodicity, with the period much less than a light crossing time, implying that the errors are true 'grid phenomena', rather then caused by spurious boundary conditions or such. This result supports the findings of Jansen et al. [2003], who found similar behaviour in the 3-dimensional ADM equations. The behaviour of both methods lead us to employ a 4th order Runge-Kutta (RK(4)) algorithm [Press et al., 1996] for comparison and

		Standard ADM		GEM	
dt/dx	Method	Runs to T=100?	Exp. growth?	Runs to T=100?	Exp. Growth?
0.5	CrN(2)	Yes	No	Yes	No
0.75	CrN(2)	Yes	No	Yes	No
1.0	CrN(2)	Yes	Yes	Yes	No
1.1	CrN(2)	No (T_{crash} = 0.682)	Yes	No (T_{crash} = 12.8)	at late times
0.5	RK(4)	Yes	No	Yes	No
1.0	RK(4)	Yes	No	Yes	No
1.4	RK(4)	Yes	No	Yes	No
1.5	RK(4)	No (T_{crash} = 0.87)	Yes	No (T_{crash} = 12.03)	at late times

Table 5.1: *Stability as a function of dt/dx.*

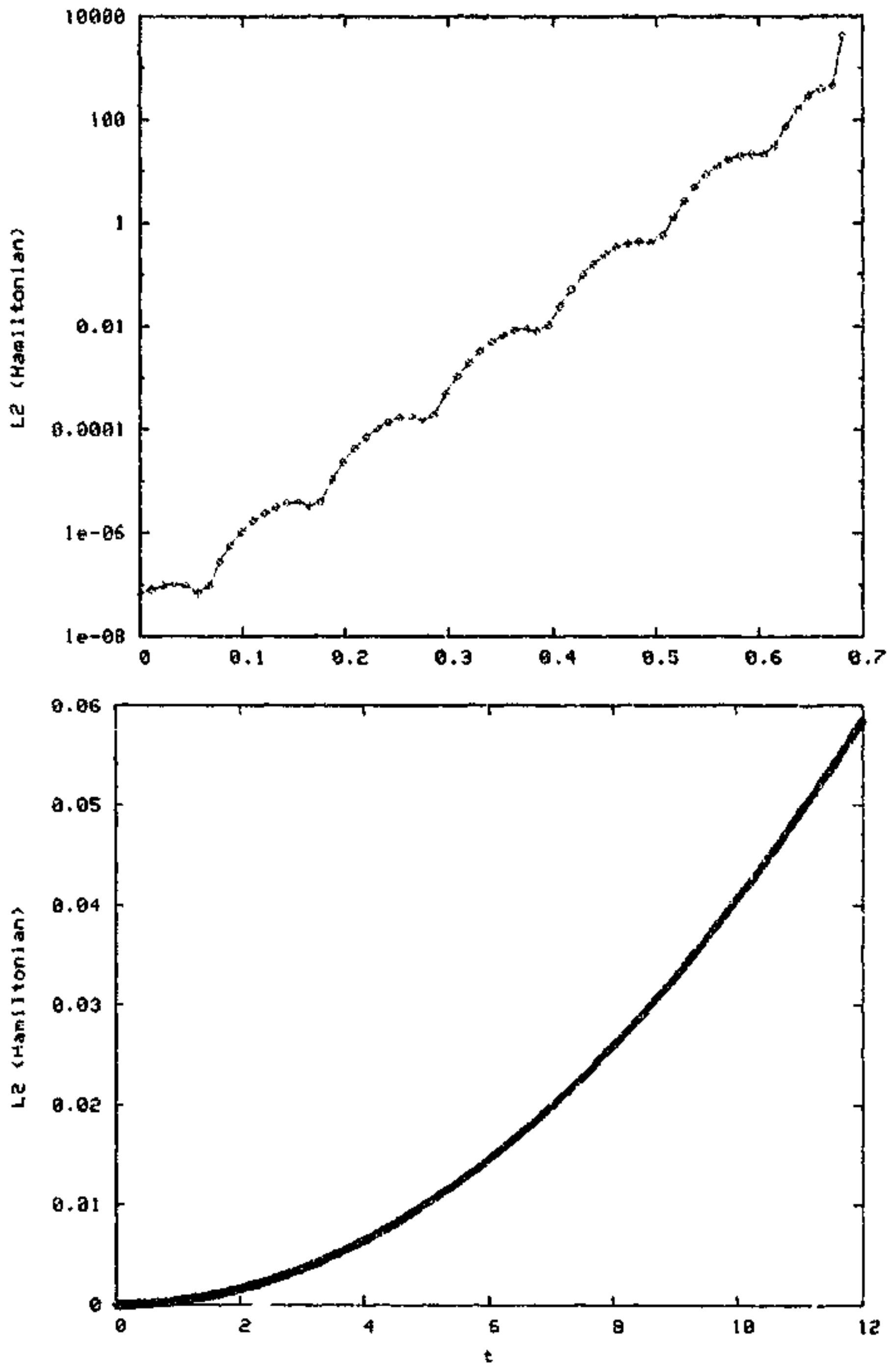

Figure 5.5: *The L_2 norm of the Hamiltonian constraint for the Standard ADM (top) and GEM (bottom) formalisms for the Minkowski+noise spacetime when $dt/dx = 1.1$. This shows the evolution until just before the 'runaway' instability sets in, for both cases. Note the difference in scale on the y-axis.*

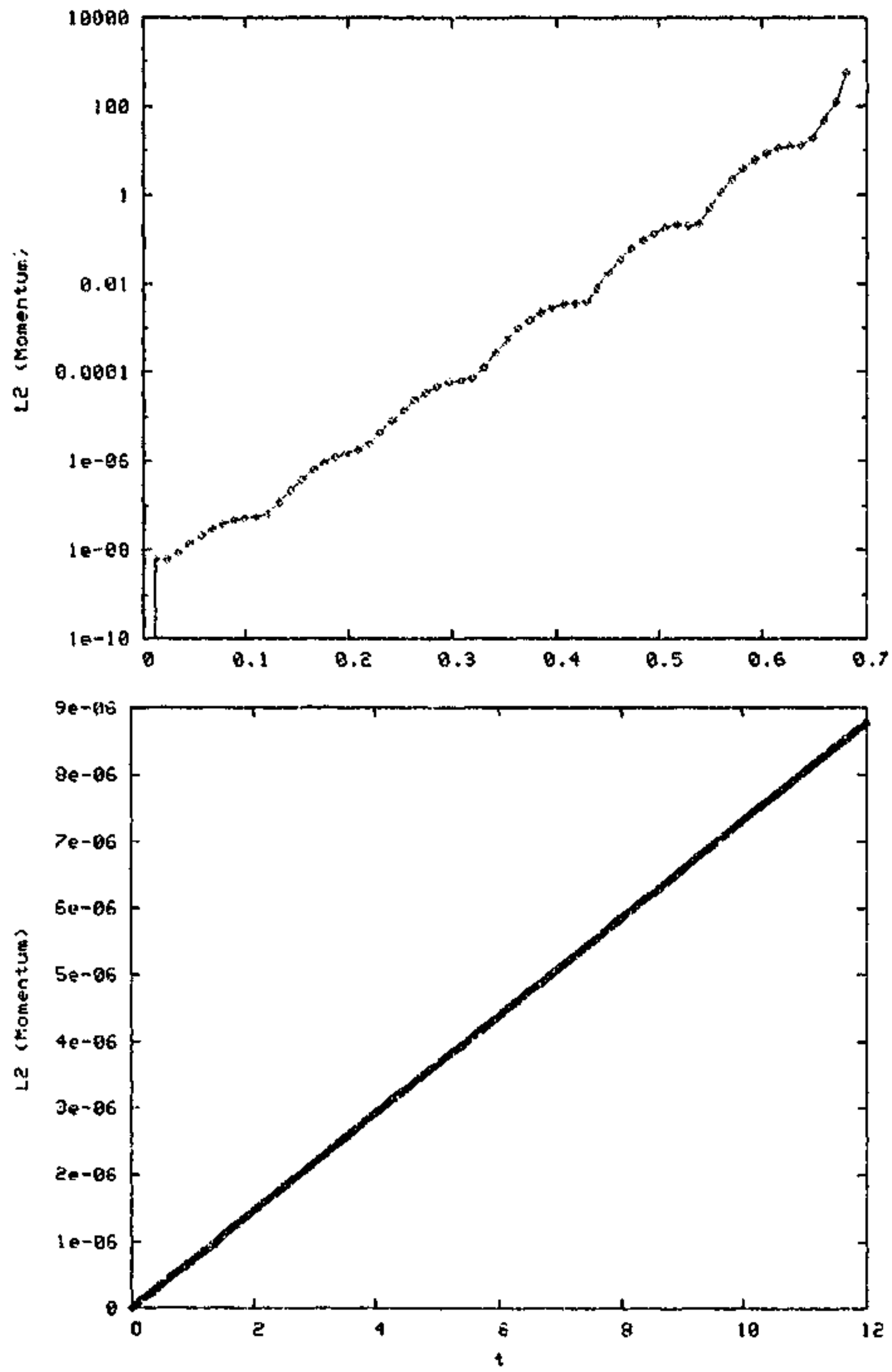

Figure 5.6: *The L_2 norm of the Momentum constraint for the Standard ADM (top) and GEM (bottom) formalisms for the Minkowski+noise spacetime when $dt/dx = 1.1$. Again, we are seeing the evolution until just before the 'runaway' instability causes the code to crash. Note the difference in scale on the y-axis.*

to establish that the stability behaviour previously discussed is not caused by our choice of time-stepping routine. RK(4) has the advantage of being less dissipative then Crank-Nicholson (as the leading error is of order $(\Delta t)^5$) and is widely regarded as a robust integrator for both partial and ordinary differential equations. As an example, figure 5.7 shows us the violation of the Hamiltonian constraint using Runge-Kutta (4), for $dt/dx = 0.5$ and $\rho = 1, 2, 4, 8$ (refer to figure 5.1 for comparison). As you can see there is little qualitative difference between the two integrators (nor was any difference noted in the growth of the momentum constraint, or in the deviation from flat space, though these are not pictured). The main difference we did note was a slight difference in the stable values of dt/dx (see table 5.1). We also see a slight trend toward constraint growth with ADM, though only in the finest grid case.

5.3 The Gauge Wave Spacetime

The Minkowski+Noise spacetime gives us an idea of how different sets of evolution equations, coupled to various numerical methods, behave in the presence of very high frequency oscillations in the initial data for even the simplest spacetimes. In this section we will test the performance of both methods in the presence of a low frequency perturbation. We do this by examining a "gauge wave" spacetime.

To construct a gauge wave spacetime we take flat minkowski spacetime and perform a coordinate transformation to write it in the form:

$$ds^2 = H(dx^2 - dt^2) + dy^2 + dz^2 \tag{5.9}$$

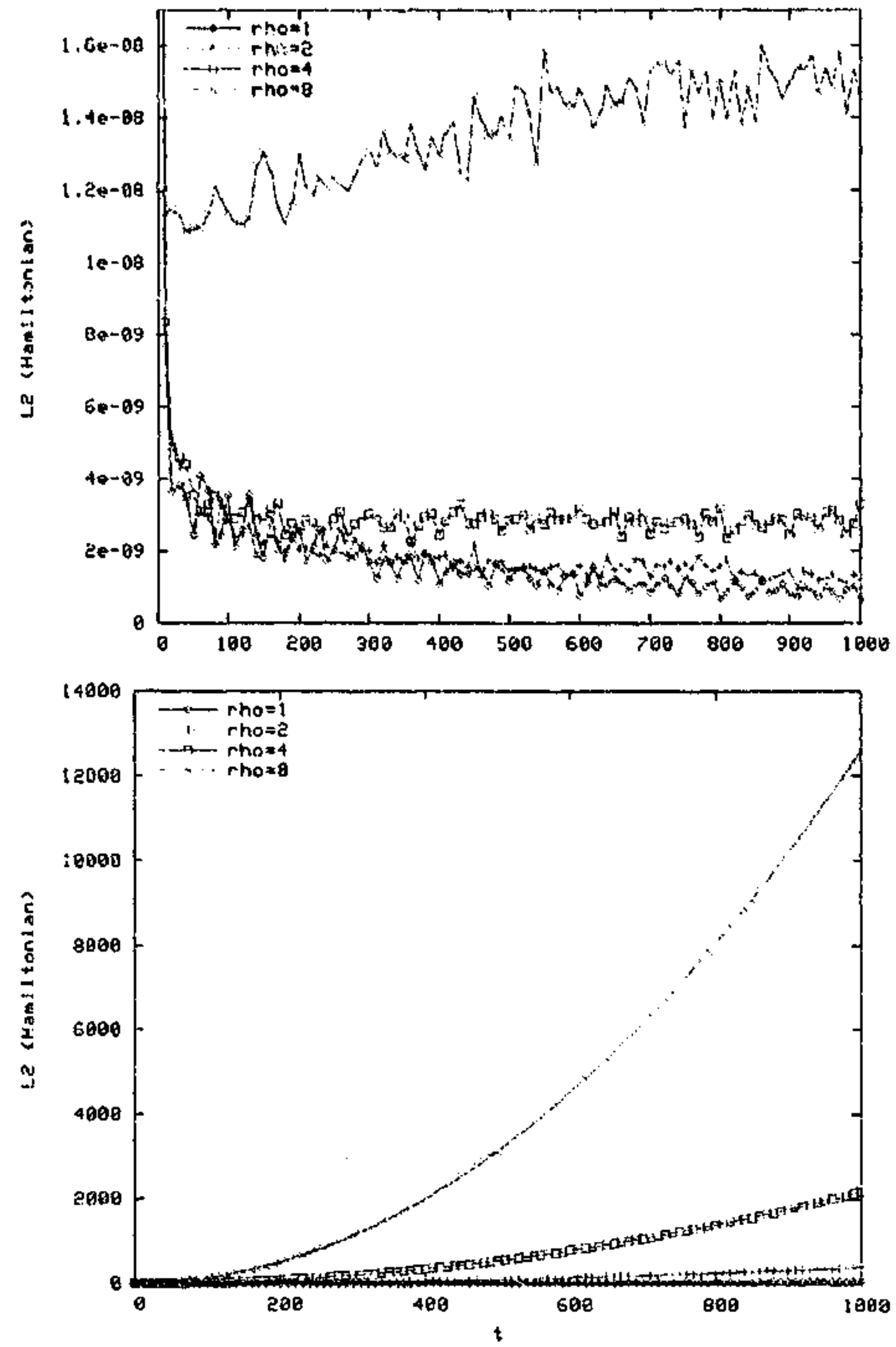

Figure 5.7: *The L_2 norm of the Hamiltonian constraint for the Standard ADM (top) and GEM (bottom) formalisms as a function of crossing time for the Minkowski+noise spacetime using RK(4) integration.*

where $H = H(x-t)$ is some positive function [Bona and Palenzuela, 2002] [Alcubierre et al., 2003a]. Although this is a cartesian, and not a spherically symmetric grid, it is a reasonably simple task to show that the symmetry arguments from the previous chapter (e.g. $B_{ij} = 0$) still hold.

Because equation (5.9) may be obtained from the Minkowski metric (5.1) by a simple change of coordinates (and the fact that the 4-Riemann tensor is identically equal to zero for the above metric) we see that equation (5.9) represents a completely flat spacetime. Thus any non-trivial evolution is a consequence of co-ordinate and gauge choices only.

Our choices for the function $H(x - t)$ are numerous. Previous investigations of these spacetimes have considered a range of choices, including Gaussian waves [Alcubierre, 1997] [Bona et al., 1998], trigonometric functions [Bona and Palenzuela, 2002] [Alcubierre et al., 2003a] and combinations of the two [Calabrese et al., 2002a] [Calabrese et al., 2002b]. Here, as in the previous section, we choose to follow Alcubierre et al. [2003a] and specify

$$H(x-t) = 1 + A\sin\left(\frac{2\pi(x-t)}{d}\right) \tag{5.10}$$

here A is the amplitude of the wave (we choose $A = 10^{-2}$ so that the perturbation remains small) and d is both the period of the wave and the size of the computational domain in the direction of propagation of the wave.

We initialise our one-dimensional grid as $x \in (-0.5, 0.5)$. Thus $d = 1$ in the above equation (5.10). This allows us to implement simple periodic boundary conditions, as

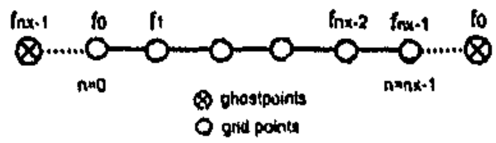

Figure 5.8: *Using ghostpoints to implement periodic boundary conditions : The value of a function on the ghostpoints is used to evaluate derivatives on the boundary grid points. The value of a given function on the left-most ghostpoint is set by remapping the value on the right-most grid point (and vice versa). In this way the computational domain has gone from being a line (or a n-cube in higher dimensions) to being a circle (or n-torus).*

in figure 5.8, by setting functions on the ghostpoint on the right-hand-side of the grid to be equal to their values first "real" grid point on the left-hand-side and vice versa. This eliminates errors from the boundary conditions and means we can focus on the influence of the gauge conditions alone.

Thus we have the following initial conditions for this simulation:

- $\Psi = 1$, i.e. not a conformal metric
- $\perp_1 = 1 + A\sin(2\pi x)$, $\perp_2 = 1$
- $K_1 = \frac{-\pi A\cos(2\pi x)}{\sqrt{1+A\sin(2\pi x)}}$, $K_2 = 0$
- $A_1 = -\frac{2}{3}\frac{\pi A\cos(2\pi x)}{\sqrt{1+A\sin(2\pi x)}}$, $A_2 = \frac{1}{3}\frac{\pi A\cos(2\pi x)}{(1+A\sin(2\pi x))^{3/2}}$, $tr(K) = \frac{-\pi A\cos(2\pi x)}{(1+A\sin(2\pi x))^{3/2}}$
- ${}^{(3)}R_1 = {}^{(3)}R_2 = {}^{(3)}Q_1 = {}^{(3)}Q_2 = {}^{(3)}R = 0$
- $E_1 = 0$, $E_2 = 0$, using the constraint equation (3.93)
- $\alpha = \sqrt{1 + A\sin(2\pi x)}$, $\beta = 0$

We expect to see a couple of things in this simulation. We have implemented periodic boundary conditions, rather than the more traditional requirement of asymptotic flatness. Thus there is no way for the gauge wave to leave the grid, which leads to interesting spacetime dynamics. We can see from equation (5.4) that $tr(K) < 0$ everywhere on a slice will drive an expansion of the volume element, $\sqrt{det(\perp)}$, whereas an everywhere positive value of $tr(K)$ must always lead to the focusing of observers' worldlines and the formation of a coordinate singularity [Wald, 1984]. Similarly any growth in the volume element (or a negative $tr(K)$) will drive a growth in the lapse function, which will, in turn drive the expansion . Conversely, a decrease in the volume element will lead to a 'freezing' of α (hence the singularity avoiding nature of the Bona-Masso family of slicing conditions in black hole spacetimes). Where tr(K) changes from positive to negative across the grid we may see expansion or collapse or both (the exact behaviour will be dependent on the formalism, algorithm etc.).

One thing to note though is that the evolution of the Minkowski+sinwave+harmonic slicing spacetime is expected to lead to a gauge pathology (whether that be expansion or collapse). What we are looking at here, then, is the ability of the GEM (and, in comparison ADM) evolution equations to follow the dynamics of the spacetime for a large number of light crossing times. We also hope to see that the errors in the evolution variables converge to the exact solution with increasing resolution.

Again, we use harmonic slicing to propagate the gauge variables and for comparison we use both iterated Crank-Nicholson and Runge-Kutta(4). We found no qualitative differences between the two, and thus present only the Crank-Nicholson results here. We also implemented harmonic slicing in two different ways: firstly by using the constraint equation (5.5) and secondly by evolving α according to equation (5.3). Again, no qualitative difference was found between the two.

5.3.1 Results

Figures 5.9 to 5.11 compare the qualitative behaviour of the Gaugewave simulation using the two formalisms. We show the value of key evolution variables at every 100 crossing times (with the initial condition for comparison) up to the 1000th crossing time. The results depicted here are from the $\rho = 2$ case, that is, from the second coarsest grid/dt choice. Thus the figures depict somewhat amplified gauge effects.

We can see that the qualitative behaviour of the primary evolution variables in both codes is very similar. Both show the expansion of the spacetime, through the behaviour of the 3-metric components in particular (fig. 5.9). We also see that the terms representing the 3-curvature are zero or very close to.*

It is also clear that both codes exhibit a growing phase error. This is most evident in the behaviour of the extrinsic curvature (fig. 5.10) which is becoming increasingly out of phase with increasing time. The exact solution has a period of one crossing time, but our numerical solution is drifting to the right with each successive crossing time. The drift is worse for the coarser grids, and the numerical solution (for both methods) converges to the exact solution with increasing resolution. This is illustrated in figure 5.12 showing the x component of the extrinsic curvature, A_1, in the GEM formalism

*Note that the 3-Ricci tensor remains identically equal to zero in the ADM case. This is ensured trivially due to the restrictions placed by demanding a 1-D simulation, and doesn't represent any advantage of this formalism.

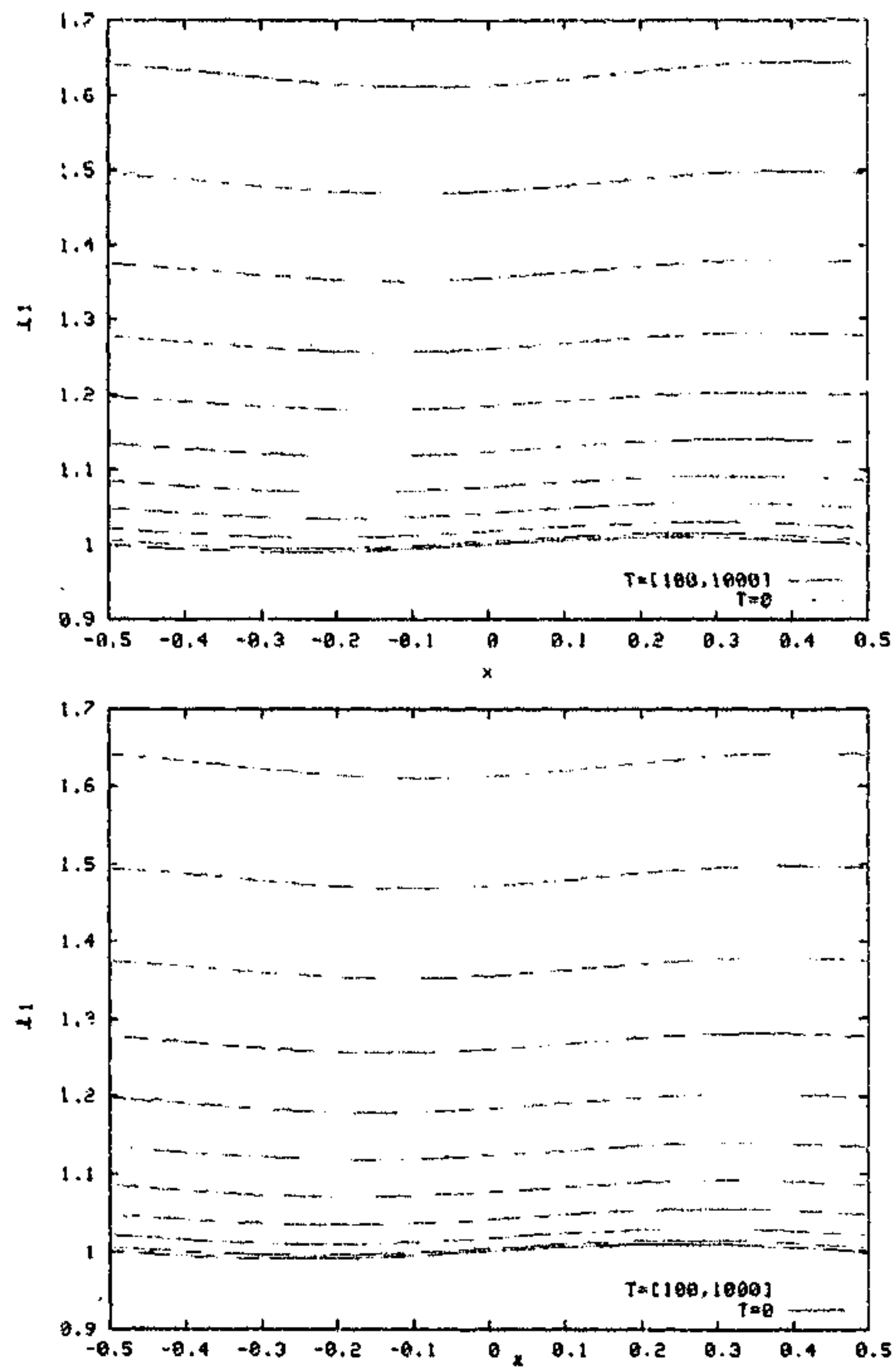

Figure 5.9: *The evolution of the nontrivial metric component ($\perp_1$) for the Minkowski+Sinwave spacetime ($\rho = 2$). Standard ADM is on the top, GEM on the bottom. Values were output every 100 crossing times.*

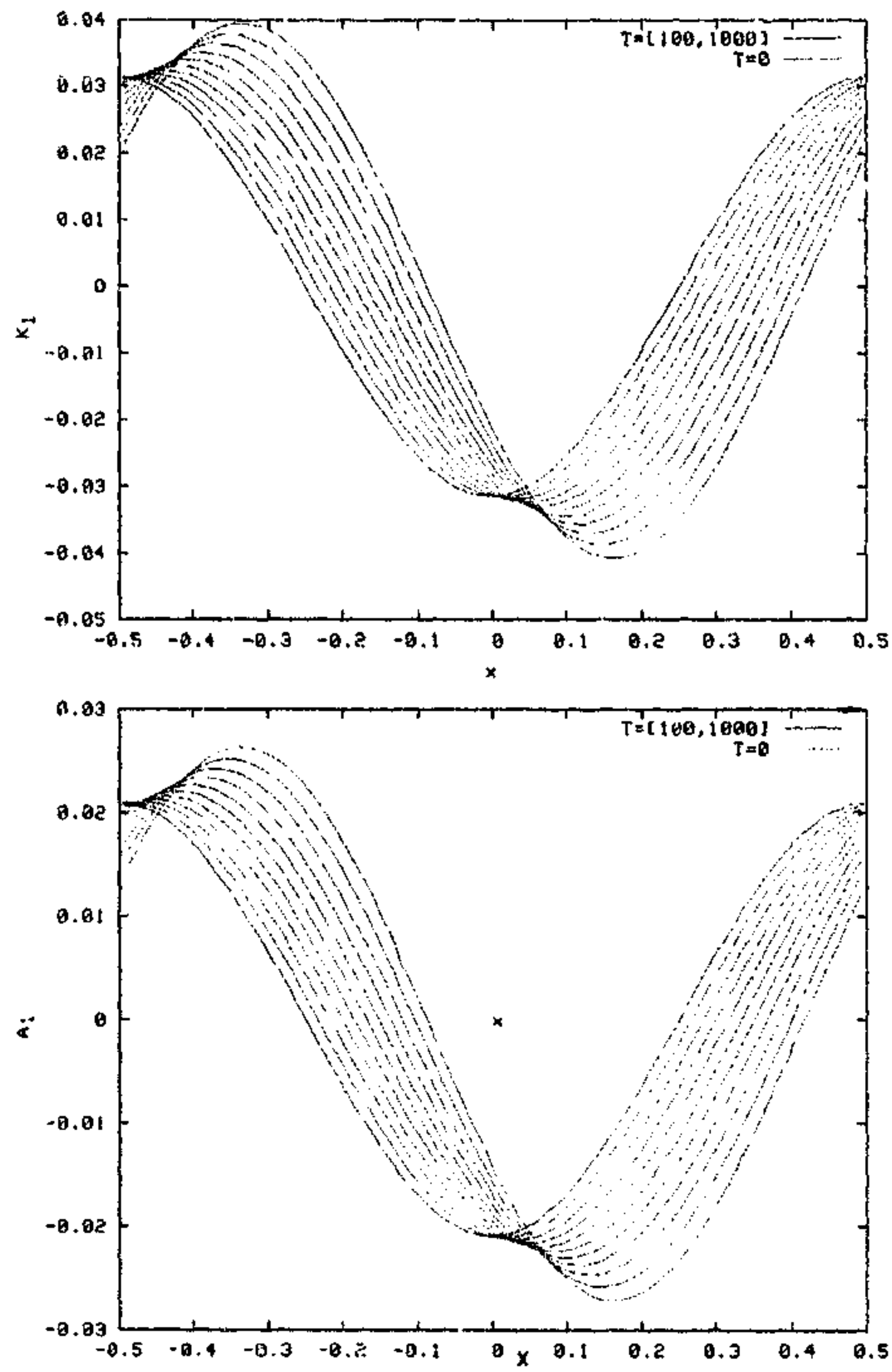

Figure 5.10: *The evolution of the nontrivial extrinsic curvature component (K_1 for ADM, A_1 for GEM) for the Minkowski+Sinwave spacetime ($\rho = 2$). Standard ADM is on the top, GEM on the bottom. Values were output every 100 crossing times.*

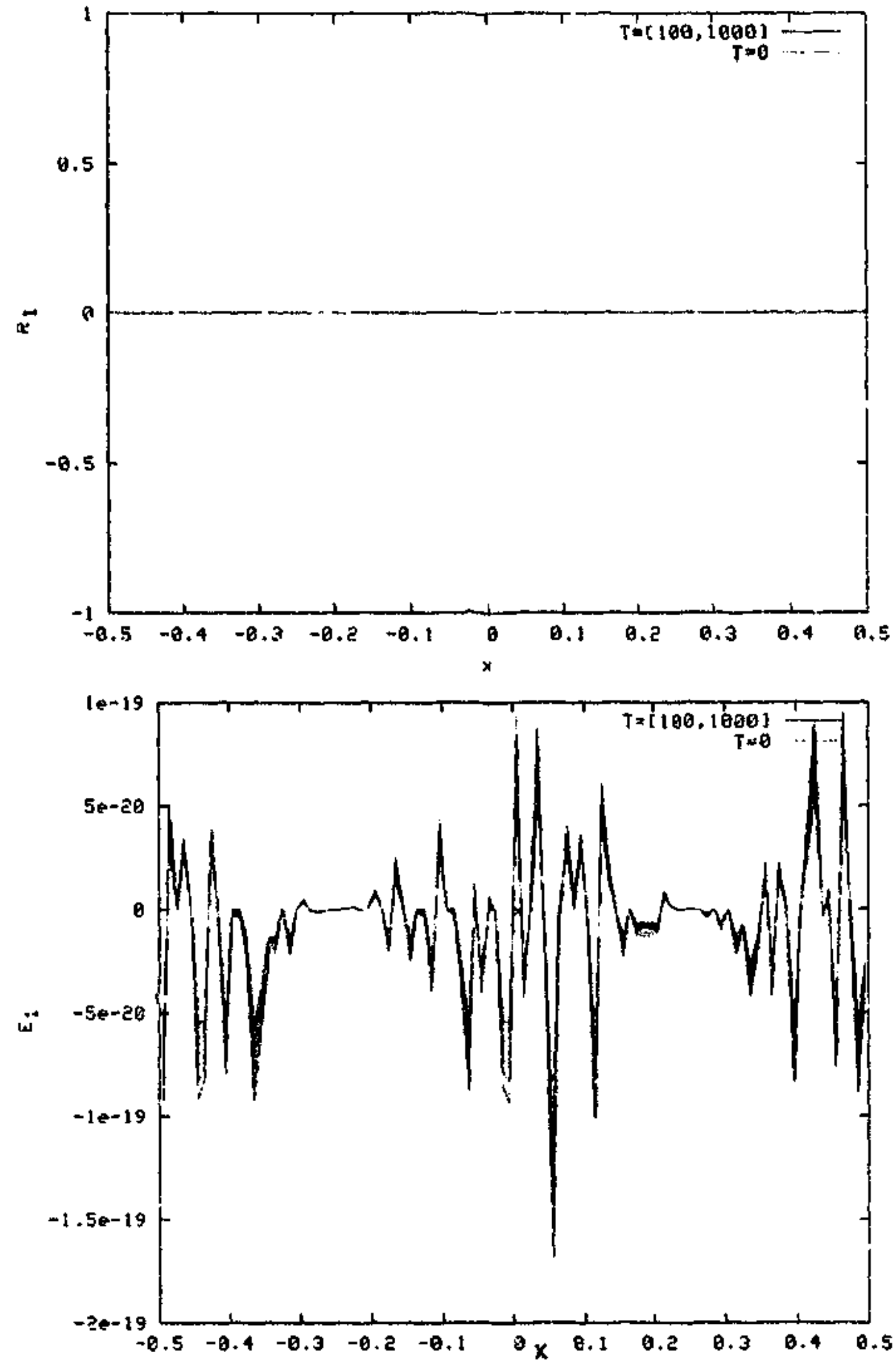

Figure 5.11: *The evolution of the curvature components (R_1 for ADM, E_1 for GEM) for the Minkowski+sinwave spacetime ($\rho = 2$). Standard ADM is on the top, GEM on the bottom. Values were output every 100 crossing times.*

after 500 light crossing times for each of the resolutions under consideration.

To examine further the behaviour of these errors with respect to the different grid resolutions we plot the behaviour of the error in $\perp_1$ as a function of time, for each resolution (figure 5.13). We note two things:

Firstly, the response of the two methods is almost identical. This similar behaviour tells us something about the gauge properties of the GEM formalism. As both the 3-Ricci and gravito-electric tensors are negligible throughout the simulation (refer to figure 5.11) the major difference between the two formulations, in this case, is the way in which the extrinsic curvature is treated. Recall that with the GEM evolution equations, (4.17) - (4.23), we have split up the extrinsic curvature into its trace and trace-free parts, thereby making the evolution of the kinematic variable, $tr(K)$, removed from the other variables. It would appear, in this test case at least, that this neither retards or encourages the development of gauge pathologies.

Secondly, the growth of the errors decreases with increasing spatial resolution (c.f. the response of the Standard ADM algorithm in the Minkowski+Noise test). This implies that we not detecting gauge modes here, but normal convergent behaviour. Note, however, that convergence is weakened at late times due to the algorithms' inability to accurately deal with the growth in the evolution variables as the spacetime expands.

We can see this quantitatively in figure 5.14. Here we have taken the three coarsest grids (corresponding to $\rho = [1, 2, 4]$) and calculated a convergence factor, σ, according-

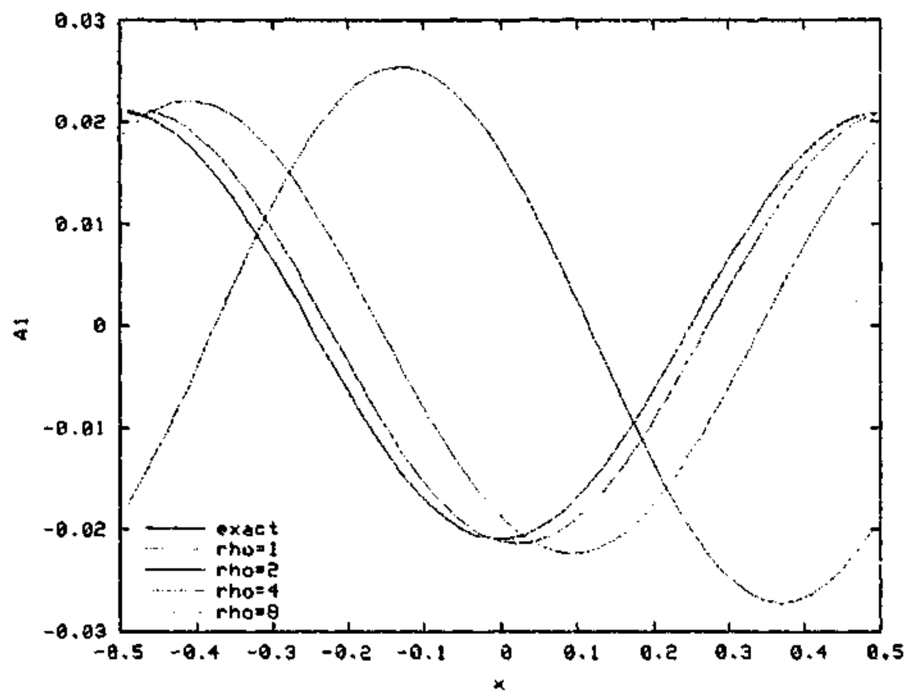

Figure 5.12: *The x-component of A_1 for GEM, as a function of x. The values were output after 500 light crossing times and show clear convergence toward the exact solution with increasing resolution.*

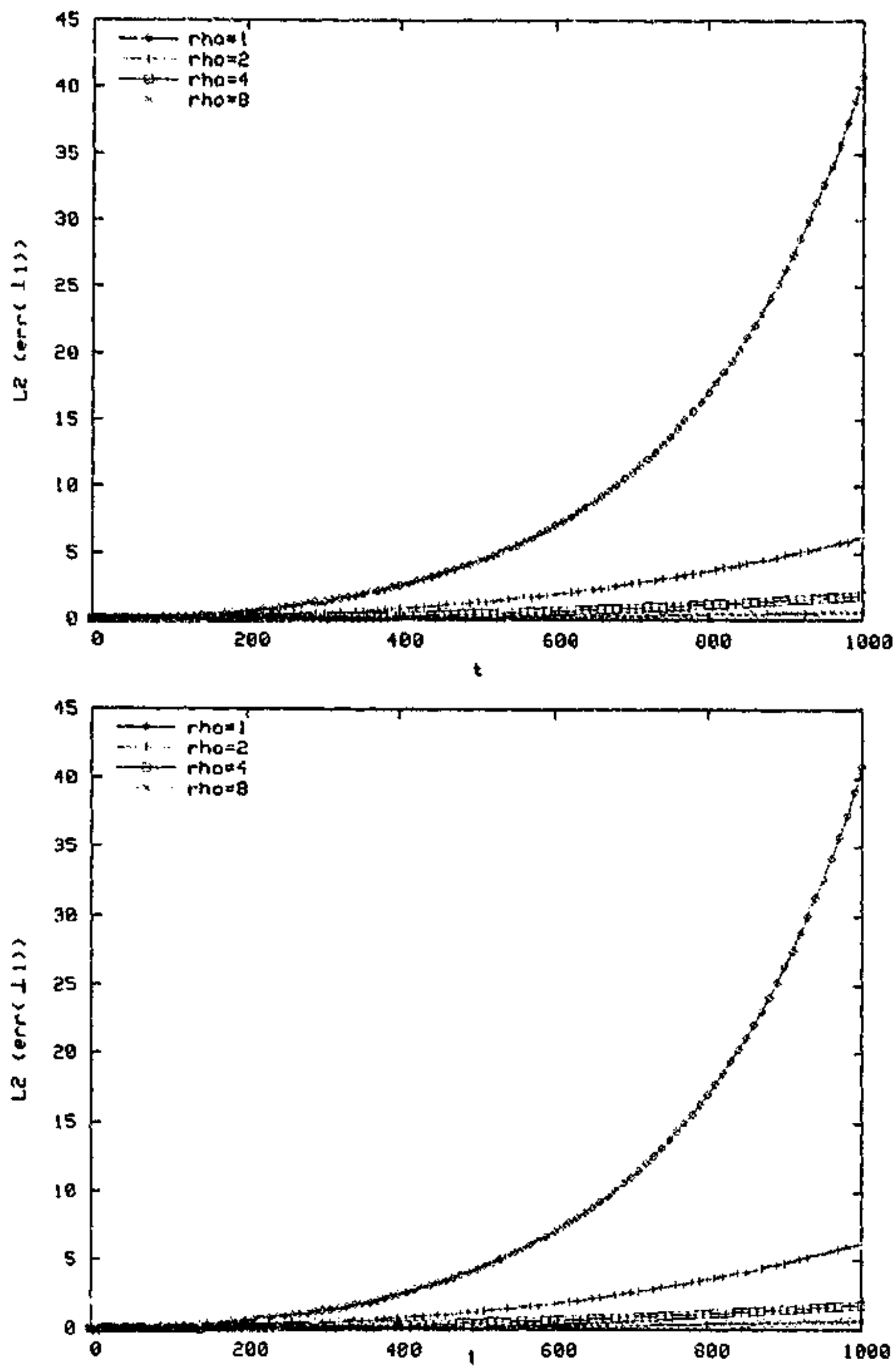

Figure 5.13: *The growth of errors in the $\perp_1$ component for the Minkowski+Sinwave spacetime (CrN(2) integration, $\rho = 2$). Standard ADM is on the top, GEM on the bottom.*

ing to

$$2^{\sigma} = \left| \frac{e_{\rho=1} - e_{\rho=2}}{e_{\rho=2} - e_{\rho=4}} \right| \tag{5.11}$$

where e is some error measure. We expect that for second order convergence we will have $\sigma = 2$, for fourth order $\sigma = 4$, etc.. In figure 5.14 we show the convergence factor, calculated from the error in $\perp_1$, as a function of time. Note that both the Crank-Nicholson ($O(\Delta x^2)O(\Delta t^2)$) and Runge-Kutta ($O(\Delta x^2)O(\Delta t^4)$) show the expected second order convergence at early times. However, both ADM and GEM show a deviation from this convergence as the integration progresses. This behaviour may influence the long term stability and convergence of more general spacetimes, using both these formalisms, though, naturally the convergence of the scheme will also be dependent on gauge choice, boundary conditions, etc.. This highlights the importance of not only testing accuracy, but also convergence where possible.

Keeping these points in mind, in the next chapter we shall look more closely at the behaviour of the GEM formalism in non-flat spacetimes. We do this by considering a range of slicings of a simple, spherically symmetric spacetime containing a Schwarzschild black hole.

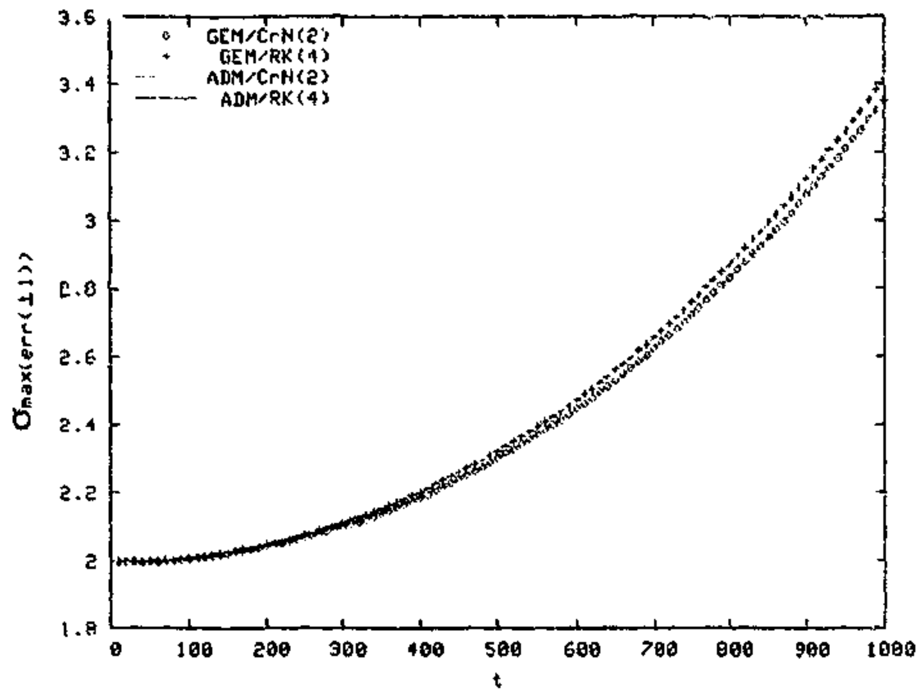

Figure 5.14: *The convergence factor σ for the gauge-wave spacetime. Both ADM and GEM show the same behaviour, namely second order convergence at early times and divergence from this as the gauge dynamics become dominant at late times.*

Chapter 6

Tests of Schwarzschild Spacetimes

6.1 Properties of the Schwarzschild Solution

The Schwarzschild geometry is of fundamental importance in numerical general relativity. Theory shows this geometry to be the end-state of dynamical spacetimes such as the merger of compact objects and some supernovae explosions. As such, any dynamical approach to the Einstein equations should be able to accurately and stably model this geometry. Also, although the physical singularity of the black hole is a non-trivial thing to model, the spacetime is spherically symmetric and admits exact solutions in a variety of coordinates, making it an obvious test-case for any numerical relativist. However, as we saw in the previous chapter "simple" spacetimes do not necessarily lead to trivial numerical implementations.

In this chapter we shall continue our discussion of the numerical properties of the GEM formalism, with an emphasis on modelling the dynamics of a Schwarzschild spacetime. We shall look at the behaviour of the formalism in handling the gauge dynamics for a number of slicings of a spherically symmetric black hole spacetime.

Historically, the first line-element to describe a black hole is given in Schwarzschild coordinates, $[t_s, r, \theta, \phi]$, by

$$ds^2 = -\left(1 - \frac{2M}{r}\right)dt_s^2 + \left(1 - \frac{2M}{r}\right)^{-1} dr^2 + r^2 d\theta^2 + r^2 \sin^2\theta d\phi^2 \qquad (6.1)$$

As well as the physical singularity at $r = 0$ this coordinate system exhibits a coordinate singularity at $r = 2M$, which represents the event horizon of the black hole. We can see that this is truly a coordinate phenomenon by transforming our metric into the conformally flat isotropic coordinates, $[t_{iso}, \bar{r}, \theta, \phi]$, to obtain

$$ds^2 = -\left(\frac{1 - M/2\bar{r}}{1 + M/2\bar{r}}\right)^2 dt_{iso}^2 + (1 + \frac{M}{2\bar{r}})^4 \left[d\bar{r}^2 + \bar{r}^2(d\theta^2 + \sin^2\theta d\phi^2)\right] \qquad (6.2)$$

where $r = \bar{r}(1 + \frac{M}{2\bar{r}})^2$ We see that this coordinate system is completely regular at $\bar{r} = 2M$, however g_{tt} goes to zero at $\bar{r} = M/2$. This represents the isometry surface of the black hole, where the coordinate $\bar{r}$ undergoes the transformation $\bar{r} \to M^2/4\bar{r}$. This is equivalent to $r = 0$ in Schwarzschild coordinates.

In this work we shall make use of the following line-element (with coordinates $[t, \eta, \theta, \phi]$) to describe our black-hole:

$$ds^2 = -\tanh^2(\eta/2)dt^2 + \left[\sqrt{2M}\cosh(\eta/2)\right]^4 (d\eta^2 + d\theta^2 + \sin^2\theta d\phi^2) \qquad (6.3)$$

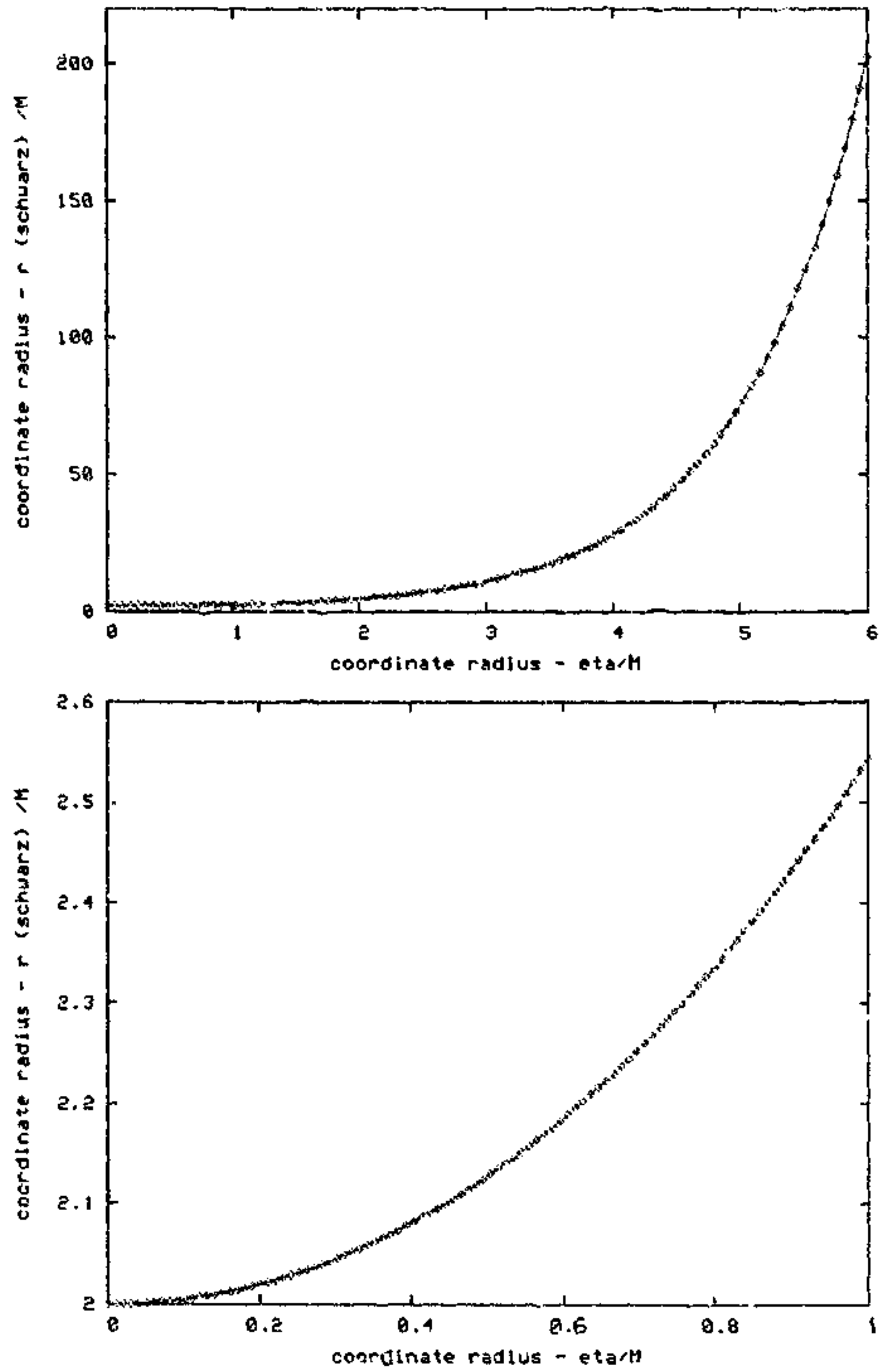

Figure 6.1: *Comparison of Schwarzschild (r) and η coordinates.*

where $\bar{r} = \frac{M}{2}e^{\eta}$ or, alternatively, $r = 2M\cosh^2(\eta/2)$. This coordinate system has been used previously (most useful for us is Bernstein [1993] upon which we base the tests in this chapter) and has a few properties that are worth noting. By inspection of the line-element, the η radial coordinate is symmetric about $\eta = 0$ giving us natural inner boundary conditions. Figure 6.1 shows the behaviour of the radial coordinate in comparison to standard Schwarzschild coordinates. We see that $\eta \in [0M, 6M]$ corresponds to the interval $r \in [2M, 200M]$. Thus we can cover a much greater portion of the underlying spacetime with less grid points than in Schwarzschild coordinates. We note also that $\eta = 0$ corresponds to $r = 2M$, so if we set up our grid with the innermost grid point at $\eta = 0$ we are, in fact, placing this point on the event horizon.

6.2 Initial and Boundary Conditions

For each of the slicings under consideration in this chapter, we initialise the evolution variables as

- $\Psi = \sqrt{2M}\cosh(\eta/2)$, i.e. we use a time-independent conformal factor
- $\tilde{\perp}_1 = 1, \tilde{\perp}_2 = 1$
- $\tilde{K}_1 = \tilde{K}_2 = \tilde{A}_1 = \tilde{A}_2 = tr(K) = 0$, i.e. a time-symmetric initial slice.
- ${}^{(3)}R_1 = {}^{(3)}Q_1 = -1/(\cosh^2(\eta/2))$
  ${}^{(3)}R_2 = {}^{(3)}Q_2 = -1/(2\cosh^2(\eta/2))$
  ${}^{(3)}R = 0$ using (4.6) to (4.8)

- $E_1 = {}^{(3)}Q_1$, $E_2 = {}^{(3)}Q_2$, using the constraint equation (3.93)

We also set $\eta_0 = 0$ and $\eta_{max} = 6 - d\eta$ throughout. Standard resolution is $dt = 0.005M$, $d\eta = 0.0075$ (800 grid points).

The inner boundary conditions are set using symmetry conditions rather than more complicated excision techniques. We implement ghost points on the inner boundaries and set the values of the evolution variables on the ghost points via symmetry. That is, if a function f, defined on the discrete nodes $i = 0 \rightarrow i = nx$ by the discrete values f_i, is symmetric about the isometry surface we set $f_{ghost-point} = f_1$ and if f is antisymmetric $f_{ghost-point} = -f_1$. We use the ghost point values when evaluating derivatives on the throat ($\eta = 0$).

On the inner boundary, symmetry of the coordinates tells us that the metric is symmetric about $\eta = 0$ and we choose the lapse to be symmetric also (to allow evolution on the throat). The shift vector (see the following chapter) is chosen to be antisymmetric about $\eta = 0$. These conditions lead to the extrinsic curvature and gravito-electric tensor also being symmetric about $\eta = 0$.

Although the asymptotic flatness of the spacetime allows us to make some judgements about the form of the functions on the outer boundary, we choose a free evolution here (except where specific conditions were necessary for determining the gauge variables). We obtain a value for functions on the outer ghost point by fitting a curve through the outer values of each of the variables and extrapolating along this curve.

We investigated two fitting functions

$$P_x = q_0 + q_1 e^{-x} + q_2 e^{-2x} \tag{6.4}$$

and

$$P_x = q_1 + q_2 x + q_3 x^2 \tag{6.5}$$

where x is the coordinate position in the x^1 direction (which is the radial direction, η, in this particular case). The two fitting functions were found to give similar results, unless otherwise indicated. We use equation (6.4) as a default.

6.3 Geodesic Slicing

Choosing the coordinate system attached to Eulerian observers who are falling along geodesics is a natural place to start our exploration of the behaviour of the GEM equations in a Schwarzschild spacetime. This slicing also admits exact solutions. Geodesic slicing is obtained by making the gauge choice

$$\alpha = 1 \tag{6.6}$$

$$\beta^i = 0 \tag{6.7}$$

Clearly, in this gauge, the proper time, τ, of the infalling observers is equivalent to the coordinate time, t. This follows by inspection of the 3+1 line element (4.1). To construct the exact solution with which we compare our code's performance, we shall follow Misner et al. [1973] and, to recast the equations into our coordinates we have followed the work of Bernstein [1993]. As the full derivation is available in Bernstein [1993] we shall merely sketch out the steps here.

The geodesic of an infalling test particle is found by integrating

$$\tau = \int d\tau = \int \frac{dr_s}{[2M/r_s - 2M/r_{s,o}]^{1/2}} \tag{6.8}$$

where the particle starts from rest at Schwarzschild radial coordinate $r_s = r_{s,o}$. The solution is given in parametric form, with respect to the parameter ω, by

$$r_s = \frac{r_{s,o}}{2}(1 + \cos\omega) \tag{6.9}$$

$$\tau = \frac{r_{s,o}}{2}\sqrt{\frac{r_{s,o}}{2M}}(\omega + \sin\omega) \tag{6.10}$$

A particle starting at $r_{s,o} = 2M$ will fall from rest (when $\omega = 0$) to the singularity (when $\omega = \pi$) in proper time

$$\tau = \frac{\pi}{2} r_{s,o}\left(\frac{r_{s,o}}{2M}\right)^{1/2} = \pi M \tag{6.11}$$

On the initial slice, our inner-most grid point is located at $\eta = 0$, which is equivalent to $r_s = 2M$ (see figure 6.1). As our observers fall toward the physical singularity, an observer at $\eta = 0$ will measure the coordinate volume to be decreasing to zero. The volume element will reach zero in $\tau = t = \pi M$. At this point our inner-most observer will hit the singularity and our numerical simulation will crash. This provides us with a simple first verification of the accuracy of our code.

To convert from (t_s, r, θ, ϕ) coordinates to (t, η, θ, ϕ) we note that $t = \tau$ and $r_{s,0} = 2M\cosh^2(\eta/2)$ and we perform a coordinate transformation (where the s denotes Schwarzschild coordinates and metric) according to

$$g_{\mu\nu} = g^s_{\sigma\tau} \frac{\partial x^\sigma}{\partial x^\mu_s} \frac{\partial x^\tau}{\partial x^\nu_s} \tag{6.12}$$

to obtain the following cumbersome, but exact, solutions for the ADM variables

$$\tilde{\perp}_2^{exact} = \frac{1}{4}(1+\cos\omega)^2 \tag{6.13}$$

$$\begin{aligned}\tilde{\perp}_1^{exact} = & \frac{\sin^2\omega(\sin^2\omega + 6\omega\sin\omega + 8\cos\omega + 9\omega^2 - 8)\sinh^2(\eta/2)}{(32\sinh^2(\eta/2)(1+\cos\omega) - 16\cosh^2(\eta/2)\sin^2\omega} \\ & + \frac{8(1+\cos\omega)(3\omega\sin\omega + 4)\sinh^2(\eta/2)}{(32\sinh^2(\eta/2)(1+\cos\omega) - 16\cosh^2(\eta/2)\sin^2\omega} \\ & - \frac{\sin^2\omega[\cosh^2(\eta/2)(1+\cos\omega) - 2](\sin^2\omega(\cos\omega - 3) + (1+\cos\omega)(8+3\omega\sin\omega))^2}{16(1+\cos\omega)(\cosh^2(\eta/2)\sin^2\omega(3+\cos\omega) - 2\sin^2\omega - 4\sinh^2(\eta/2)(1+\cos\omega)^2}\end{aligned} \tag{6.14}$$

$$\tilde{K}_1^{exact} = -\frac{\tilde{\perp}_1^{exact}(\sin\omega\cos\omega + 3\omega + 4\sin\omega)}{(M\cosh^3(\eta/2)(1+\cos\omega)(2(1+\cos\omega)^2 + 3\omega\sin\omega + 3\sin^2\omega))} \tag{6.15}$$

$$\tilde{K}_2^{exact} = \frac{\sin\omega}{4M\cosh^3(\eta/2)} \tag{6.16}$$

We implement the exact solution by using a numerical root-finder algorithm (a simple mid-point rule) to solve for ω using (6.10) and then use the above equations to generate the exact solution throughout the simulation.

Figure 6.2 shows the evolution of the GEM variables in this slicing. We can see that all the action is taking place near the throat, whilst the spacetime is asymptotically flat (note that the computational grid was defined by $\eta \in [0, 6)$ but we only show the inner portion of the grid to highlight the dynamics). We see clear evidence of the

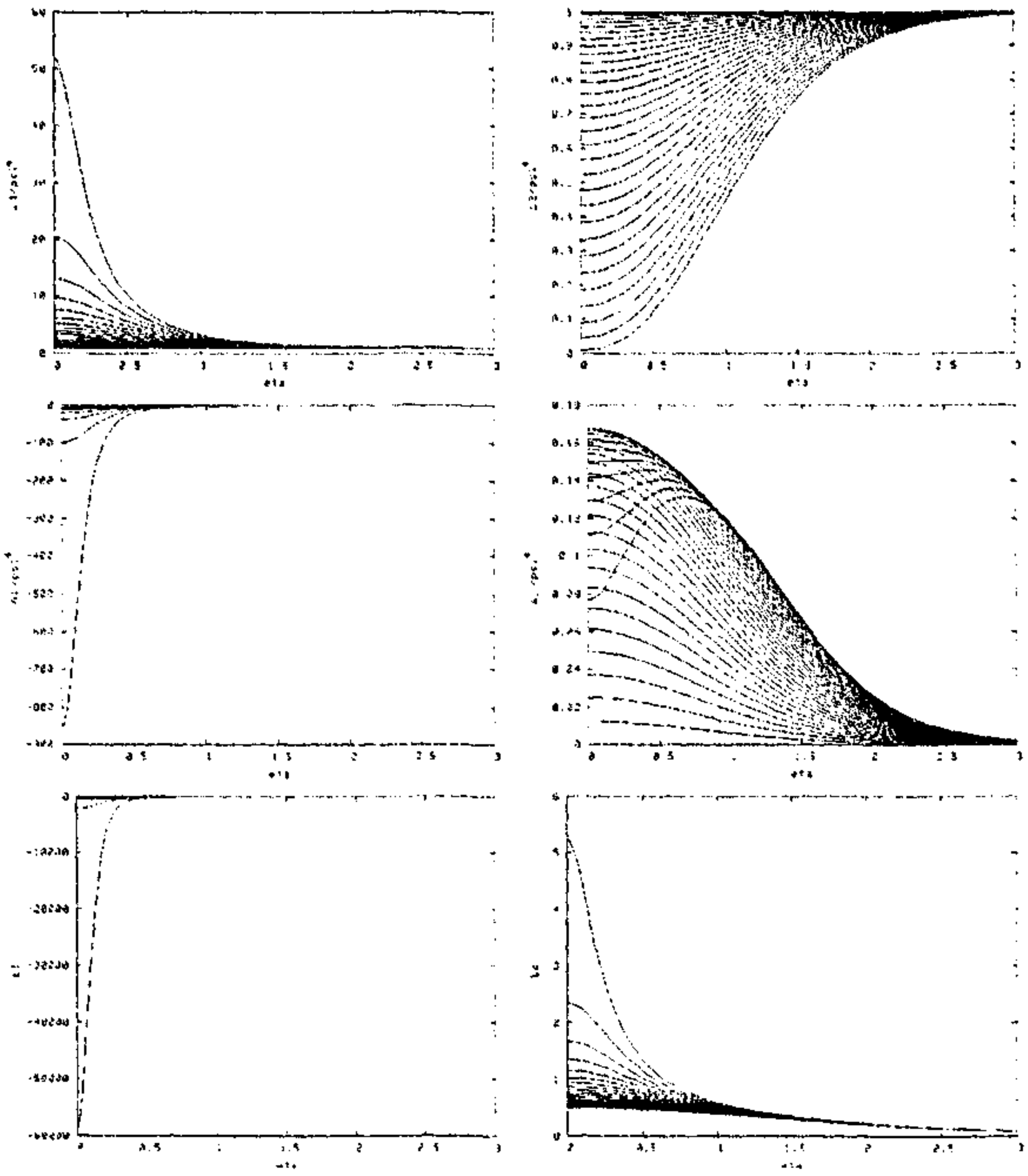

Figure 6.2: *Evolution of the 3-metric (top) the trace-free part of the extrinsic curvature (middle) and the gravito-electric part of the spacetime (bottom) for geodesic slicing implemented in the GEM formalism. Results are plotted from t=0M to t=3.1M, in increments of 0.1M. Time-stepping was CrN(2)*

underlying spacetime stretching in the radial direction from the behaviour of $\tilde{\perp}_1$, $\tilde{A}_1$ and E_1 from the large gradients developing in the variables as the coordinate time approaches πM. We also see the contraction of the volume element, most noticeably in $\tilde{\perp}_2$, which approaches zero on the throat. $\tilde{\perp}_2 = 0$ signifies that the volume element has decreased to zero (i.e. the first test particle has hit the physical singularity) and the code will crash shortly after. We found that the GEM equations reproduced the qualitative behaviour of this slicing accurately, and that for all combinations of dt, $d\eta$ and time-stepping algorithm (see below) tested the code crashed within a couple of time-steps of $t = \pi M$.

The ability to generate an exact solution means that we are able to use this slicing to run convergence tests, to convince ourselves that our formalism tends toward the exact Schwarzschild solution. This also enables us to quantitatively compare our results with those obtained using the standard ADM equations, and to highlight some of the properties of our equations. We check convergence with both dt and $d\eta$. For checking convergence with dt we use a standard grid resolution of $d\eta = 0.075$ (800 grid-points) and for convergence with $d\eta$ we use $dt = 0.005M$ for all runs. We use the exact solution to calculate the relative error in our numerical functions using

$$err(f) = \left|\frac{f - f_{exact}}{f_{exact}}\right| \tag{6.17}$$

and we calculate convergence at $t = 3M$.

As was the case in section 5.2 the choice of geodesic slicing reduces the 1D GEM equations to a set of ordinary differential equations, as all derivatives of the lapse

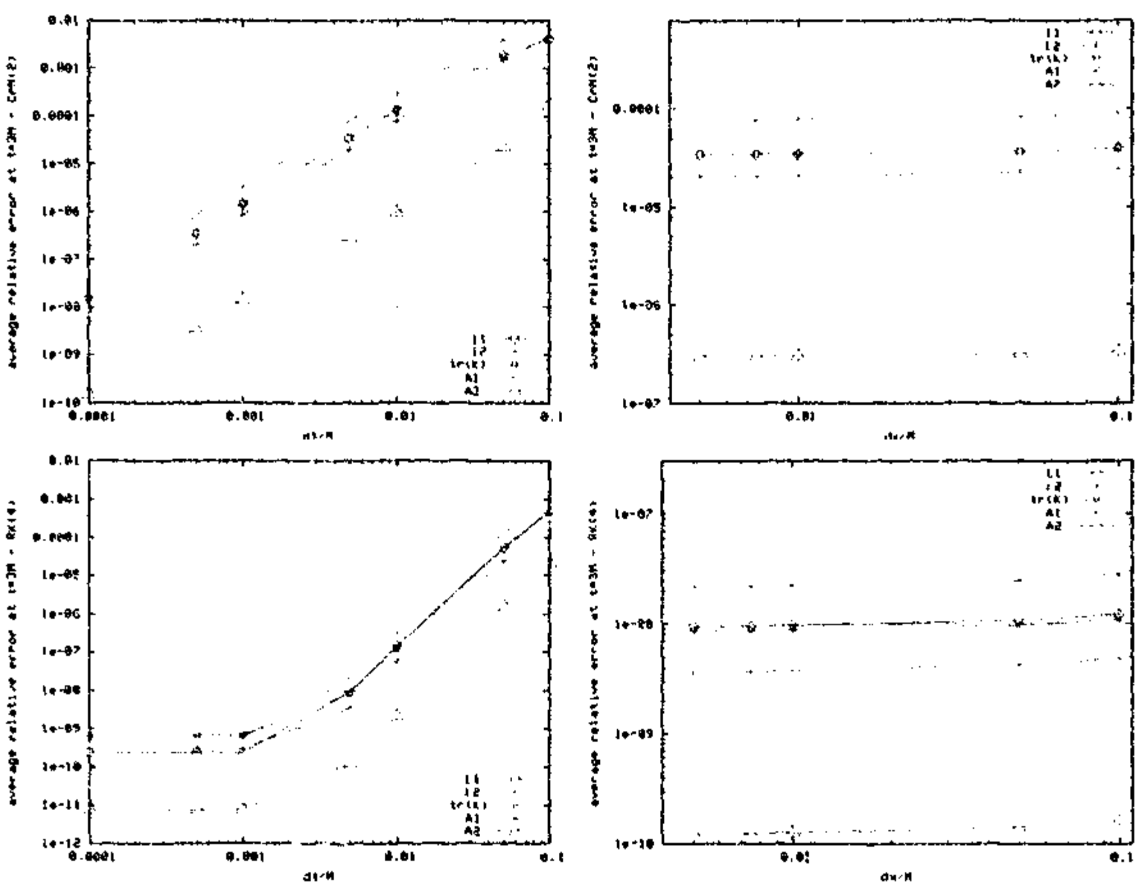

Figure 6.3: *Convergence of errors at t=3M for GEM. The top line shows the convergence with dt (left) and dη (right) for CrN(2) time-stepping. The bottom line shows results for RK(4) (convergence with dt on left and dη on right).*

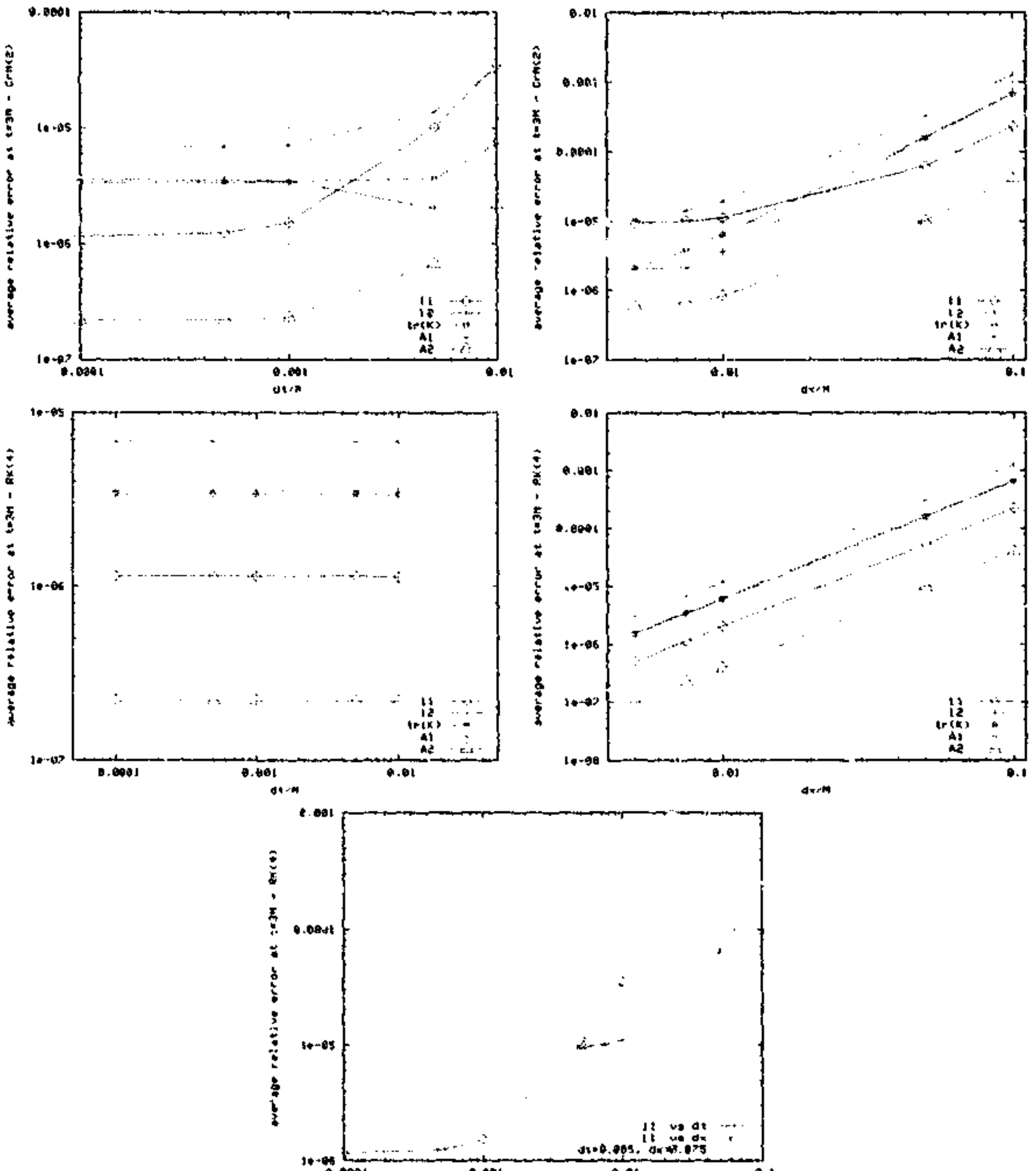

Figure 6.4: *Convergence of errors at t=3M for ADM. The top line shows the convergence with dt (left) and dη (right) for CrN(2) time-stepping. The second line shows results for RK(4) (convergence with dt on left and dη on right). The bottom graph shows the convergence of $\perp_1$ with respect to both dt and dη to illustrate the inter-dependence of the two.*

function are zero. Thus the accuracy of our equations in this case are independent of the grid's spatial resolution. This will not be the case in more general slicings, but here it leads to the convergence behaviour we see in figure 6.3. We see clear second order convergence with time using second order Crank Nicholson and fourth order convergence with time using Runge-Kutta (4). Note that the seeming non-convergence at fine resolutions is actually a result of the fact that the root-finder used to construct the exact solution has a tolerance of 10^{-9} so relative errors below this level are not reliable.

The convergence behaviour of the standard ADM equations is summarised in figure 6.4 for comparison. We note a couple of important points. Firstly, the ADM formalism crashed well before $t = \pi M$ for those combinations of dt and $d\eta$ for which $dt/d\eta > 1$ (c.f. section 5.2), whereas GEM reached $t = \pi M$ in all cases. This is most likely the same sort of combined Courant and gauge mode instability that we saw in the Minkowski+Noise test case.

Secondly we see that the spatial grid spacing is the dominant factor in the size of the error. We see second order convergence with $d\eta$ using both time-stepping algorithms (the $O(\Delta t^4)$ of the RK(4) is dominated by $O(\Delta x^2)$ spatial derivatives). The convergence (or lack thereof) with dt is completely dominated by the relative error in the grid spacing $d\eta = 0.0075$ which is of the order 10^{-5}. This is highlighted in the bottom graph in figure 6.4. We see that when dt becomes fine enough to lower the error to less than the error caused by the grid spacing, the dt convergence is hindered.

6.4 Maximal Slicing

Due to the limited length of simulations of the Schwarzschild spacetime, geodesic slicing's usefulness is limited to testing the accuracy and convergence of schemes. In order to model realistic astrophysical phenomena, we need to be able to run long-term simulations of black hole spacetimes. If we choose not to excise the physical singularity we must choose a singularity avoiding gauge. One popular choice is maximal slicing, where we impose

$$tr(K) = 0 \tag{6.18}$$

We set this condition on the initial hypersurface, and by enforcing the time derivative of $tr(K)$ to be zero for all time we obtain, through equation (3.96), the following elliptical equation for the lapse function

$$D_a D^a \alpha = \alpha A_{ab} A^{ab} \tag{6.19}$$

which, using equation (4.21) reduces to

$$D_a D^a \alpha = \alpha \left[(\frac{\tilde{A}_1}{\text{I}_1})^2 + 2(\frac{\tilde{A}_2}{\text{I}_2})^2 \right] \tag{6.20}$$

Expanding the left hand side in our coordinates yields

$$\partial_\eta^2 \alpha + \left[\frac{2(\partial_\eta \Psi)}{\Psi} - \frac{(\partial_\eta \text{I}_1)}{2\text{I}_1} + \frac{(\partial_\eta \text{I}_2)}{\text{I}_2} \right] \partial_\eta \alpha - \Psi^4 \text{I}_1 \left[(\frac{\tilde{A}_1}{\text{I}_1})^2 + 2(\frac{\tilde{A}_2}{\text{I}_2})^2 \right] \alpha = 0 \tag{6.21}$$

We implement second order centred differences for the derivatives of α, and require that $\alpha \to 1$ on the outer boundary (i.e. we require asymptotic flatness). Furthermore, α is symmetric about $\eta = 0$, which amounts to the condition $\partial_\eta \alpha|_{\eta=0} = 0$. Equation (6.21) then reduces to a tridiagonal matrix system for the lapse function which we solve this numerically, following the method outlined in Brewin [2002]. Keeping our outer boundary condition constant, we make two initial guesses for the inner ghost-point, $\alpha_{-1}^{(i)}$ † and solve equation (6.21) using a simple Thomas algorithm [Press et al., 1996]. We then make our third and final choice for the inner ghost-point value using a linear combination of the first two guesses, i.e.

$$\frac{\alpha_{-1}^{(1)} - \alpha_{-1}^{(2)}}{[\frac{d\alpha}{d\eta}^{(1)} - \frac{d\alpha}{d\eta}^{(2)}]} = \frac{\alpha_{-1}^{(1)} - \alpha_{-1}^{(3)}}{[\frac{d\alpha}{d\eta}^{(1)} - \frac{d\alpha}{d\eta}^{(3)}]} \tag{6.22}$$

which becomes

$$\alpha_{-1}^{(3)} = \frac{\frac{d\alpha}{d\eta}^{(1)}}{[\frac{d\alpha}{d\eta}^{(1)} - \frac{d\alpha}{d\eta}^{(2)}]} \tag{6.23}$$

where $\frac{d\alpha}{d\eta} \simeq (\alpha_1^{(i)} - \alpha_{-1}^{(i)})/(2\Delta\eta)$. We then make a final calculation using $\alpha_{-1}^{(3)}$ as our inner ghost-point value. We are justified in this method because (6.21) is linear differential equation for α, thus a linear combination of two solutions will automatically be a solution also.

The fact that we must solve an elliptic equation for the lapse on each iteration of the time-stepping algorithm means that maximal slicing is a relatively computationally expensive choice. A possible advantage, however, is that it is a global condition, as opposed to local algebraic conditions such as harmonic slicing. This is potentially

† We require the lapse function to lie between 0 and 1 so we simply choose $\alpha_{-1}^{(1)} = 0$ and $\alpha_{-1}^{(2)} = 1$.

advantageous, as solving the lapse equation will tend to smooth out local oscillations across the grid.

To properly gauge the performance of our code in this slicing we implement three simulations of differing resolutions, but all with $dt/d\eta = 2/3$. We choose

$$\begin{aligned} &dt = 0.01/\rho \\ &nx = 400\rho \implies d\eta = 0.015/\rho \\ &\rho = 1,\ 2,\ 4 \end{aligned} \tag{6.24}$$

Our initial conditions are as given in section 6.2 with the lapse function given by the maximal slicing condition, and the shift vector kept equal to zero throughout the simulation.

In terms of providing long-term integrations of the Schwarzschild spacetime, maximal slicing is somewhat of a double-edged sword. Our observers are initially infalling, but it can be shown [Beig, 2000] that the lapse function on the throat collapses exponentially, via

$$\alpha(\eta = 0) = Ge^{-Ft} + O(e^{-2Ft}) \text{ as } t \to \infty \tag{6.25}$$

where

$$G = \frac{4}{3\sqrt{2}} e^{4H/(3\sqrt{6})} \tag{6.26}$$

$$F = \frac{4}{3\sqrt{6M}} \tag{6.27}$$

$$H = \frac{3\sqrt{6}}{4} \ln\left|18(3\sqrt{2}) - 4)\right| - 2\ln\left|\frac{3\sqrt{3}-5}{9\sqrt{6}-22}\right| \simeq -0.2181 \tag{6.28}$$

and M is the mass of the black hole. Thus the coordinate time becomes "frozen" on the inner boundary. Thus, although our coordinates are able to cover a portion of the manifold interior to the event horizon, our observers will never hit the physical singularity as in, for example, geodesic slicing

This does not mean we are able to run simulations for an infinite time though. As the interior of the grid becomes frozen whilst the exterior portion is still infalling, large gradients develop in all our metric functions, and hence all our evolution variables. The steep gradients that form in this transition region will eventually be the death of most codes, especially those that implement simple numerical methods, such as ours. This is because standard finite difference techniques implemented on a fixed grid struggle to resolve the coordinate shocks that develop, resulting in runaway numerical noise in the transition region.

This behaviour is illustrated in figures 6.5 and 6.6 which present the evolution of the GEM variables for the "Standard" resolution case ($\rho = 2$). We output the variables every $5M$ until $t = 60M$. It is shortly after this that the error growth becomes unbounded and the code becomes unstable. The results we present here were obtained with the iterative Crank-Nicholson integrator, but similar results were found with Runge-Kutta

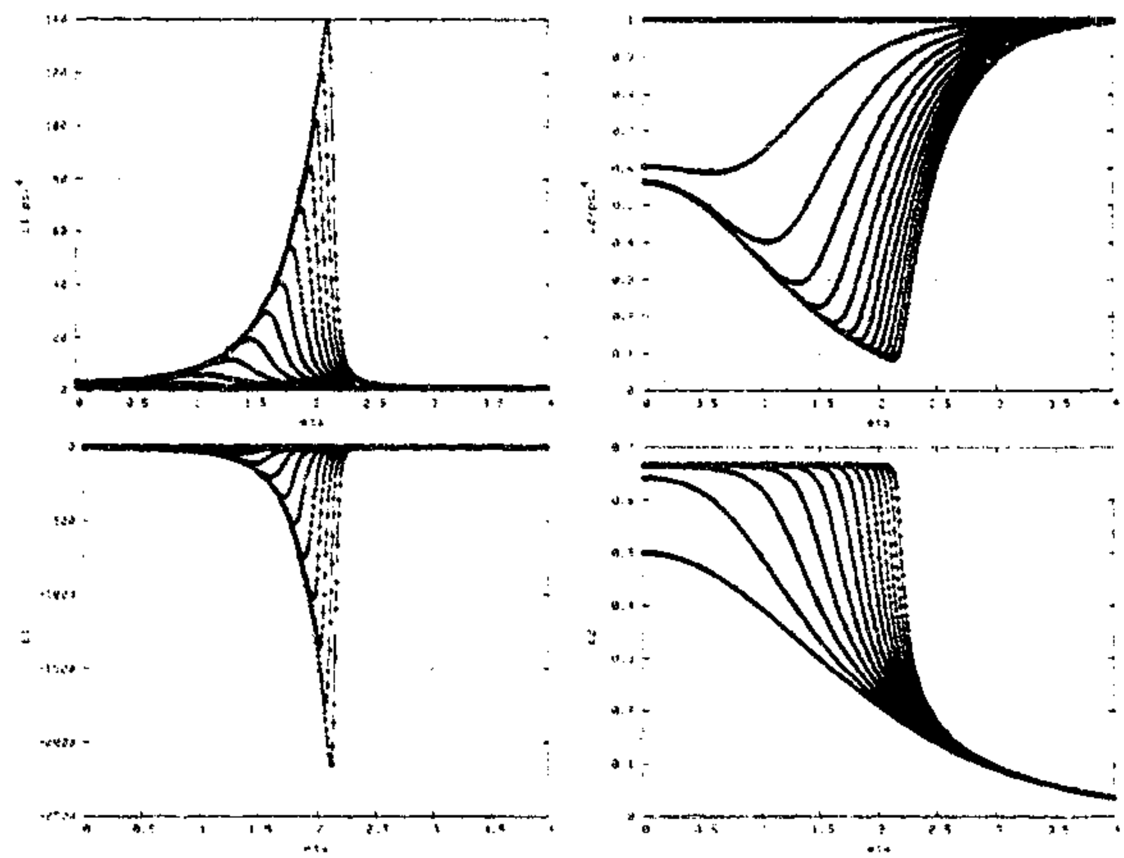

Figure 6.5: *GEM evolution variables for maximal slicing : metric on line 1, gravito-electric tensor on line 2. All variables are outputted as a function of η every $t = 5M$ from $t = 0M$ to $t = 60M$. The resolution is "standard" ($p = 2$). The steep gradients cause the code to crash shortly after this point.*

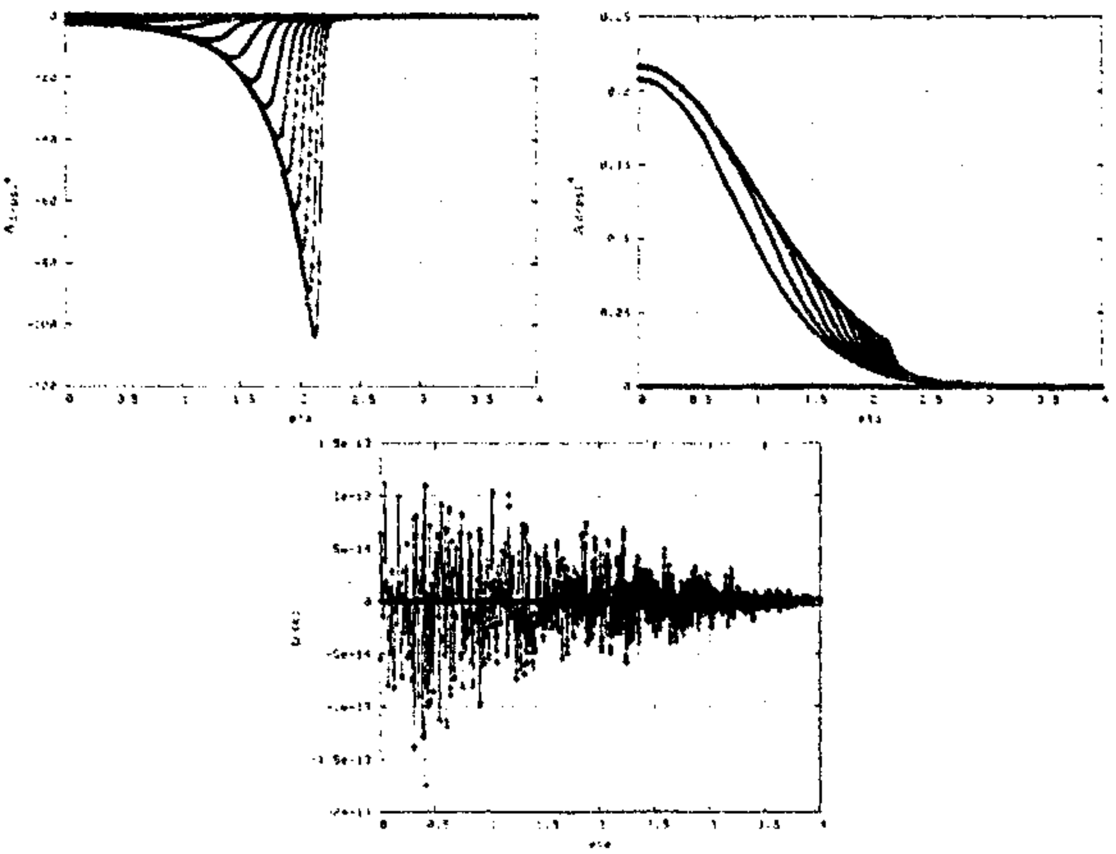

Figure 6.6: *GEM evolution variables for maximal slicing : trace-free part of the extrinsic curvature on line 1 and the trace of the extrinsic curvature on bottom line. All variables are output as a function of η every $t = 5M$ from $t = 0M$ to $t = 60M$. The resolution is "standard" ($\rho = 2$). The steep gradients cause the code to crash shortly after this point.*

(though the RK(4) code was stable for slightly longer).

We see clearly the steep gradients forming well before $60M$. The worst case of this is E_1, whose values vary by three orders of magnitude across the grid. Note also that at $t = 60M$ the transition region is covered by only about 20 grid points, out of the 800 that cover the grid. Because we have no shift vector and do not have to compute the 3-Ricci tensor directly, there there is no error caused by having to compute second derivatives over the transition region. However, the large differences in scale in our variables across the grid will still cause round-off error to be an issue. Also, the resolution of the first order spatial derivatives becomes almost impossible with such poor resolution.

The ADM code runs for longer than the GEM code in this configuration. Figure 6.7 shows the evolution of the metric in the ADM formalism. The ADM code, whilst exhibiting similar behaviour to the GEM code, is stable until about $t = 110M$ (for thestandard resolution, $\rho = 2$). As both methods reproduce the expected qualitative behaviour, it is not trivial to ascertain the reason that GEM performs worse in this case. By comparing figures 6.5 and 6.7 we can see that the peak in E_1 is much more severe than the peak that develops in R_1 in the ADM case (note that the plots in figure 6.7 show data for $40M$ longer than figure 6.5).

To get a handle on what is happening here we consider the growth of the errors throughout the simulation. We consider the collapse of the lapse on the throat, for all three resolutions and for both formalisms, in figure 6.8. We use the analytic expression given by equation (6.25) for comparison.

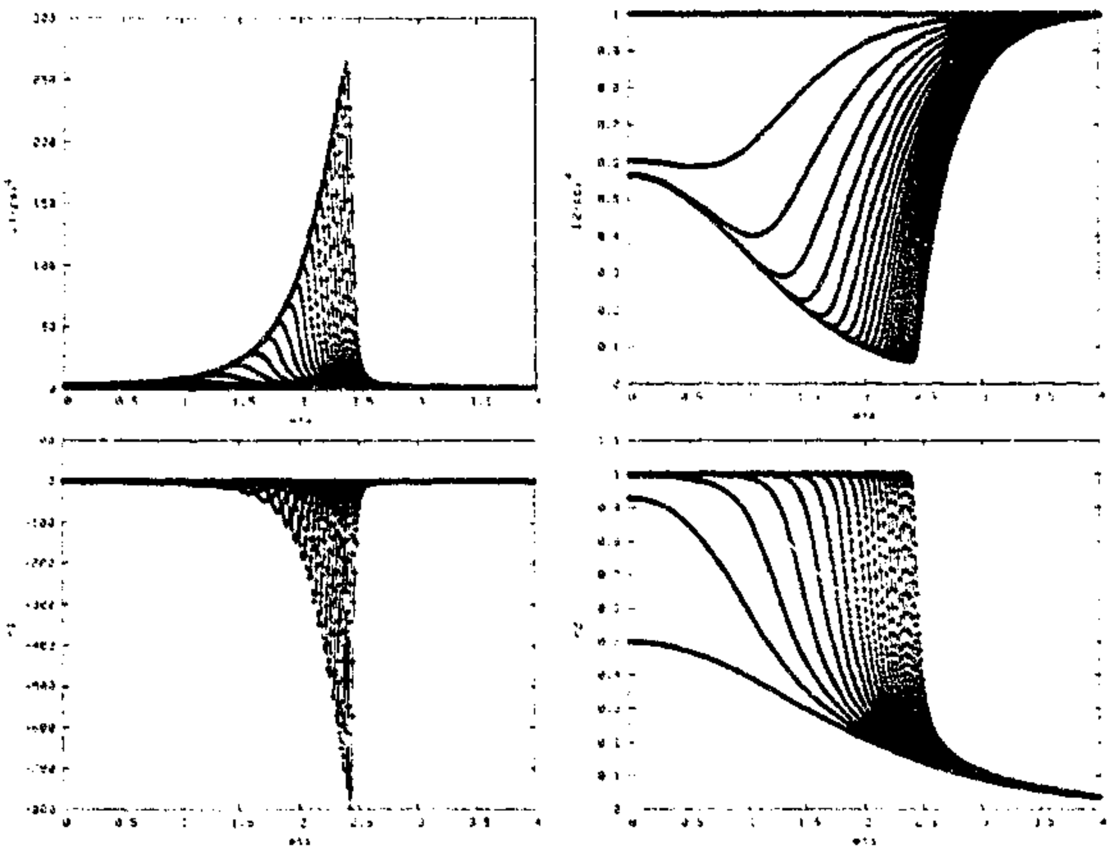

Figure 6.7: *Evolution of the ADM metric functions in maximal slicing. All variables are outputted as a function of η every $t = 5M$ from $t = 0M$ to $t = 100M$. The resolution is "standard" ($\rho = 2$). The steep gradients cause the code to crash at around $t = 110M$*

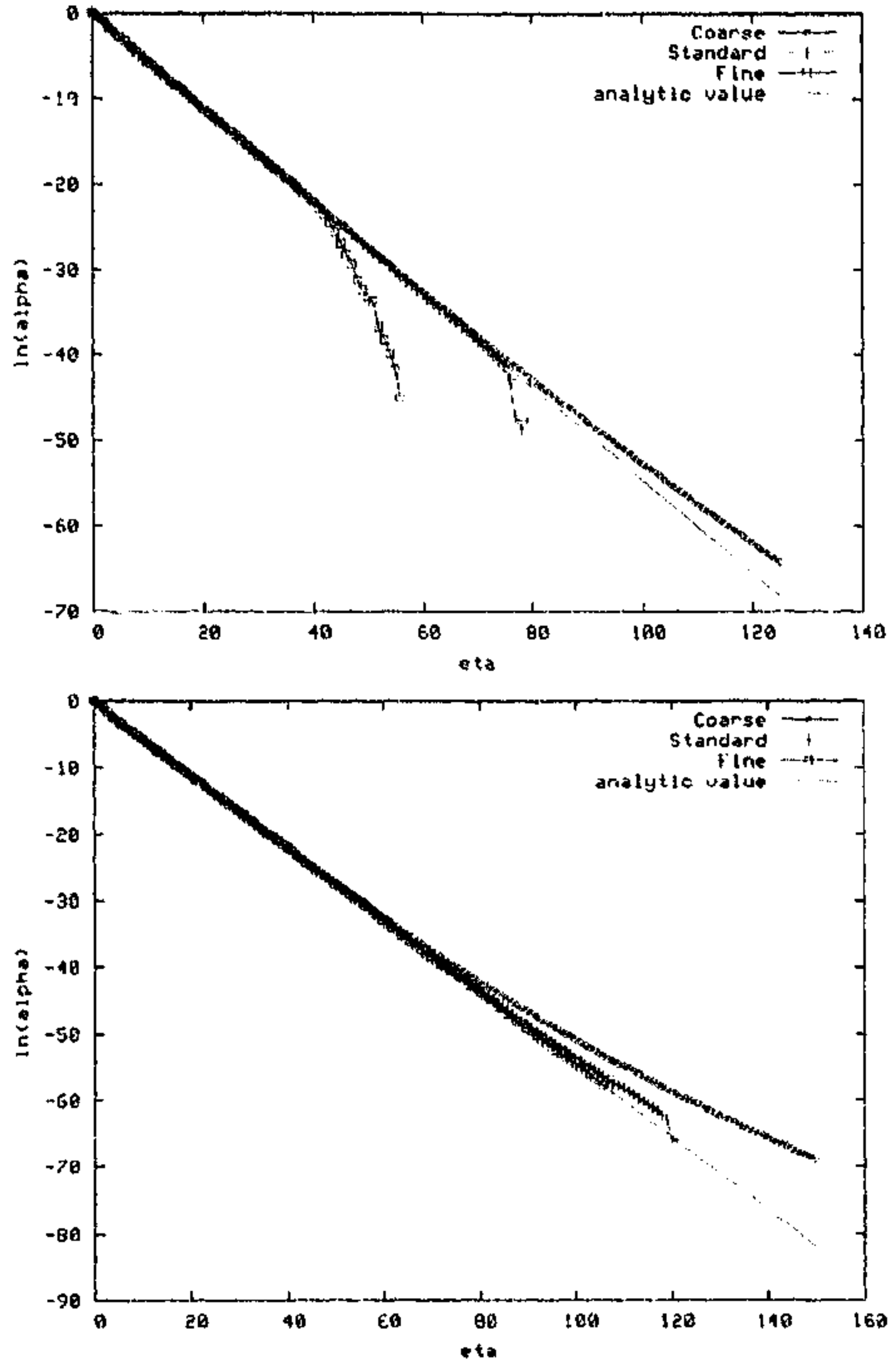

Figure 6.8: *The collapse of the lapse as a function of time for three resolutions, compared to the analytical solution (equation (6.25)). GEM is on the top, ADM on the bottom. All runs used CrN(2) time-stepping and resolutions as given by equation (6.24). All runs were timed to end at $t = 150M$ (though not all made it that far!)*

Firstly we note that the coarser the grid, the longer the evolution lasted, for both formalisms. We note that all resolutions give reasonably accurate results (until the runaway errors dominate). The coarsest grid resolution leads to deviation from the analytical solution at late times, with ADM being less accurate than GEM in this case. This loss of accuracy is not unexpected for long integrations on coarser grids, due to the lower resolution. The same sort of thing is discussed in section 5.3, where the coarser grids exhibited growing inaccuracies with time. It is interesting that the lapse is collapsing more slowly than expected. This would tend to lead to a slower formation of the steep gradients in the transition region and, presumably, a longer lived simulation.

Although we have no exact solution to compare with in the maximal slicing case, the violation of the constraints can be used to gauge the accuracy and convergence of our code. We plot the average value of the Hamiltonian and momentum constraints at each time-step (figures 6.9 and 6.10). Both sets of equations show convergent behaviour at first but the convergence is destroyed once the codes are no longer able to accurately resolve the gauge dynamics.

Again, figures 6.9 and 6.10 shows that the development of the steep gradients and the violation of the constraints is exacerbated by better resolution, indicating a true gauge instability rather than an code inaccuracy. Both formalisms violate the constraints by a similar amount at early times, indicating again that the poorer performance of GEM does not arise from a low accuracy simulation, or an unstable formalism. Rather the difficulty in following the gauge dynamics, especially the coordinate shocks, appear to be the biggest factor in the performance of both formalisms in this particular case.

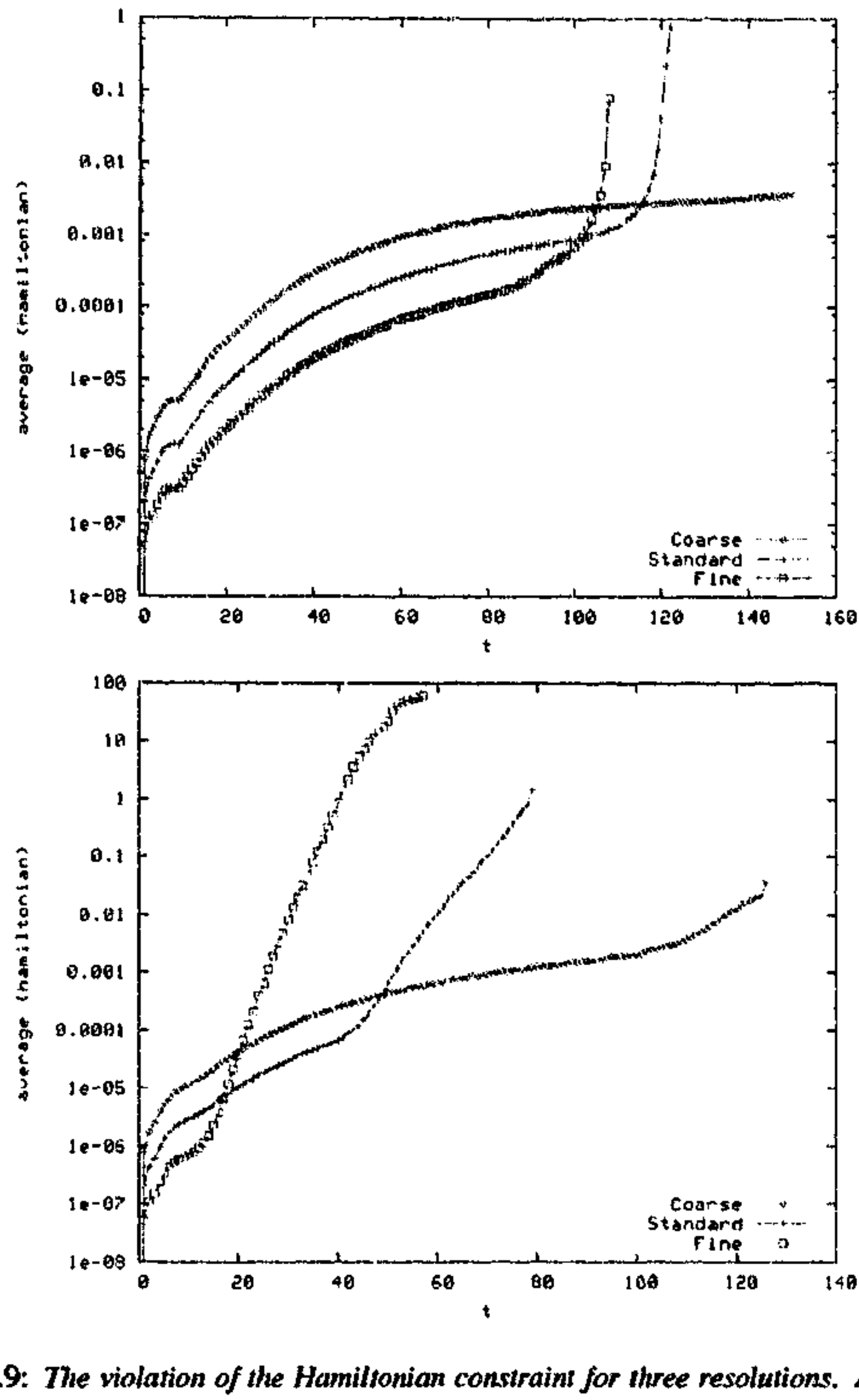

Figure 6.9: *The violation of the Hamiltonian constraint for three resolutions. ADM is on the top, GEM on the bottom. All runs used CrN(2) time-stepping and resolutions as given by equation (6.24). All runs were timed to end at $t = 150M$ (though not all made it that far!)*

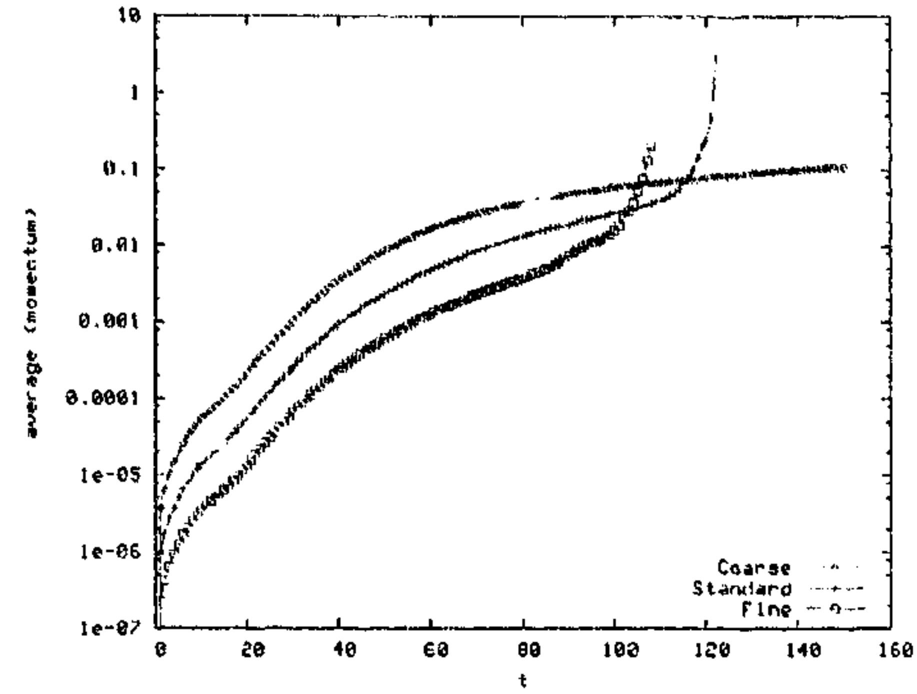

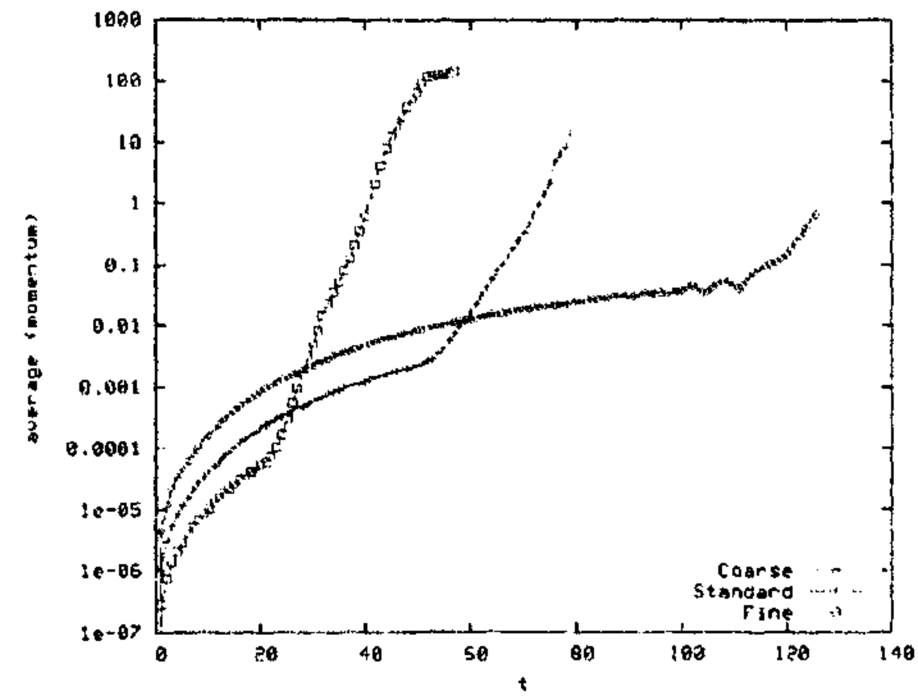

Figure 6.10: *The violation of the momentum constraint for three resolutions. ADM is on the top, GEM on the bottom. All runs used CrN(2) time-stepping and resolutions as given by equation (6.24). All runs were timed to end at $t = 150M$ (though not all made it that far!)*

6.5 1+ln Slicing

We can also utilise the Bona-Masso family of slicing conditions (equation (5.3)) in the Schwarzschild spacetime. Harmonic slicing is not appropriate in this case as the lapse does not collapse fast enough on the throat and the singularity is reached in finite time [Bernstein, 1993]. However, we can choose $f(\alpha) = 1/\alpha$ in equation (5.3), leading to what is commonly called 1+log, or 1+ln slicing. The evolution of the lapse is prescribed by

$$\partial_t \alpha = -\alpha tr(K) \tag{6.29}$$

which integrates to become $\alpha = 1 + \ln(\sqrt{\det(\perp)})$, hence the name. We also require that the shift vector be identically equal to zero. The rest of the variables are initialised as in section 6.2.

Like the maximal slicing condition, the 1+ln gauge choice has both advantages and disadvantages. A major advantage is in efficiency, as solving equation (6.29) is much more computationally efficient than solving equation (6.21). Although this is not a major issue in 1D, it is worth keeping in mind, as it will become an issue in higher dimensions.

In terms of dynamics, 1+ln slicing is qualitatively similar to maximal slicing. Both have singularity avoiding properties, with the lapse collapsing to zero on the inner boundary. This leads to steep gradients forming in the transition region between the frozen and infalling parts of the grid. As in the maximal slicing case, the steep gradients and loss of resolution in this region will tend to destroy the accuracy and/or stability of the code over time.

We conducted the simulations using the same computational parameters as in the previous section. In particular we ran the tests at three different resolutions, as specified by (6.24). We found our GEM code performed better in this gauge than in maximal slicing, with each resolution running for approximately twice as long as its maximal slicing counterpart. Again, Crank-Nicholson(2) and Runge-Kutta(4) performed similarly. The evolution of the key variables for the $\rho = 2$ standard resolution are given in figures 6.11 and 6.12. Note these results extend to $t = 120M$, an improvement over the maximal slicing case (where, for $\rho = 1$ the GEM code crashed by about $t = 80M$).

As in the previous section, we again note the growth of the radial component of the metric and gravito-electric tensor (figure 6.11). Both these components are only starting to show spiking on the transition region at $t = 120M$ where we note, for example, that $\tilde{\mathcal{I}}_1$ has grown by 750% from its original value and the transition region is covered by only about 10 grid points. Note also that $tr(K)$ is not zero in this gauge (figure 6.12).

Again we see that ADM seems to out-perform GEM in this gauge, in terms of following the evolution for longer. For all resolutions, the ADM code ran to $t = 150M$ (when we terminated the run). The cause of this is indicated in figure 6.13 where we see that the coordinate shocks in the ADM evolution variables to not become as steep as in the GEM case.

This is not all good news for ADM though. Figures 6.14 and 6.15 demonstrate the convergence of the constraints with resolution. Although there is no exact solution

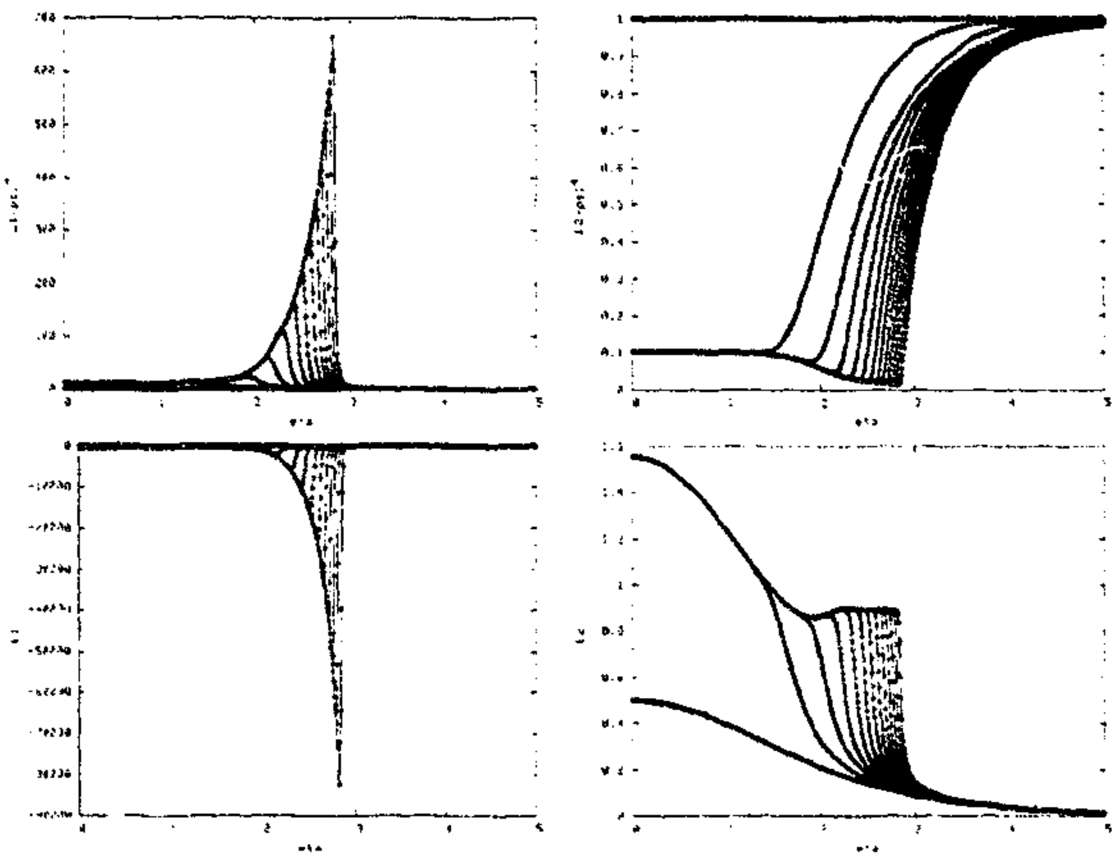

Figure 6.11: *GEM evolution variables for 1+ln slicing : metric on line 1, gravito-electric tensor on line 2. All variables are outputted as a function of η every $t = 10M$ from $t = 0M$ to $t = 120M$. The resolution is "standard" ($\rho = 2$). The steep gradients cause the code to crash shortly after this point.*

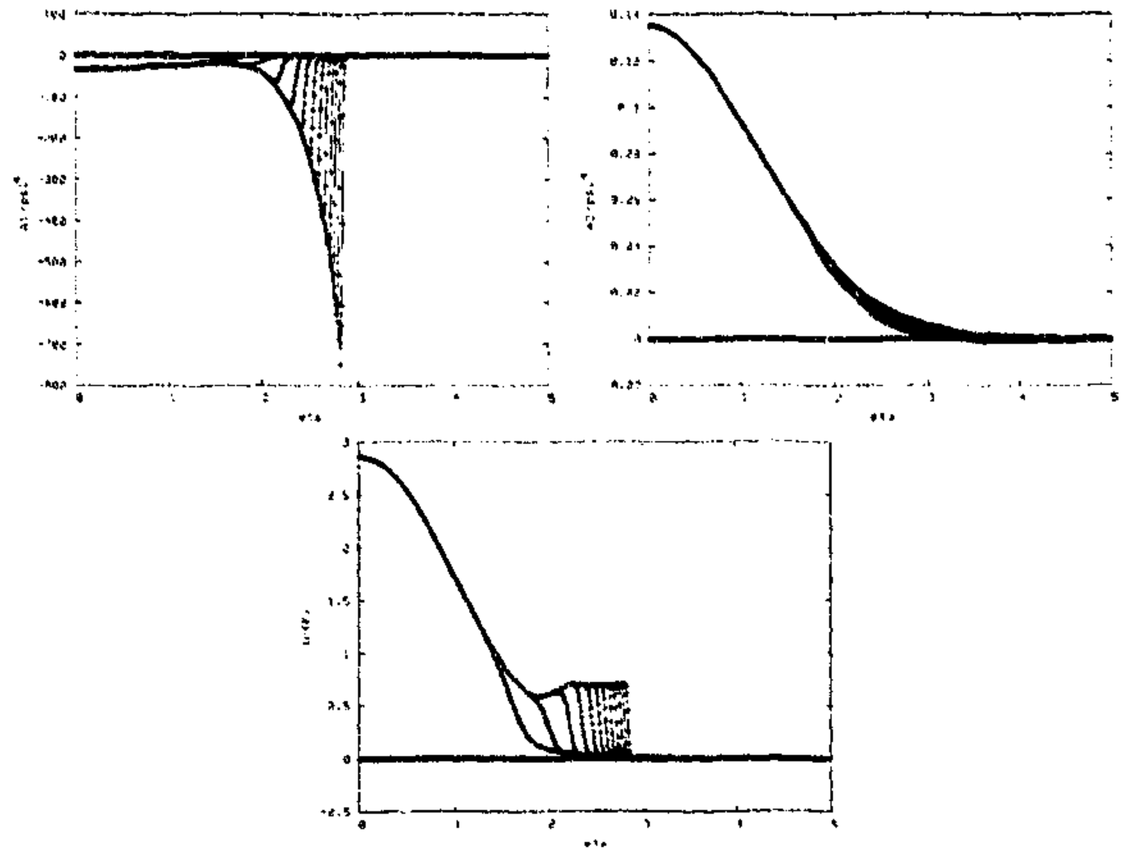

Figure 6.12: *GEM evolution variables for 1+ln slicing: trace-free part of the extrinsic curvature on line one and the trace of the extrinsic curvature on bottom line. All variables are outputted as a function of η every t = 10M from t = 0M to t = 120M. The resolution is "standard" ($\rho = 2$). The steep gradients cause the code to crash shortly after this point.*

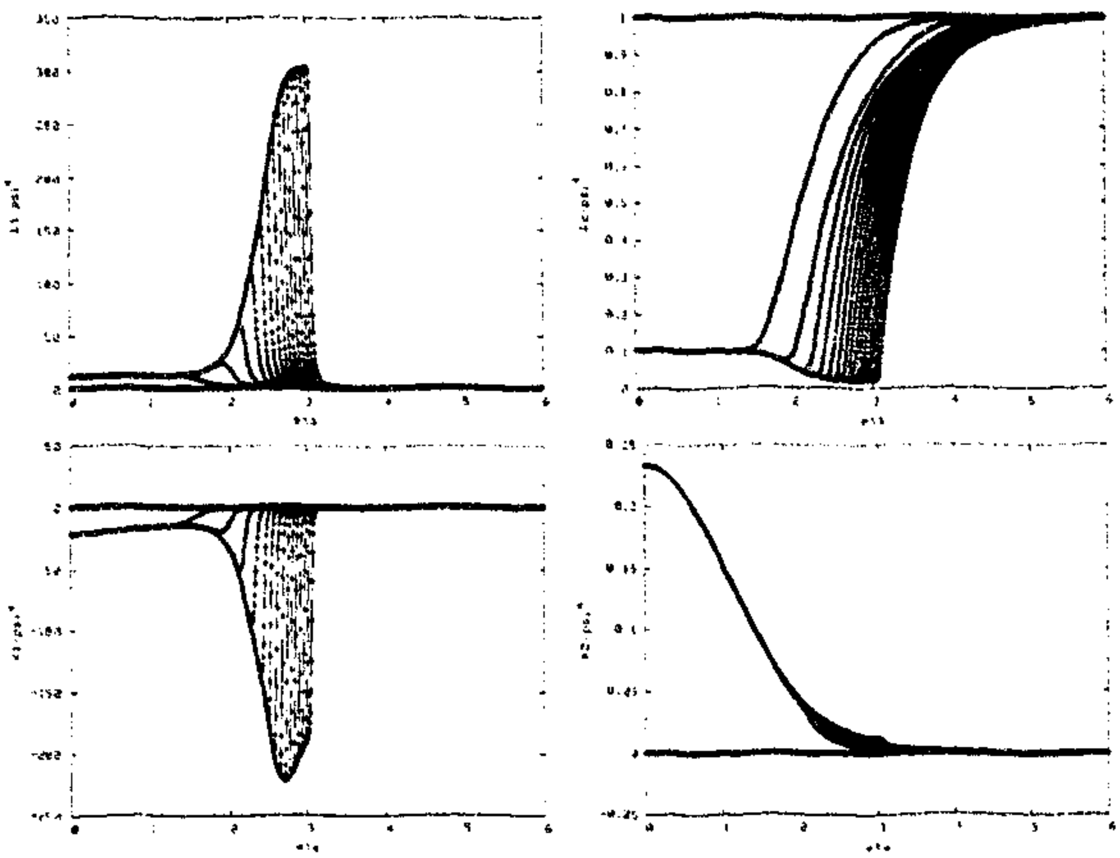

Figure 6.13: *ADM evolution variables for 1+ln slicing : metric on line 1, extrinsic curvature tensor on line 2. All variables are outputted as a function of η every $t = 10M$ from $t = 0M$ to $t = 150M$. The resolution is "standard" ($\rho = 2$). The steep gradients cause the code to crash shortly after this point.*

available in this gauge, we can use the violation of the constraints to gauge the convergence of a formalism to the "correct" solution. We use equation (5.11) to calculate the convergence factor σ using the Hamiltonian and momentum constraints. The GEM equations are convergent until about 40-50M, which corresponds to the time at which errors in the finest grid resolution become unbounded. Therefore the behaviour of σ after this time indicates the loss of accuracy involved in trying to resolve the worsening coordinate shock, rather than saying anything meaningful about the convergence properties of the GEM equations.

The ADM simulations all run to 150M for all resolutions, but we clearly see that the convergence of the constraints is destroyed after about 30M. Note also that the convergence behaviour for both schemes (but in particular ADM) is unaffected by the choice of time integrator. Both schemes use simple second-order centred differences for the spatial derivatives and it is this that dominates both the error and the convergence of the overall scheme. This suggests that the lack of convergence in the ADM case is due to the inability of the spatial differencing to approximate the first and, in particular, the second order derivatives. This, in turn, implies that the longer integration time achieved with the ADM equations is gained at the expense of accuracy.

The fact that GEM does not exhibit this behaviour, then, is due to the fact that the GEM equations are first order in both space and time. Because we have replaced the 3-Ricci tensor in the GEM evolution equations we do not have the additional complication of evaluating accurate second-order spatial derivatives on the steep gradients in the transition region of the grid. We surmise that although the GEM simulations were relatively short-lived, they appear to achieve a higher level of accuracy than the

ADM equations in this slicing.

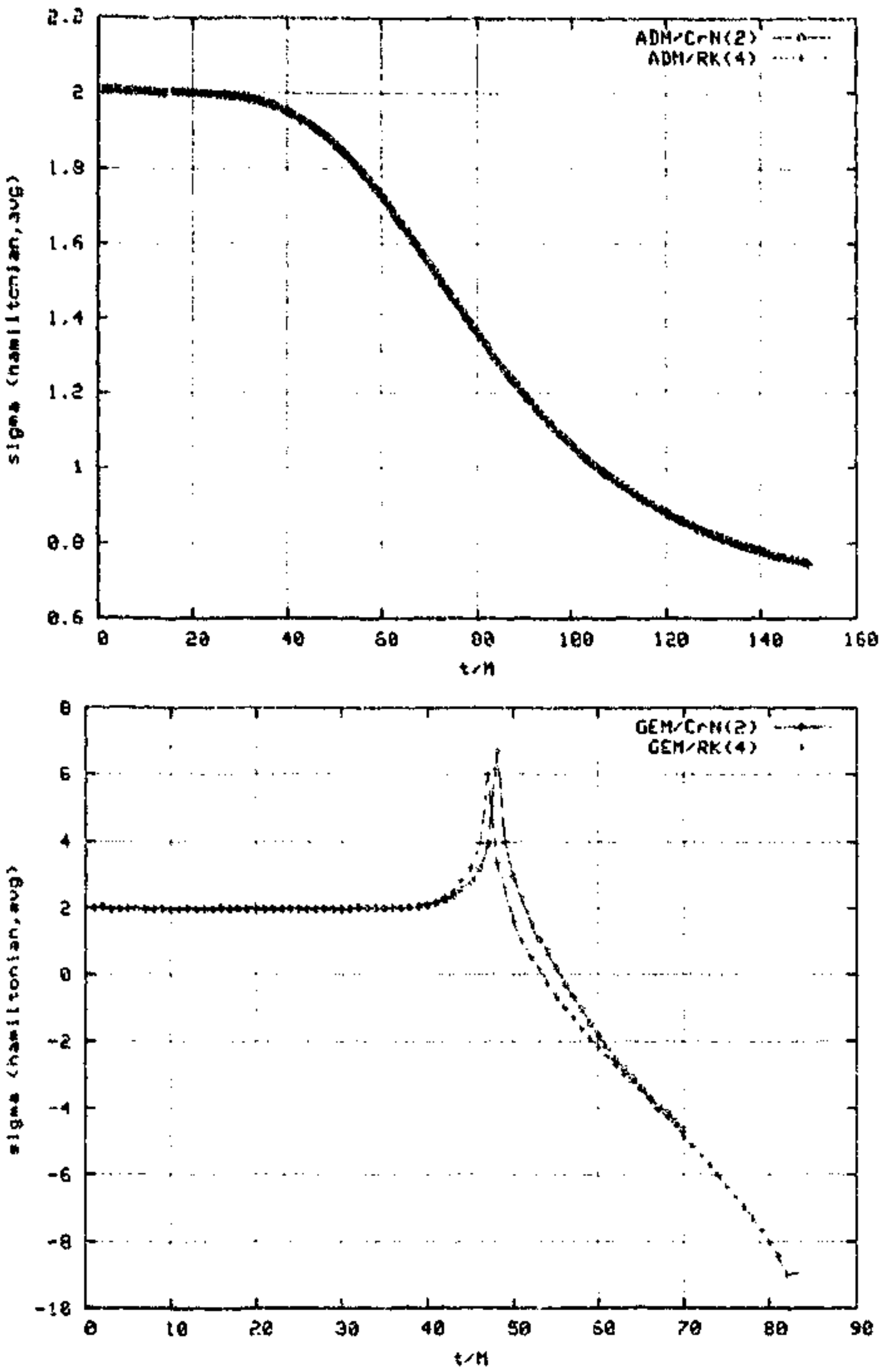

Figure 6.14: *Convergence of the Hamiltonian constraints for ADM (top) and GEM (bottom) equations in 1+ln slicing.*

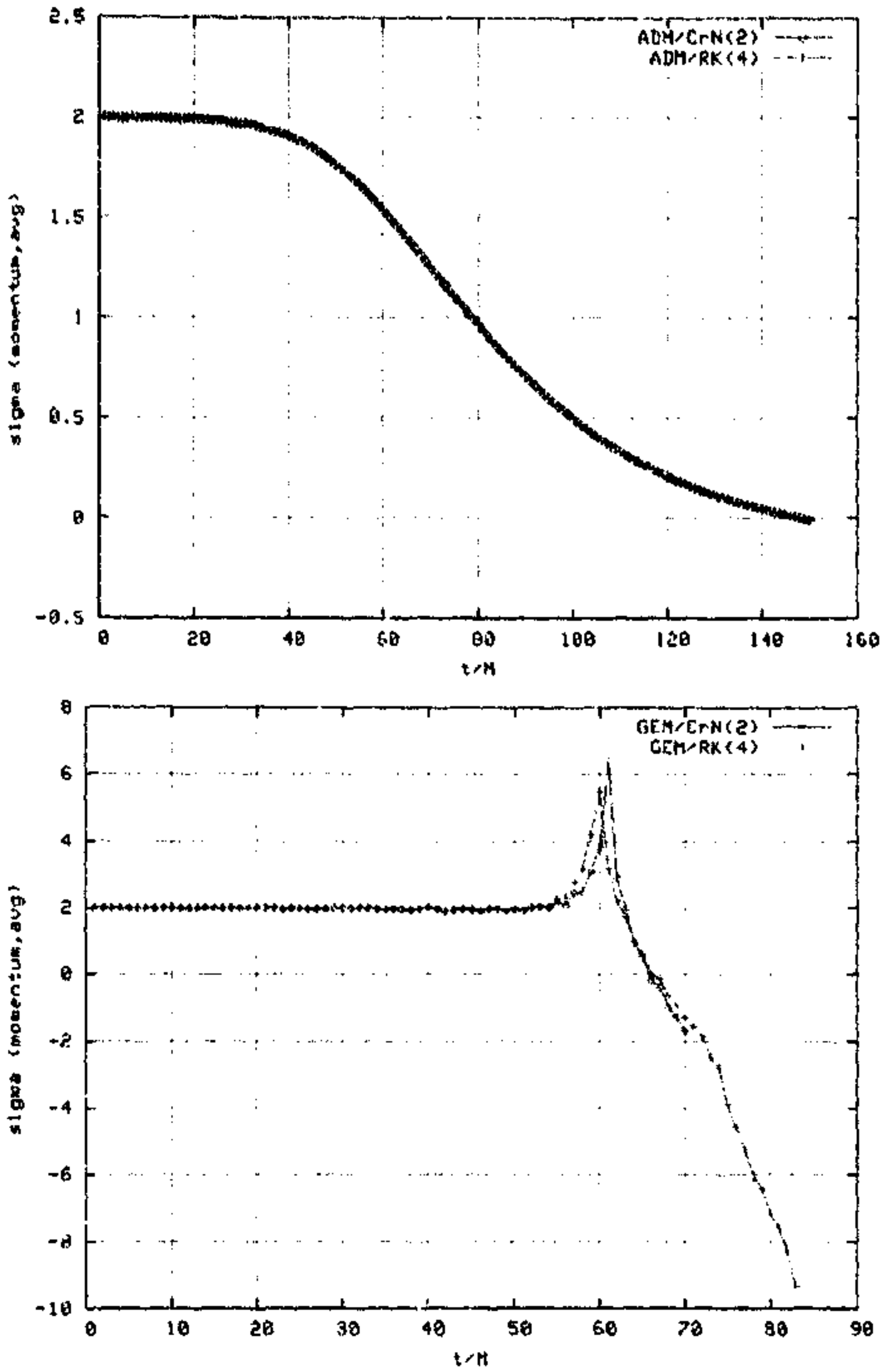

Figure 6.15: *Convergence of the momentum constraint for ADM (top) and GEM (bottom) equations in 1+ln slicing.*

Chapter 7

A Shift Vector Slicing

One of the fundamental difficulties in modelling the Schwarzschild spacetime is the appearance of coordinate shocks when singularity avoiding slicings are used. Traditional finite difference methods will always struggle to resolve these shocks regardless of which 3+1 equations are used, which goes some way to explaining the dearth of long-lived evolutions of Schwarzschild in the maximal or 1+log family of slicing conditions. One successful evolution is described in Alcubierre et al. [2003b]. They utilise the BSSN formalism coupled to a K-driver condition for the lapse function, based on maximal slicing and the so-called Gamma-driver condition for the shift vector [Balakrishna et al., 1996] .

Another stable evolution was obtained by Brewin [2002] by using maximal slicing, and no shift vector. The numerical technique was based on the smoothed lattice approach [Brewin, 1998b][Brewin, 1998a]. Rather then using the 3-metric, this method utilises the leg-lengths of the lattice to calculate curvature. Although this approach uses ideas and notation from the Eulerian ADM approach, it is fundamentally Lagrangian in implementation. This contributes to the stable evolution, as the lattice is able to stretch with the motion of the spacetime, which eliminates the gauge-shocks seen in finite difference approaches.

In this chapter we aim to ascertain whether we can use our 3+1 approach, coupled with an appropriate shift vector to mimic the result of Brewin [2002]. That is, can we remove the gauge instabilities that plague the evolutions using both the ADM and GEM equations by a prudent choice of shift vector?

To do this we implement a "radial distance locking" gauge choice (c.f. area locking gauge as examined in Kelly et al. [2001]). We use the gauge freedom to keep the radial metric function constant at its initial value throughout the evolution. The motivation to try to reduce the spiking seen in singularity avoiding slicing such as maximal and 1+ln slicing.

We must first cast the spatial metric into a form more suited to our needs through a change of variables from the (t, η, θ, ϕ) of the previous chapter, to a new system with a modified radial coordinate. We restrict the radial component of the 3-metric to be unity, thus imposing a constant radial resolution.*

*As opposed to the coordinates used in the previous chapter, in which the resolution decreased as a function of proper spatial distance

7.1 A Coordinate Transformation

We start with the spatial metric taken from equation (6.3), i.e.

$$dl^2 = [\sqrt{2M}\cosh(\eta/2)]^4[d\eta^2 + d\theta^2 + \sin^2\theta d\phi^2] \tag{7.1}$$

and implement the change to a new coordinate system, $[t, \bar{\eta}, \theta, \phi]$ via the transformation

$$d\bar{\eta} = [\sqrt{2M}\cosh(\eta/2)]^2 d\eta \tag{7.2}$$

which implies

$$\bar{\eta}/M = 2(\eta + \sinh(\eta)) \tag{7.3}$$

As the Schwarzschild spacetime is spherically symmetric, only the radial coordinate was transformed.

The 3+1 line-element in the new coordinates is given by:

$$ds^2 = -(\alpha^2 - \beta^i\beta_i)dt^2 + \beta_i dx^i dt + d\bar{\eta}^2 + f(\eta)(d\theta^2 + \sin^2\theta d\phi^2) \tag{7.4}$$

where $f(\eta) = [\sqrt{2M}\cosh(\eta/2)]^4$ and η is obtained by solving equation (7.2). We cannot solve for η analytically, but obtain a numerical solution of a chosen tolerance. This metric is related to that mentioned in Alcubierre [1997], though that work involved a transformation from isotropic coordinates.

The relationship of the modified radial coordinate to the radial coordinate used in the preceding chapter and to the Schwarzschild radial coordinate is outlined in figure

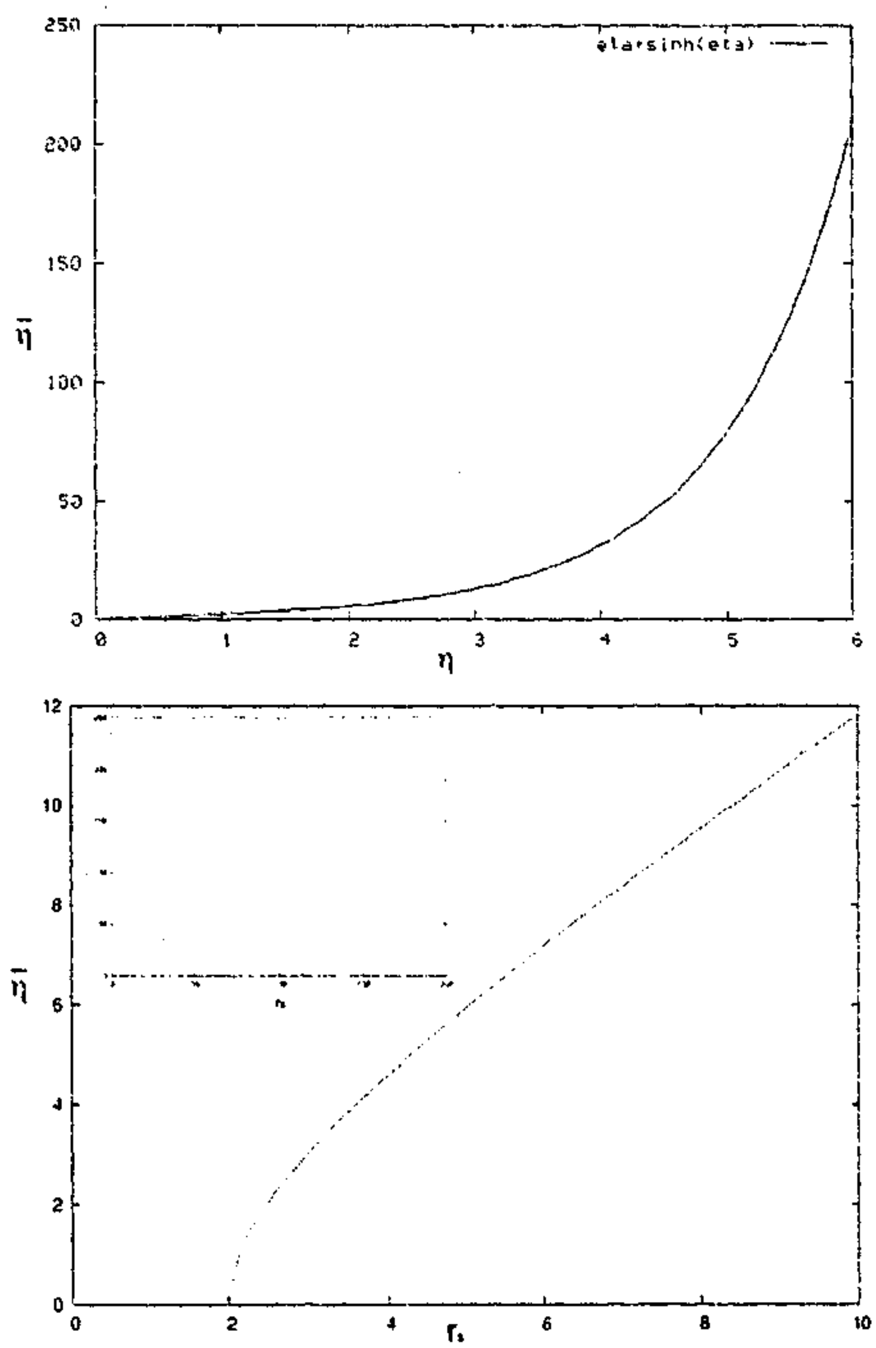

Figure 7.1: *Comparison of η and $\bar{\eta}$ coordinates (top). Comparison of Schwarzschild (r_s) and $\bar{\eta}$ coordinates (bottom). The inset shows the large-scale behaviour of the coordinate.*

7.1. The first thing to note is that the original η coordinate grows exponentially as a function of $\tilde{\eta}$. Thus, we need $\tilde{\eta} \in [0, 200)$ to model the spacetime covered by $\eta \in [0, 6)$ and we will have significantly less resolution in the inner region. However, as the horizon moves outward in, for instance, maximal slicing, the number of grid points covering the 'transition' region will remain constant, not decrease as in the η case. This should help alleviate some of the spiking behaviour seen in the previous chapter. We also have from figure 7.1, or perhaps more clearly from equation (7.2) that $\tilde{\eta} = 0$ when $\eta = 0$, so the position of the isometry surface has not changed. This means we can implement simple inner boundary conditions, as in the previous chapter.

The relationship to the Schwarzschild radial coordinate (r_s) is also interesting. Whilst the relationship is almost linear on a large scale, we see that $\tilde{\eta}$ decreases to zero as r_s approaches $2M$. Thus this coordinate system is very similar to standard Schwarzschild coordinates, with the added bonus of being regular everywhere.

The initial conditions are set as follows:

- $\tilde{\eta} \in [0, 200)$, solve for $\eta(\tilde{\eta})$ using (7.2) and a standard bisection root-finder algorithm [Press et al., 1996].
- $\Psi = 1$
- $\perp_1 = 1$, $\perp_2 = [\sqrt{2M}\cosh(\eta/2)]^4$
- $K_1 = K_2 = A_1 = A_2 = tr(K) = 0$, i.e. a time-symmetric initial slice.
- ${}^{(3)}R_1 = {}^{(3)}Q_1 = -2/(1 + \cosh(\eta))^3$

$$^{(3)}R_2 = {}^{(3)}Q_2 = 1/(1+\cosh(\eta))$$
$$^{(3)}R = 0$$

- $E_1 = {}^{(3)}Q_1$, $E_2 = {}^{(3)}Q_2$, using the constraint equation (3.93)

The fact that the η and $\bar{\eta}$ coordinates have the same isometry behaviour allows us to implement the inner boundary conditions outlined in section 6.2. The outer boundaries were treated in the same way as in section 6.2 also. It was found that the quadratic fitting function (equation (6.5)) gave more accurate results then the exponential function (6.4) in approximating the outer value of $\perp_2$, which grows almost quadratically with $\bar{\eta}$.

We wish to keep the metric in the form of (7.4) and in particular we wish to keep the radial metric component equal to one which necessitates the use of a non-zero shift vector.

7.2 Radial Distance Locking Shift Vector

In order to keep $\perp_{\bar{\eta}\bar{\eta}} \equiv \perp_1 = 1$ throughout the simulation we need to enforce the condition $\partial_t \perp_1 = 0$. From spherical symmetry we assume the shift vector has the form

$$\beta^i = (\beta^1, 0, 0) \tag{7.5}$$

Inspection of the equation for the time derivative of the metric (equation (4.17)) yields the following condition on the shift vector

$$\partial_{\bar\eta}\beta^1 = -2\alpha(A_1 + \frac{1}{3} \perp_1 tr(K)) \qquad (7.6)$$

To solve this first order differential equation we apply the boundary condition $\beta^1(\bar\eta = 0) = 0$ which ensures that the shift vector vanishes on the throat and removes the need for complicated inner boundary conditions on our other evolution variables.

We solve equation (7.6) using a shooting method based on that used to solve for the lapse in maximal slicing (section 6.4). The same principles hold as equation (7.6) is linear in β^1. We make two separate guesses for β^1 on the outer boundary (${}^{(i)}\beta^1_{out}$) and integrate in to the inner boundary using a standard second order predictor-corrector. The third and final guess for the outer boundary value of the shift is constructed from

$$\frac{{}^{(1)}\beta^1_{out} - {}^{(2)}\beta^1_{out}}{{}^{(1)}\beta^1_{in} - {}^{(2)}\beta^1_{in}} = \frac{{}^{(1)}\beta^1_{out} - {}^{(3)}\beta^1_{out}}{{}^{(1)}\beta^1_{in} - {}^{(3)}\beta^1_{in}} \qquad (7.7)$$

which becomes

$${}^{(3)}\beta^1_{out} = \frac{{}^{(1)}\beta^1_{in}}{{}^{(2)}\beta^1_{in} - {}^{(1)}\beta^1_{in}} \qquad (7.8)$$

For the following simulations we implement the radial distance locking shift and maximal slicing lapse function (see section 6.4). The addition of a non-zero shift vector gives the 1D evolution equations (for both ADM and GEM) the form of advection equations, i.e. all the evolution equations have the form

$$\partial_t \mathcal{U} = \beta^1 \partial_{\tilde{\eta}} \mathcal{U} + g(\mathcal{U}) \tag{7.9}$$

where $\mathcal{U}$ is the vector of evolution variables and g is a non-linear function of the evolution variables. The derivative in the advective term is calculated using an upwind difference method, as implemented in Kelly et al. [2001], i.e.

$$\partial_{\tilde{\eta}} w_i \approx \frac{w_{i+1} - w_{i-1}}{2\Delta\tilde{\eta}} \pm q\left(\frac{w_{i\mp1} - 3w_i + 3w_{i\pm1} - w_{i\mp2}}{3\Delta\tilde{\eta}}\right) \tag{7.10}$$

where $\pm$ is chosen to correspond to the sign of the shift vector (always negative, in this case) and q is an arbitrary constant which must satisfy $q \geqslant 0$. Furthermore, Kelly et al. [2001] show that the discretisation error associated with (7.10) is

$$\mathrm{err}(\partial_{\tilde{\eta}} w_i) = \frac{1}{6}(1 - 2q)\Delta\tilde{\eta}^2 \partial_{\tilde{\eta}}^3 u_i \mp \frac{q}{6}\Delta\tilde{\eta}^3 \partial_{\tilde{\eta}}^4 u_i \tag{7.11}$$

We see from this that the truncation error is best ($O(\Delta\tilde{\eta}^3)$) when q=0.5. Thus, this is the choice we make here. All other derivatives are estimated by second-order centred differences.

7.3 Results

The GEM and ADM codes were run with the following grid resolutions:

$$\bar{\eta}_{inner} = 0M \quad \bar{\eta}_{outer} = 200M \tag{7.12}$$

$$dt = 0.02/\rho$$

$$\text{no. grid points} = 2000\rho \implies d\bar{\eta} = 0.01/\rho \tag{7.13}$$

$$\rho = 1,\ 2,\ 4$$

Figures 7.2 and 7.3 show the qualitative behaviour of the GEM evolution variables with time, and figures 7.4 and 7.5 show the same for the ADM variables. We show the results for the Standard resolution ($\rho = 2$) case.

We see from both sets of results the advantages in this gauge. The effect of the shift vector is to "pull in" observers from the outer region, giving constant resolution over the transition from the frozen inner grid to the dynamical outer grid. We see the volume element (indicated by $\perp_2$) growing with radial distance from the throat. As the integration progresses, however, the value of $\perp_2$ on the outer grid decreases, indicating that these observers are infalling.[†]

Although $\perp_1$ is required to be 1, we allow it to evolve freely, as an additional constraint. We see that $\perp_1 \approx 1$ throughout the evolutions. We also see that the values of the extrinsic curvature terms remain bounded, and $tr(K)$ remains very close to zero

[†]To be precise, in the Eulerian reference frame of the calculation, the observers aren't "pulled" or infalling at all, rather they remain at constant spatial coordinates and the inner portion of the space is falling out toward them.

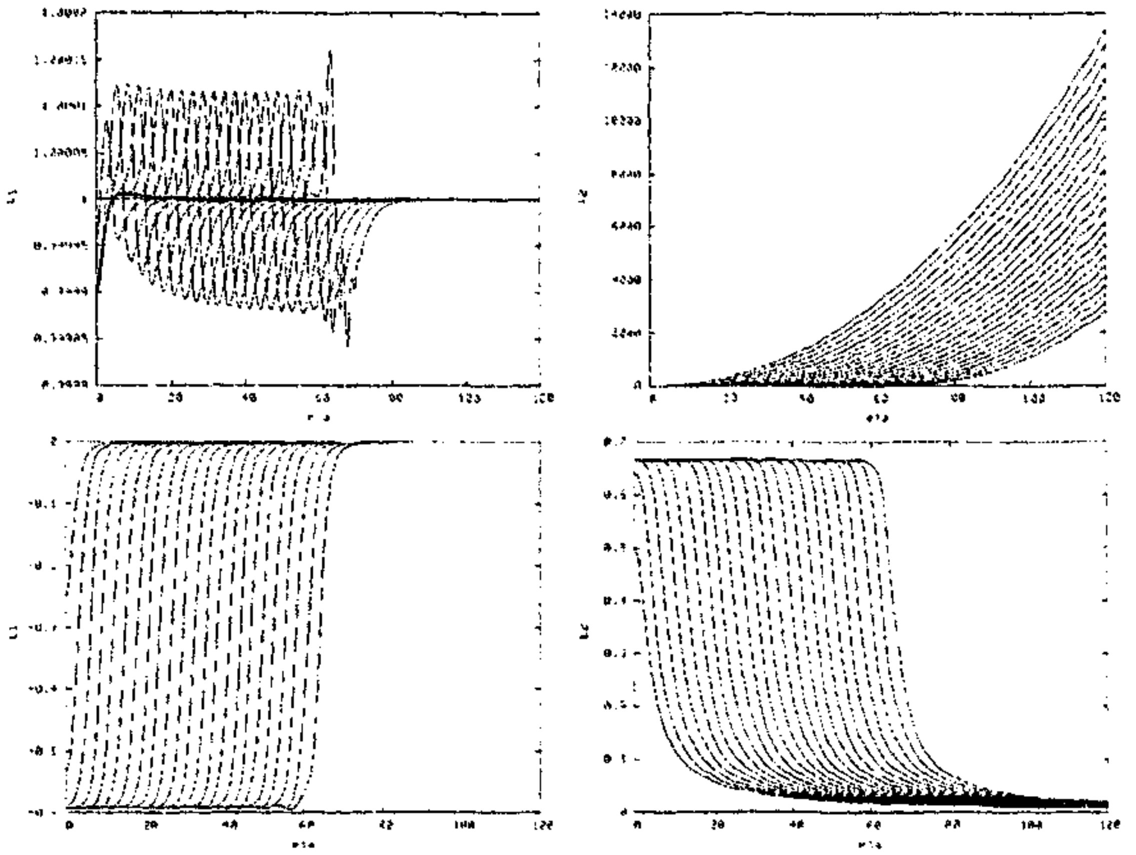

Figure 7.2: *GEM evolution variables for the radial distance locking gauge : metric on line 1, gravito-electric tensor on line 2. All variables are output as a function of $\bar{\eta}$ every $t = 5M$ from $t = 0M$ to $t = 110M$. The resolution is "standard" ($\rho = 2$). We can clearly see the onset of instability, particularly in the evolution of $\perp_1$.*

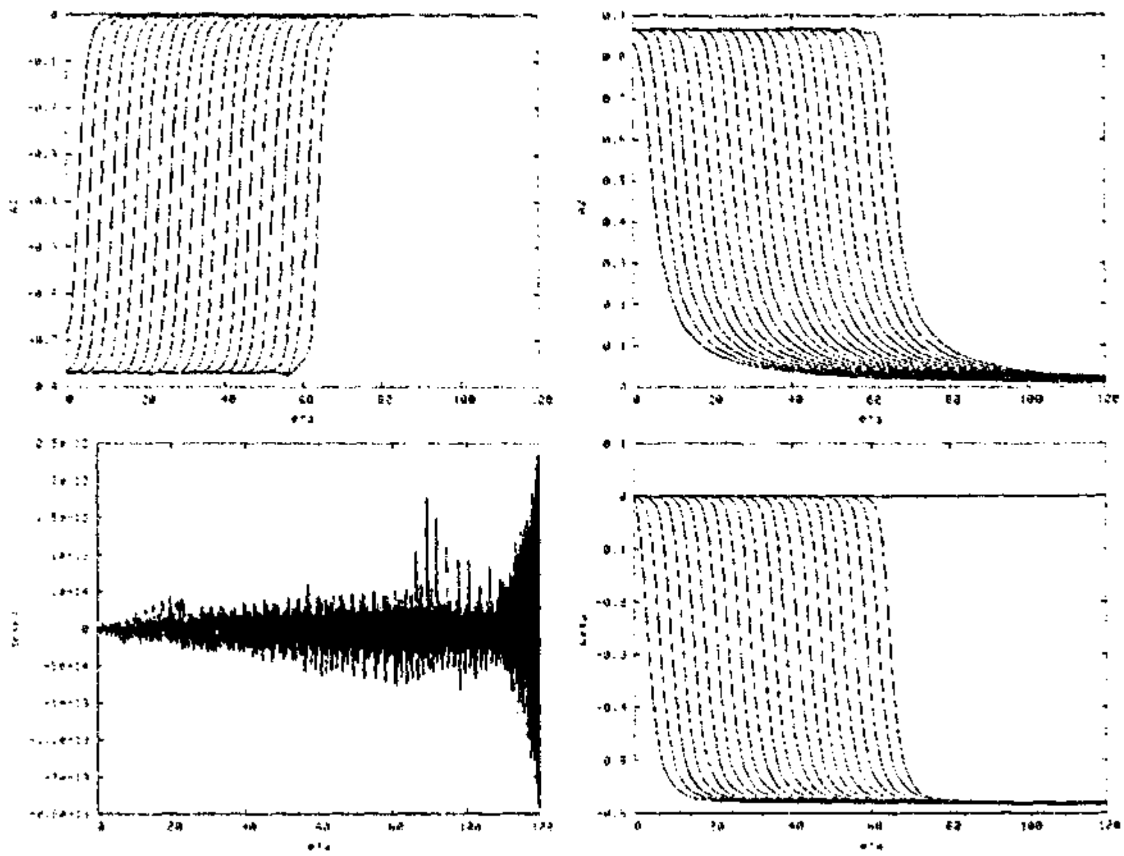

Figure 7.3: *GEM evolution variables for the radial distance locking gauge: trace-free part of the extrinsic curvature on line 1and the trace of the extrinsic curvature on bottom line. All variables are output as a function of $\bar{\eta}$ every $t = 5M$ from $t = 0M$ to $t = 60M$. The resolution is "standard" ($\rho = 2$).*

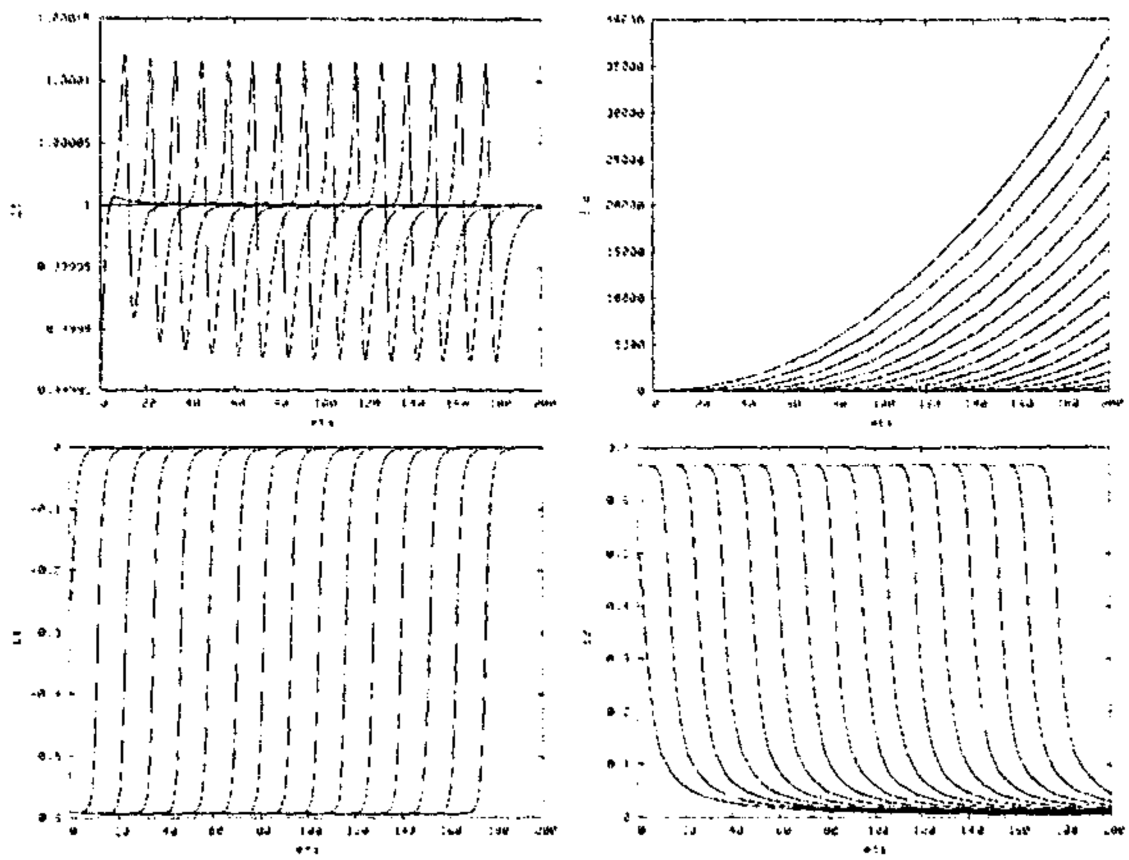

Figure 7.4: *ADM evolution variables : metric on line 1, gravito-electric tensor on line 2. All variables are output as a function of $\bar{\eta}$ every $t = 20M$ from $t = 0M$ to $t = 300M$. The resolution is "standard" ($\rho = 2$).*

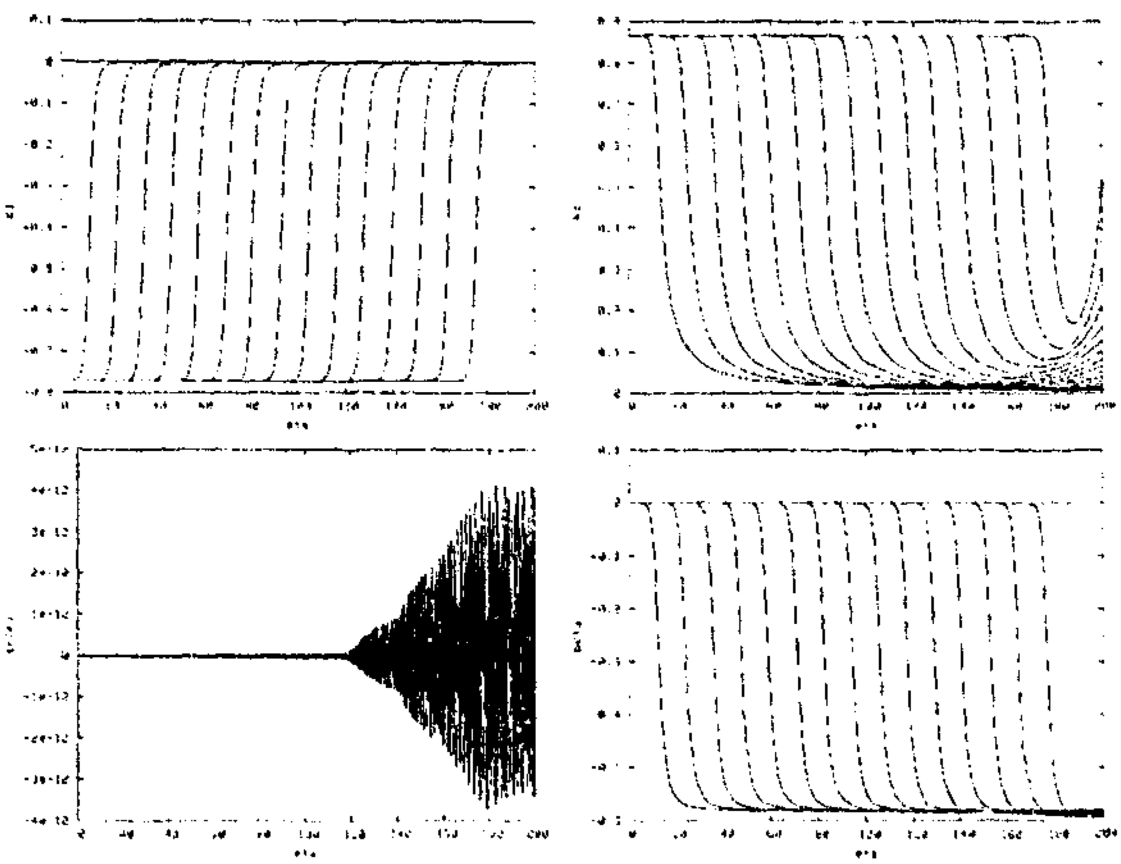

Figure 7.5: *ADM evolution variables : trace-free part of the extrinsic curvature on line 1and the trace of the extrinsic curvature on bottom line. All variables are output as a function of $\bar{\eta}$ every $t = 20M$ from $t = 0M$ to $t = 300M$. The resolution is "standard" ($\rho = 2$).*

although there is, naturally, a slightly higher error on the outer, free boundary.

Although GEM and ADM produce qualitatively similar results in the short term, the GEM evolution is plagued by the onset of an instability which becomes noticeable by 100M (for the Standard resolution) and crashes the code before 150M. The onset of instability is sooner at higher resolutions. It has the form of a high frequency wave (see the evolution of $\perp_1$ in figure 7.2 for an illustration of this).

As a further test, we also ran the above tests whilst enforcing the constraint $\partial_t \perp_1 = 0$, and using centred differences in place of the upwind differences. Neither change had any noticeable effect on the results. The instability appears to be linked to the GEM equations themselves, rather then a numerical error (the same resolution, outer boundary condition, time-stepping etc. routines were used for both sets of equations).

This is also indicated in figure 7.6, where we plot the growth of the Hamiltonian and momentum constraints with time for each of the resolutions tested. We see that the GEM scheme is convergent at early times, but errors dominate as the evolutions continue. Most interesting is the fact that runaway errors appear earlier in the finer resolutions. This implies some sort of gauge-driven instability.

The story is quite different with the ADM equations, however. As figures 7.4 and 7.5 show, the integration proceeded until the code was terminated at t=300M. At this point, almost the entire grid is in the frozen region and we see errors forming on the outer boundary, as our rudimentary boundary conditions are insufficient to allow the information to leave the grid cleanly (see K_2 in fig. 7.5 in particular).

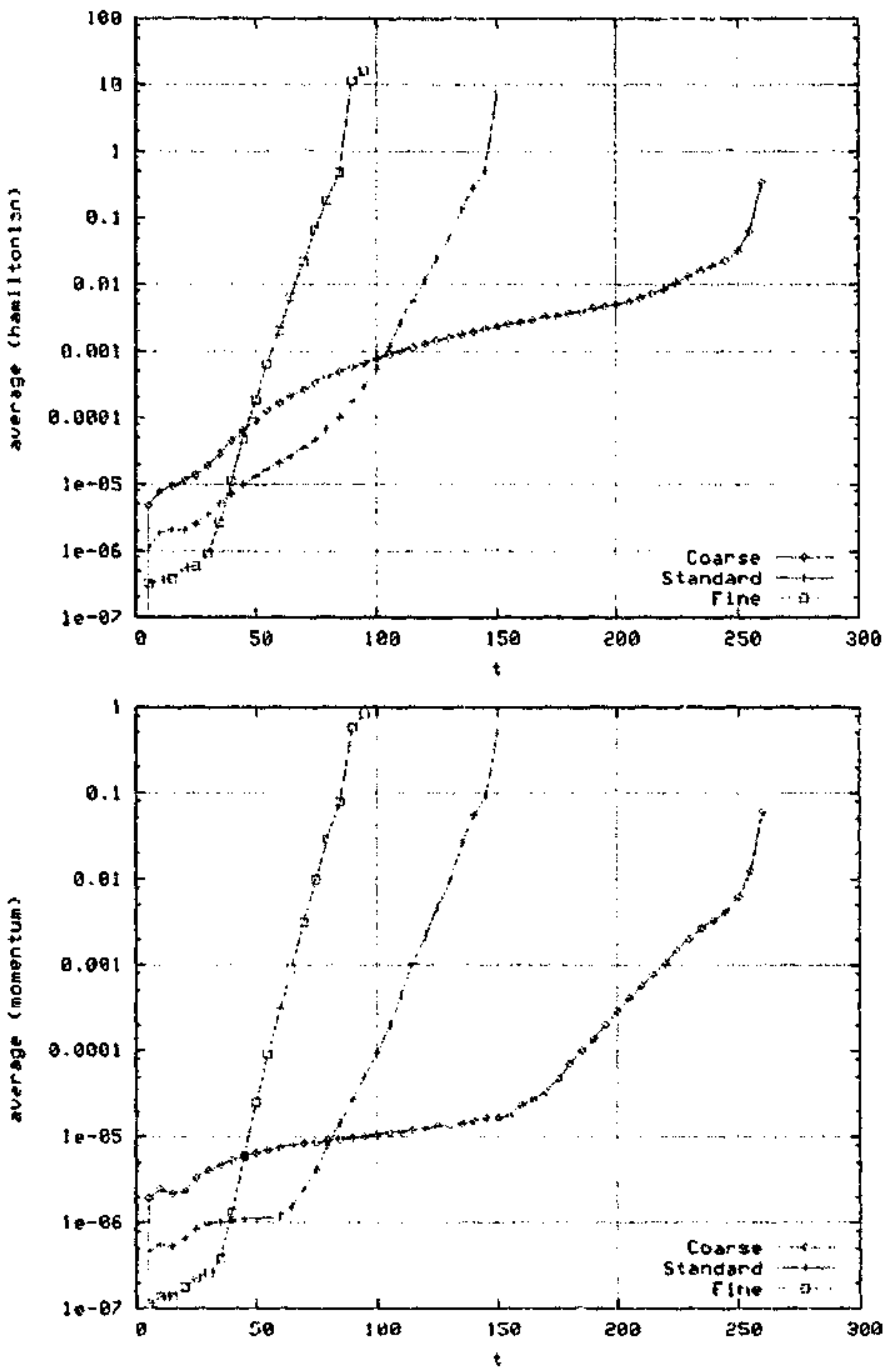

Figure 7.6: *The Hamiltonian (top) and momentum (bottom) constraints as a function of coordinate time. This shows the effect of resolution on the stability of the GEM equations in this slicing.*

To really test out the stability of the ADM equations in this gauge, we rerun the $\rho = 2$ resolution, but extend the spatial domain so that $\bar{\eta}_{out} = 1000$ and time the evolution to run until $t = 1000M$. This allowed the evolution variable to evolve further without interference from the outer boundary. The metric and extrinsic curvature are presented in figure 7.7. The evolution of the Hamiltonian and momentum constraints are given in figure 7.8.

We can see, that although there is still some error on the outer boundary, due to our simple boundary conditions, the evolution proceeds in a stable fashion up to t=1000M. We see that the relative error in the radial metric component, $\perp_1$ remains bounded at around 0.1% and both the Hamiltonian and momentum constraints are also bounded at less then $\sim 3 \times 10^{-5}$ and $\sim 9 \times 10^{-6}$ respectively.

These results are interesting on a number of levels. Firstly, despite the ill-posedness (in a general gauge) of the standard ADM equations, stable and accurate long-term integrations can still be obtained through a prudent choice of slicing condition. Secondly, it is a reminder of how two reasonably similar formulations of the numerical Einstein equations can produce markedly different responses to the same gauge.

Exactly why the GEM case exhibits unstable behaviour with the coordinate and gauge conditions presented here remains an open question. The coordinate and gauge choices both seem to be well-behaved. That is, there is no indication of the kind of gauge shocks we see forming in the maximal and 1+ln slicings with zero shift vector. As we have seen no evidence for gauge modes in GEM from the previous test cases, it remains unclear whether the behaviour presented in this chapter is an anomaly, or

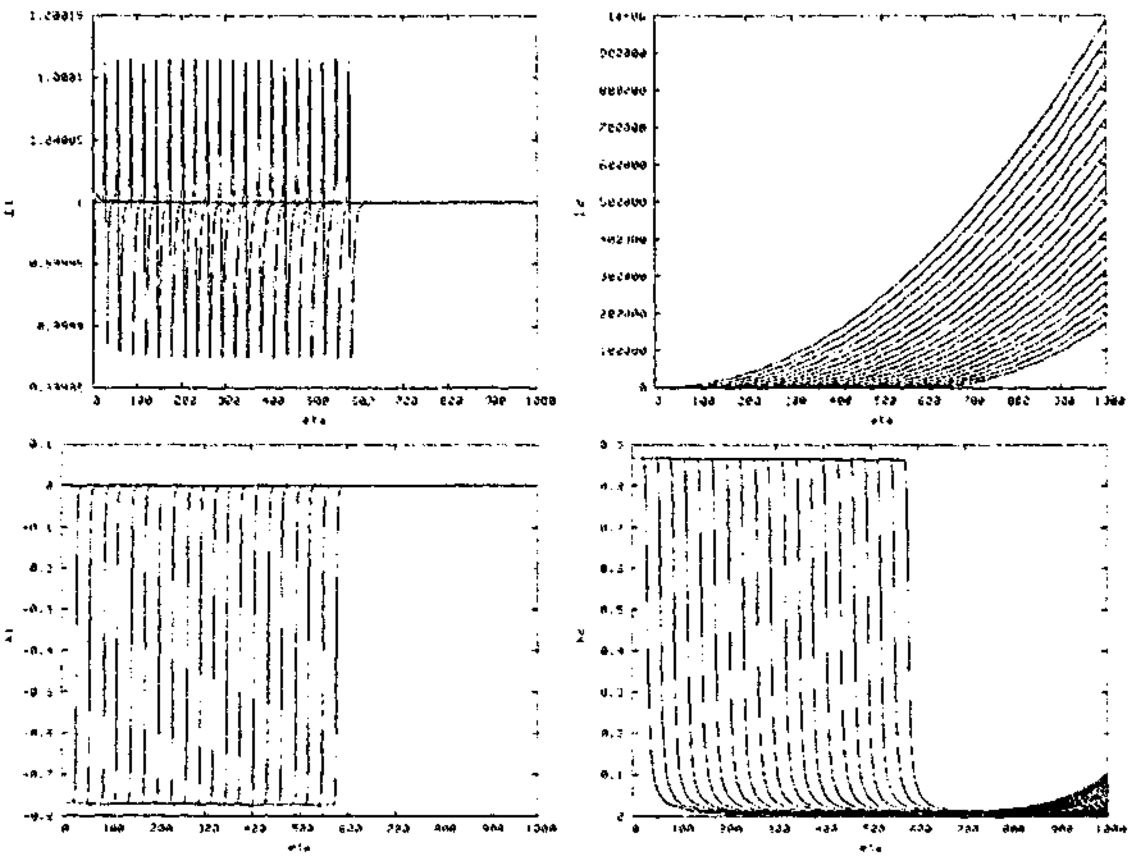

Figure 7.7: *ADM evolution variables output every 50M from t=0M to t=1000M. Metric functions on top line, extrinsic curvature on second and constraints on the bottom line.*

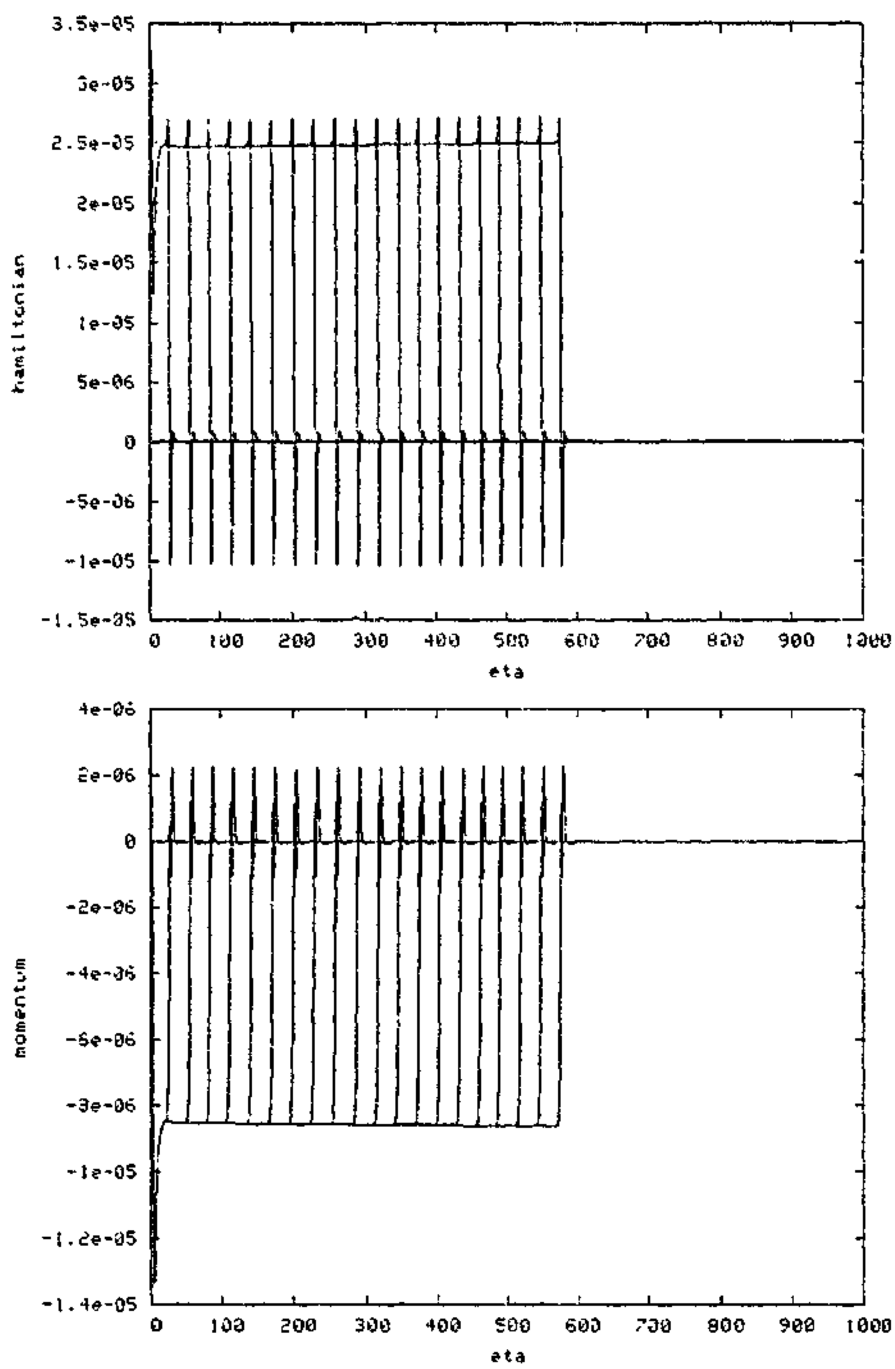

Figure 7.8: *Hamiltonian (top) and momentum constraints for the ADM evolution variables output every 50M from t=0M to t=1000M.*

indicates a deeper pathology of the GEM equations themselves.

The only difference in the structure of the GEM equations in this chapter is the introduction of the shift vector. It is possible that this changes the GEM system in such a way as to introduce spurious gauge modes, and render the system unstable. To answer these questions with any confidence at all would require the GEM system to be tested in a wider range of spacetimes, including higher dimensional spacetimes, with both zero and non-zero shift vectors.

Chapter 8

Conclusions and Future Directions

Responding to the question of stability in numerical general relativity is anything but trivial. To begin to have an understanding of the stability of even one formulation of the 3+1 equations involves investigations of numerical techniques, Courant conditions, gauge dynamics and the mathematical structure of the partial differential equations themselves. Each one of these areas is nontrivial on its own and the interrelation of them creates an area of research deep enough that each individual work can only scratch the surface of the bigger questions.

It is with this in mind that we have limited ourselves to asking some relatively simple questions in this thesis. We have developed a modified set of equations in the 3+1 formalism (the GEM equations) and have compared the behaviour of our equations to the standard ADM equations through a number of standard test-bed calculations. The modification, which centred around augmenting the standard ADM equations with the Bianchi identities (expressed in terms of the Weyl tensor), was presented and discussed in chapter 3.

In works such as this there are a number of ways in which to construct the equations. We must consider which are the fundamental variables? Which are determined through constraints and which through evolution? How, if at all, are the constraints incorporated into the construction of the evolution equations? For clarity, we have considered only one of the possible sets of equations that are obtainable through adding the Bianchi identities to the evolution scheme. A natural extension of the work would involve investigating different forms of the ADM+Bianchi identity combination. Some of the points of difference between the augmented equations used herein and the Standard ADM equations are summarised below:

- The addition of an evolution equation for the gravito-electric tensor, $E_{\mu\nu}$.
- The splitting up of the evolution equation for the extrinsic curvature, $K_{\mu\nu}$ into evolution equations for the trace ($tr(K)$) and trace-free ($A_{\mu\nu}$) parts.
- The use of the gravito-electric tensor to remove the (trace-free) Ricci tensor from the evolution equation for $A_{\mu\nu}$ and the use of the Hamiltonian constraint to replace the Ricci scalar from the evolution equation for $tr(K)$. The resultant set of partial differential equations are now first order in both space and time. this last point was found to be beneficial in the Schwarzschild 1+ln slicing test (section 6.5).

We have also limited ourselves to two one-dimensional spacetimes, namely Minkowski and Schwarzschild. By limiting the range of spacetimes investigated we are able to consider a choice of gauges in each. We have chosen numerical techniques, e.g. time-stepping algorithms and boundary conditions, that were expected to neither detract from or add to the performance of the equations themselves.

Through this work we have been able to glean some insight into the behaviour of the GEM equations in a numerical setting and the broader question of stability. Our findings include:

- For gauge choices that result in a lapse function that does not change with time (geodesic slicing and the implementation of harmonic slicing in the Minkowski+Noise spacetime) the GEM equations reduce to ordinary differential equations, which affects their stability and convergence properties. From the Minkowski + Noise test (section 5.2) we found that the reduction to ordinary differential equations will cause the violation of the constraints to increase with time. This will eventually lead to a runaway error. However, the error growth is kept less than exponential for a thousand light crossing times by a sensible choice of time step.

  In fact, the GEM code proved capable of producing stable results for both the Minkowski+Noise and Minkowski+Gaugewave (section 5.3) simulations. The growth of errors (constraint violation and deviation from exact solution) was at most quadratic for early to medium times (at least into the hundreds of crossing times, except when very large time-steps were used).

- In the Minkowski+Noise test the GEM equations showed no evidence of the periodic error that the ADM equations exhibited for certain resolutions. These errors appear in the ADM case as a result of the existence of gauge modes that result in spurious high frequency waves that are acknowledged as one of the major drawbacks of the standard equations. Importantly, the appearance of these gauge modes seem to be dependant on the ratio dt/dx, implying a Courant type instability.

- The Minkowski+Gaugewave spacetime showed the GEM equations to follow the gauge dynamics as well as the Standard ADM equations (for at least 1000 crossing times). The numerical solution showed no evidence of dissipation and, although the travelling sin wave exhibited an increasing phase error over time, the numerical solution converged to the exact solution with increasing spatial resolution.

The exploration of the Schwarzschild spacetime also showed up some interesting differences in the way the gauge dynamics were handled by GEM and Standard ADM. In particular :

- In both maximal (section 6.4) and 1+ln slicing (section 6.5) the GEM equations produced shorter-lived evolutions than the ADM equations. However, the runaway errors and the loss of convergence appeared to arise from the gauge dynamics rather than an unstable formalism. In particular, both the GEM and Standard ADM codes eventually failed once steep shocks in the evolution variables formed.

  It is interesting that in the 1+ln case, where the ADM equations evolved the spacetime for much longer than the GEM equations, the ADM code was not convergent after about t=30M. This is well before the GEM code became non-convergent due to coordinate shocks. This implies that the ADM evolution's longer life came at the expense of accuracy. It also highlights the importance of convergence testing in a field such as numerical relativity, where we have so few exact solutions for comparison.

The most likely reason this behaviour did not manifest in the GEM code is the absence of second-order spatial derivatives in the GEM formulation. This suggests that the removal of the 3-Ricci tensor terms from the GEM evolution equations results in better convergence.

A number of interesting questions were raised by the modelling of the Schwarzschild spacetime in a maximal+shift vector slicing (chapter 7), where we chose a radial distance locking coordinate and gauge, to avoid the coordinate shocks usually associated with a maximally sliced Schwarzschild simulation .

- The first result is not with respect to the GEM equations at all, but is the fact that in this coordinate system, the ADM equations are able to produce an accurate, stable and convergent long-term integration, despite their known disadvantages. It is an indication of the important role the choice of gauge plays in constructing stable codes.

- This last spacetime, when modelled with the GEM equations gave rise to some difficult questions, that remain open. The simulation was unstable in the long term, with the appearance of a high frequency wave destroying both the accuracy and stability of the evolution. The errors were worse at higher spatial resolutions. This suggests that this is an unphysical, constraint satisfying mode, of the type that can plague the Standard ADM equations. However, this is the only one of the tests conducted here that indicated such a thing, implying that further investigation of these equations is needed.

This was the only one of the spacetimes studied that involved a non-zero shift vector. This could possibly imply that the inclusion of the shift-vector changes the system of GEM equations into a less numerically stable form. On the evidence presented, however, it is impossible to do more than conjecture about this. More tests are necessary to pinpoint whether the radial distance locking coordinate represents an anomalous result, or an underlying property of the GEM equations.

Indeed, as noted above, a work such as this can only scratch the surface of the nature of the GEM equations and their possible use in obtaining stable, accurate long-term evolutions in general relativity. Thus, there exists much scope for extensions to the work presented here. A natural first extension is to test these equations in a 3-dimensional setting. As we have restricted the form of the metric, for clarity, we can only make limited, first conclusions as to the stability of the full GEM equations.

Another extension that would be possible in higher dimensions is to manipulate the structure of the equations themselves. In particular, it would be interesting to analyse the effect of adding the gravito-magnetic tensor into the system, how this changes the structure of the equations and whether it adds or detracts from the overall stability of the system (and why it does so).

One related extension of this work is not in the field of numerical stability, but rather in the the description of radiative spacetimes. Knowing the gravito-electric and gravito-magnetic tensors gives us information about the radiative part of the spacetime. The 3+1 Bianchi identities have a possible application in modelling the production and propagation of gravitational radiation, whether they are coupled to the ADM equations, as in this work, or used in tandem with one of the other variations of the standard equations.

The results presented in this work provide a first step in the analysis of a modification of the numerical Einstein equations. This thesis and its extensions are a part of the process of understanding, not only the behaviour of the equations presented here, but the overall question of 'What makes a stable numerical integration in general relativity and why?' Whether or not these equations prove themselves to be useful in obtaining long-term integrations in more physically interesting settings remain to be seen, but we have provided a case for further investigation into the idea of applying the equations governing gravitoelectromagnetism to numerical relativity.

Bibliography

M. Alcubierre. The appearance of coordinate shocks in hyperbolic formalisms of general relativity. *Physical Review D*, 55(10):5981–5991, May 1997.

M. Alcubierre, G. Allen, C. Bona, D. Fiske, T. Goodale, F. S. Guzmán, I. Hawke, S.H. Hawley, S. Husa, M. Koppitz, C. Lechner, D. Pollney, D. Rideout, M. Salgado, E. Schnetter, E. Seidel, H. Shinkai, D. Shoemaker, B. Szilágyi, R. Takahashi, and J. Winicour. Towards standard testbeds for numerical relativity. (preprint) gr-qc/0305023v1, May 2003a.

M. Alcubierre, G. Allen, B. Brügmann, E. Seidel, and Wai-Mo Suen. Towards and understanding of the stability properties of the 3+1 evolution equations in general relativity. *Physical Review D*, 62(12), Dec 2000.

M. Alcubierre and B. Brügmann. Simple excision of a black hole in 3+1 numerical relativity. *Physical Review D*, 63:104006, May 2001.

M Alcubierre, B. Brügmann, P. Diener, M. Koppitz, D. Pollney, E. Seidel, and R. Takahashi. Gauge conditions for long-term numerical black hole evolutions without excision. *Physical Review D*, 67:084023, 2003b. gr-qc/0206072.

R. Arnowitt, S. Deser, and C. W. Misner. The dynamics of general relativity. In L. Witten, editor, *Gravitation*. John Wiley & Sons, Inc., 1962.

J. Balakrishna, G. Daues, E. Seidel, S. Wai-So, M. Tobias, and E. Wang. Coordinate conditions in three-dimensional numerical relativity. *Classical and Quantum Gravity*, 13:L135–L142, 1996.

A. O. Barut. *Electrodynamics and Classical Theory of Fields and Particles*. Dover Publications, Inc, 1980.

T. Baumgarte and S. Shapiro. On the numerical integration of Einstein's field equations. *Physical Review D*, 59:024007, 1999. gr-qc/9810065.

R. Beig. The maximal slicing of a Schwarzschild black hole. *Annalen der Physik*, 11 (5):507–510, 2000. gr-qc/0005078.

D. H. Bernstein. *A Numerical Study of the Black Hole Plus Brill Wave Spacetime*. PhD thesis, University of Illinois at Urbana-Champaign, 1993.

C. Bona, T. Ledvinka, C. Palenzuela, and M. Žáček. A symmetry-breaking mechanism for the Z4 general-covariant evolution system. (preprint) gr-qc/0307067 v2, Jul 2003.

C. Bona, J. Masso, E. Seidel, and J. Stela. A new formalism of numerical relativity. *Physical Review Letters*, 75(4):600–603, July 1995.

C. Bona, J. Massó, E. Seidel, and P. Walker. Three dimensional numerical relativity with a hyperbolic formulation. (preprint) gr-qc/9804052, submitted to Phys. Rev. D, Apr 1998.

C. Bona and C. Palenzuela. Flux limiter methods in 3D numerical relativity. In L. Fernández and L. M. González, editors, *Current Trends in Relativistic Astrophysics*, volume 617 of *Lecture Notes in Physics*. Springer, 2002. gr-qc/0202101.

L. Brewin. A 3+1 ADM formulation for smooth lattice general relativity. *Classical and Quantum Gravity*, 15:2427–2449, 1998a.

L. Brewin. Riemann normal coordinates, smooth lattices and numerical relativity. *Classical and Quantum Gravity*, 15:3085–3120, 1998b.

L. Brewin. Long term stable integration of a maximally sliced Schwarzschild black hole using a smooth lattice method. *Classical & Quantum Gravity*, 19:429–456, 2002.

B. Brügmann. Numerical relativity in 3+1 dimensions. *Annalen Phys.*, 9:227–246, 2000. gr-qc/9912009.

G. Calabrese, J. Pullin, O Sarbach, and M. Tiglio. Convergence and stability in numerical relativity. *Physical Review D*, 66(4):041501, Aug 2002a. gr-qc/0207018.

G. Calabrese, J. Pullin, O Sarbach, and M. Tiglio. Stability properties of a formulation of Einstein's equations. *Physical Review D*, 66(6):064011, September 2002b. gr-qc/0205073.

G. B. Cook. Initial data for numerical relativity. *Living Reviews in Relativity [Online Article]*, 3, 2000. http://www.livingreviews.org/Articles/Volume3/2000-5cook/ (cited on 25th May 2003).

R. Courant, K Friedrichs, and H. Lewy. On the partial differential equations of mathematical physics. *IBM Journal of Research & Development*, 11:215, 1967. Originally published in *Mathematische Annalen*,100:32-74(1928).

G. F. R. Ellis. Relativistic cosmology. In R. Sachs, editor, *General Relativity and Cosmology*, volume XLVII. Academic Press, 1971.

G. F. R. Ellis. Relativistic cosmology. In E. Schatzman, editor, *Cargése Lectures In Physics*, volume 6. Gordon and Breach Science Publishers, 1973.

H. Friedrich. Hyperbolic reductions for Einstein's equations. *Classical & Quantum Gravity*, 13:1451–1469, 1996.

S. W. Hawking and G. F. R. Ellis. *The Large Scale Structure of Space-Time*. Cambridge Monographs on Mathematical Physics. Cambridge University Press, 1973.

N. Jansen, B. Brügmann, and W. Tichy. Numerical stability of the AA evolution system compared to the ADM and BSSN systems. (preprint) gr-qc/0310100 v1, Oct 2003.

B. Kelly, P. Laguna, K. Lockitch, J. Pullin, E. Schnetter, D. Shoemaker, and M. Tiglio. A cure for unstable numerical evolutions of single black holes: adjusting the standard ADM equations. *Physical Review D*, 64:084013, Oct 2001. gr-qc/0103099.

A. Knapp, E. Walker, and T. Baumgarte. Illustrating stability properties of numerical relativity in electrodynamics. *Physical Review D*, 65:064031, 2002. gr-qc/0201051.

R. Maartens. Linearisation instability of gravity waves? *Phys. Rev. D*, 55:463, 1997.

R. Maartens and B. A. Bassett. Gravito-electromagnetism. *Classical Quantum Gravity*, 15:705, 1998. gr-qc/9704059 v3.

C. W. Misner, K. S. Thorne, and J. A. Wheeler. *Gravitation*. W.H Freeman and Company, 1973.

W.H. Press, S.A. Teukolsky, W.T. Vetterling, and B.P. Flannery. *Numerical Recipes in FORTRAN 77, The Art of Scientific Computing*, volume 1. Cambridge University Press, 2nd edition, 1996.

O. Reula. Hyperbolic methods for Einstein's equations. *Living Reviews in Relativity*, 1998. [Online article]: cited on 1st Oct. 2003, http://www.livingreviews.org/lrr-1998-3.

M. Shibata and T. Nakamura. Evolution of three-dimensional gravitational waves: Harmonic slicing case. *Physical Review D*, pages 5428–5444, Nov 1995.

H Shinkai and G. Yoneda. Reformulating the Einstein equations for stable numerical simulations. (preprint) gr-qc/0209111v2, Sept 2002.

S. Teukolsky. Stability of the iterated Crank-Nicholson method in numerical relativity. *Physical Review D*, 61(8), March 2000.

R. M. Wald. *General Relativity*. The University of Chicago, 1984.

J. W. York. Kinematics and dynamics of general relativity. In L. L. Smarr, editor, *Sources of Gravitational Radiation*. Cambridge University Press, 1979.